



UNIVERSITEIT VAN PRETORIA  
UNIVERSITY OF PRETORIA  
YUNIBESITHI YA PRETORIA

# **The effect of environmental loading on restrained reinforced concrete T-Beams**

**Kleynhans, Amé**

**A dissertation submitted in partial fulfilment of the requirements for the degree of**

**MASTER OF ENGINEERING (STRUCTURAL ENGINEERING)**

**In the**

**FACULTY OF ENGINEERING, BUILT ENVIRONMENT AND INFORMATION**

**TECHNOLOGY**

**UNIVERSITY OF PRETORIA**

**2023**

# DISSERTATION SUMMARY

## THE EFFECT OF ENVIRONMENTAL LOADING ON RESTRAINED REINFORCED CONCRETE T-BEAMS

A KLEYNHANS

**Supervisor:** Kearsley, Elsabe P.  
**Co-Supervisor:** Dr S.A Skorpen  
**Department:** Civil Engineering  
**University:** University of Pretoria  
**Degree:** Master of Engineering (Structural Engineering)

Environmental conditions have the potential to cause stresses within reinforced concrete structures which equal or exceed the stresses caused by typical design dead or live loading. Concrete bridges are particularly susceptible to these effects as result of exposure to harsh environments throughout construction and service periods. The stresses caused by environmental loading are influenced by the material composition as well as the geometric properties of the structural element. Consequently, the selected type of cross-section used in bridge construction will influence the bridge's response to environmental conditions.

The main objective of this study was to compare the response of two scale model T-beams with different cross-sections to environmental loading, with specific focus on temperature and shrinkage effects independently and in combination. The T-beams were designed to be solid and voided to emulate the configurations of solid spine beam and box girder bridge cross sections, respectively. The scale size of the T-beams had two major advantages. One advantage was the practicality of constructing moulds and casting smaller sections compared to full scale sections. The second advantage was the ability to analyse the response of beams, commonly employed in construction and of similar size, to environmental loading. This expands the scope of considerations beyond bridge design applications.

The stress profiles through the T-beams were of particular interest since they provided clear insights into the conditions which caused tensile stresses which exceeded the tensile capacity of the concrete and should therefore be considered within design. In order to calculate the stress profiles in both vertical and transverse directions, the temperatures and strains throughout the T-beams had to be recorded. Thermocouples and Vibrating Wire Strain Gauges were embedded into the concrete and measurements of temperature and strain were logged at 15min intervals, from the time of casting for the duration of the study. To allow accurate strain measurement, the T-beams were designed and cast in a manner which allowed unrestricted free movement as far as possible. This was achieved by minimising the constraints imposed by the supports.

Typical daily thermal stresses were considered and factors such as heat of hydration and drying shrinkage over time were analysed to identify conditions which caused tensile stresses greater than the tensile strength of the concrete. This study showed that cross-section type and restraint conditions had significant effects on T beam behaviour in response to environmental conditions. The solid T-beam developed smaller longitudinal stresses caused by shrinkage and temperature but highlighted the need to consider the stress differentials in the transverse direction as well as the web to flange thickness ratio. The voided T-beam was more prone to curvature caused by temperature, shrinkage and swell, but developed more uniform stresses in the transverse direction of the section. Furthermore, the largest stress component was caused by the restraint of average longitudinal elongation and contraction of both T-beams, which emphasized the need to consider the timing at which restraint is applied to concrete elements.

## DECLARATION

I, the undersigned hereby declare that:

- I understand what plagiarism is and I am aware of the University's policy in this regard;
- The work contained in this thesis is my own original work;
- I did not refer to work of current or previous students, lecture notes, handbooks or any other study material without proper referencing;
- Where other people's work has been used this has been properly acknowledged and referenced;
- I have not allowed anyone to copy any part of my dissertation;
- I have not previously in its entirety or in part submitted this dissertation at any university for a degree.



---

**Amé Kleynhans**

**18142452**

**November 2023**

## ACKNOWLEDGEMENTS

In keeping with the proverbial wisdom ‘it takes a village’, I wish to express my sincere gratitude to the people whose contributions made this dissertation possible:

- a) My supervisor Professor Elsabe Kearsley, for her patience, guidance and continued encouragement to produce the best outcomes possible.
- b) Dr Sarah Skorpen, my co-supervisor, for her insight and guidance.
- c) My senior postgraduate students Ms Megan Brink and Mr Hendrik Louw for their unmatched efforts, continued support and late-night aid. Without your assistance the wheels would surely have come off more than once. Thank you to Mr Richart Ross and Mr Kyle Hambidge for your assistance with casting and mould construction.
- d) I would like to thank the laboratory staff at the University of Pretoria:
  - i. Mr Johan Scholtz who assisted throughout the panning, instrumentation and casting phases, often providing ‘bigger picture’ perspective and common sense when mine failed.
  - ii. Mr Jordan Mostert for his technical assistance
  - iii. The concrete laboratory staff: Mr Richard Ncabeleng, Mr Chris Baloyi, Mr Kgwara Mokomane, Mr Jan Ngwenya, Mr Jonas Selwadi and Mr Frank Vein for their assistance with preparations and casting
- e) My family and friends for their ongoing encouragement and reassurance during the study.

AfriSam is appreciatively recognised for providing the Readymix concrete used to cast the T-beams instrumented and analysed in this study.

The South African National Roads Agency (SANRAL) is gratefully acknowledged for supporting this study, which formed part of the broader SANRAL research project on integral bridges, contract number: 1002-58600-2018 P7a2.

Words of gratitude will never be enough to describe the support I received though out this study. The highs (and lows) produced more learning opportunities than I could ever have imagined. I truly hope the work presented here does all the effort committed to this project justice.

# TABLE OF CONTENTS

|       |  |      |
|-------|--|------|
| 1     | INTRODUCTION .....                                   | 1-1  |
| 1.1   | Background.....                                      | 1-1  |
| 1.2   | Objectives of the study .....                        | 1-4  |
| 1.3   | Scope of the study.....                              | 1-5  |
| 1.4   | Methodology.....                                     | 1-5  |
| 1.5   | Organisation of the report.....                      | 1-6  |
| 2     | LITERATURE REVIEW.....                               | 2-1  |
| 2.1   | Introduction .....                                   | 2-1  |
| 2.2   | Cracking of Reinforced Concrete .....                | 2-1  |
| 2.3   | Thermal Stresses.....                                | 2-4  |
| 2.3.1 | Heat of Hydration .....                              | 2-4  |
| 2.3.2 | Temperature Distributions and Restraint.....         | 2-7  |
| 2.3.3 | TMH7:1981 Temperature Guidelines.....                | 2-12 |
| 2.4   | Shrinkage .....                                      | 2-13 |
| 2.4.1 | Differential Shrinkage .....                         | 2-13 |
| 2.4.2 | Environmental Effects .....                          | 2-15 |
| 2.4.3 | TMH7:1989 Shrinkage Guidelines.....                  | 2-16 |
| 2.5   | Previous Field, Experimental and Numerical work..... | 2-18 |
| 2.6   | Summary.....   | 2-23 |
| 3     | EXPERIMENTAL SETUP AND WORK .....                    | 3-1  |
| 3.1   | Introduction .....                                   | 3-1  |
| 3.2   | T-beam Configuration .....                           | 3-1  |
| 3.2.1 | Mould Construction.....                              | 3-3  |
| 3.2.2 | Reinforcement .....                                  | 3-5  |
| 3.3   | Instrumentation.....                                 | 3-6  |
| 3.3.1 | Introduction .....                                   | 3-6  |
| 3.3.2 | Thermocouples .....                                  | 3-7  |
| 3.3.3 | Vibrating Wire Strain Gauges .....                   | 3-11 |

|       |  |      |
|-------|--|------|
| 3.3.4 | Weather Station and Ambient Temperature .....          | 3-14 |
| 3.4   | Concrete Casting.....                                  | 3-15 |
| 3.4.1 | Mix Design .....                                       | 3-15 |
| 3.4.2 | Casting and Curing Conditions.....                     | 3-15 |
| 3.5   | Concrete Material Properties .....                     | 3-17 |
| 3.5.1 | Setting Time .....                                     | 3-17 |
| 3.5.2 | Coefficient of Thermal Expansion.....                  | 3-19 |
| 3.5.3 | Compressive Strength.....                              | 3-20 |
| 3.5.4 | Tensile Strength.....                                  | 3-21 |
| 3.5.5 | Modulus of Elasticity.....                             | 3-22 |
| 3.5.6 | Drying Shrinkage.....                                  | 3-22 |
| 3.6   | Summary of Material and Cross Section Properties ..... | 3-23 |
| 4     | COMPARING SOLID AND VOIDED T-BEAM CROSS SECTIONS.....  | 4-1  |
| 4.1   | Measured Trends .....                                  | 4-1  |
| 4.1.1 | Temperature.....                                       | 4-2  |
| 4.1.2 | Strain.....  | 4-5  |
| 4.1.3 | Shrinkage.....   | 4-7  |
| 4.2   | Typical Daily Temperature Distributions .....          | 4-10 |
| 4.3   | Typical Daily Calculated Strain.....                   | 4-17 |
| 4.3.1 | Vertical Thermal Strain .....                          | 4-18 |
| 4.3.2 | Transverse Thermal Strain.....                         | 4-19 |
| 4.4   | Typical Daily Calculated Stress.....                   | 4-20 |
| 4.4.1 | Self-equilibrating Stress .....                        | 4-20 |
| 4.4.2 | Curvature Stress and Secondary Thermal Moments.....    | 4-22 |
| 4.4.3 | Effective Temperature Stress.....                      | 4-24 |
| 4.4.4 | Total Thermal Stress.....                              | 4-25 |
| 4.5   | Measured Strains .....                                 | 4-27 |
| 4.6   | Summary of Results.....                                | 4-30 |
| 4.6.1 | Measured Temperature .....                             | 4-30 |
| 4.6.2 | Measured Strain.....                                   | 4-30 |

|       |   |      |
|-------|---|------|
| 4.6.3 | Calculated Stress.....  | 4-31 |
| 5     | FACTORS INCREASING TENSILE STRESS .....   | 5-1  |
| 5.1   | Introduction .....  | 5-1  |
| 5.2   | Temperature caused by Heat of Hydration .....   | 5-1  |
| 5.3   | Total Stress caused by Heat of hydration .....  | 5-7  |
| 5.3.1 | Vertical Stress Distribution caused by Heat of Hydration.....   | 5-7  |
| 5.3.2 | Transverse Stress Distribution caused by Heat of Hydration .....  | 5-9  |
| 5.4   | Shrinkage .....   | 5-11 |
| 5.5   | Stresses caused by Effective Temperature and Shrinkage.....   | 5-12 |
| 5.6   | Curvature and Self-equilibrating Stress.....  | 5-15 |
| 5.6.1 | Temperature.....  | 5-16 |
| 5.6.2 | Shrinkage.....  | 5-17 |
| 5.6.3 | Combined Effects of Temperature and Shrinkage.....  | 5-18 |
| 5.7   | Summary of Results.....   | 5-28 |
| 6     | CONCLUSIONS AND RECOMMENDATIONS .....   | 6-1  |
| 6.1   | Conclusions .....   | 6-1  |
| 6.2   | Recommendations for Further Research.....   | 6-5  |
| 6.3   | Recommendations for Design and Construction of Reinforced Concrete Beams exposed to Environmental Loading ..... | 6-6  |
| 7     | REFERENCES.....   | 7-1  |
|       | APPENDIX A .....  | A-I  |



## LIST OF TABLES

|  |      |
|--|------|
| Table 2-1 Induced thermal effects of temperature distributions and restraint ..... | 2-9  |
| Table 2-2 Previous Field Work.....   | 2-20 |
| Table 2-3 Previous Experimental Work .....   | 2-21 |
| Table 2-4 Previous Numerical Work .....  | 2-22 |
| Table 3-1 Concrete Mix Proportions .....   | 3-15 |
| Table 3-2 TMH7:1989 predicted shrinkage values .....                               | 3-23 |
| Table 3-3 Representative Material Properties.....                                  | 3-24 |
| Table 3-4 Cross-section Properties .....   | 3-24 |
| Table 4-1 Effective Temperature Ranges .....                                       | 4-2  |
| Table 4-2 Maximum and Minimum recorded Temperatures.....                           | 4-3  |
| Table 5-1 Effective temperatures related to heat of hydration .....                | 5-2  |

## LIST OF FIGURES

|  |      |
|--|------|
| Figure 2-1 Design parameters affecting early-age concrete cracking.....  | 2-2  |
| Figure 2-2 Causes of bridge deck cracking.....   | 2-3  |
| Figure 2-3 Heat flow in an exposed bridge deck.....  | 2-7  |
| Figure 2-4 Damage at support due to prying forces .....  | 2-10 |
| Figure 2-5 Overloading of outside bearings due to transverse hogging of end diaphragm .....                                      | 2-11 |
| Figure 2-6 (a) Transverse constrained bending stresses and (b) axial stresses.....   | 2-11 |
| Figure 2-7 Temperature distribution guidelines for concrete elements .....   | 2-12 |
| Figure 2-8 Response of concrete to cycles of alternate drying and wetting .....  | 2-15 |
| Figure 2-9 Coefficient for environmental conditions - $k_L$ .....  | 2-16 |
| Figure 2-10 Coefficient for concrete composition - $k_c$ .....   | 2-17 |
| Figure 2-11 Coefficient for effective thickness - $k_e$ .....  | 2-17 |
| Figure 2-12 Variation as a function of time thickness - $k_j$ .....  | 2-17 |
| Figure 3-1 Cross sectional dimensions of T-beams.....  | 3-1  |
| Figure 3-2 Elevation view of cantilever arrangement.....   | 3-2  |
| Figure 3-3 Solid T-beam mould 3D rendering .....   | 3-3  |
| Figure 3-4 Voided T-beam mould 3D rendering.....   | 3-3  |
| Figure 3-5 Mould support layout.....   | 3-3  |
| Figure 3-6 Completed solid T-beam mould.....   | 3-4  |
| Figure 3-7 Solid T-beam mould with reinforcement cage.....   | 3-4  |
| Figure 3-8 Reinforcement layout.....   | 3-5  |
| Figure 3-9 Reinforcement cages .....   | 3-5  |
| Figure 3-10 Reinforcement stress versus strain relationship .....  | 3-6  |
| Figure 3-11 Thermocouple positions.....  | 3-7  |
| Figure 3-12 (a) Section, (b) Vertical nonlinear temperature distribution, (c) strain profile, (d) self-equilibrating stress..... | 3-8  |
| Figure 3-13 Strain profile with effective and continuity stresses .....  | 3-11 |
| Figure 3-14 Components of total thermal stress.....  | 3-11 |

|   |      |
|---|------|
| Figure 3-15 VWSG positions .....  | 3-13 |
| Figure 3-16 Plan view of VWSGs fixed to steel in voided T-beam mould.....   | 3-14 |
| Figure 3-17 Moulds and concrete mixer truck before and during casting.....  | 3-16 |
| Figure 3-18 Concrete surface floating .....   | 3-16 |
| Figure 3-19 Curing blankets placed over beams .....   | 3-16 |
| Figure 3-20 Completed T-beams .....   | 3-17 |
| Figure 3-21 T-beams in cantilever configuration .....   | 3-17 |
| Figure 3-22 VWSG position for setting time determination .....  | 3-18 |
| Figure 3-23 Change in temperature due to heat of hydration .....  | 3-18 |
| Figure 3-24 Derivative of hydration with time.....  | 3-18 |
| Figure 3-25 VWSG in unreinforced 0.5 m cube for CTE.....  | 3-19 |
| Figure 3-26 Strain versus $\Delta T$ for the duration of the study.....   | 3-20 |
| Figure 3-27 Compressive Strength .....  | 3-21 |
| Figure 3-28 Tensile Strength .....  | 3-21 |
| Figure 3-29 Modulus of elasticity.....  | 3-22 |
| Figure 4-1 Rainfall for the months of April to October 2023 .....   | 4-1  |
| Figure 4-2 Effective temperatures over time .....   | 4-2  |
| Figure 4-3 Daily effective temperature range versus area of cross-section per unit deck width .....               | 4-4  |
| Figure 4-4 Comparison of vertical temperature distributions to TMH7:1981 .....                                    | 4-5  |
| Figure 4-5 Total measured strains at selected positions of the (a) solid and (b) voided T-beam .....              | 4-6  |
| Figure 4-6 Shrinkage measurements for the (a) solid and (b) voided T-beam .....                                   | 4-7  |
| Figure 4-7 Effective temperatures for 29/07/2023 to 01/08/2023 .....  | 4-10 |
| Figure 4-8 Temperature distributions ( $T_0$ : 29/07/2023 at 08:30).....  | 4-11 |
| Figure 4-9 Temperature distributions from 00:00 to 09:00 on 31/07/2023 .....                                      | 4-12 |
| Figure 4-10 Temperature distributions from 12:00 to 21:00 on 31/07/2023 .....                                     | 4-13 |
| Figure 4-11 Daily vertical temperature distributions for the (a) solid and (b) voided T-beams on 31/07/2023 ..... | 4-15 |

|  |      |
|--|------|
| Figure 4-12 Temperature planes with (a) vertical and (b) transverse measured temperature distributions for solid T-beam .....                | 4-16 |
| Figure 4-13 Daily transverse temperature distributions of the (a) solid and (b) voided T-beams on 31/07/2023 .....                           | 4-16 |
| Figure 4-14 Hypothetical free (a) vertical and (b) transverse strains and strain planes for solid T-beam .....                               | 4-17 |
| Figure 4-15 Vertical hypothetical free and plane strain for the (a) solid and (b) voided T-beams....   | 4-18 |
| Figure 4-16 Transverse hypothetical free and plane strain for the (a) solid and (b) voided T-beams   | 4-19 |
| Figure 4-17 Vertical self-equilibrating stress for the (a) solid and (b) voided T-beams.....   | 4-21 |
| Figure 4-18 Transverse self-equilibrating stress for the (a) solid and (b) voided T-beams.....   | 4-22 |
| Figure 4-19 Curvature stress and moment for the (a) solid and (b) voided restrained T-beams .....  | 4-23 |
| Figure 4-20 Curvature stress in transverse direction for the (a) solid and (b) voided restrained T-beams .....                               | 4-24 |
| Figure 4-21 Effective temperature stress for the (a) solid and (b) voided restrained T-beams .....   | 4-25 |
| Figure 4-22 Total vertical thermal stress for the (a) solid and (b) voided restrained T-beams.....   | 4-26 |
| Figure 4-23 Total transverse thermal stress for the (a) solid and (b) voided restrained T-beams .....  | 4-26 |
| Figure 4-24 Measured and calculated strains for the (a) solid and (b) voided T-beams.....  | 4-28 |
| Figure 4-25 Measured and calculated strain difference for the (a) solid and (b) voided T-beams ....  | 4-29 |
| Figure 5-1 Temperature distributions from 15:00 04/04/2023 to 00:00 05/04/2023 .....   | 5-3  |
| Figure 5-2 Temperature distributions from 03:00 to 09:00 on 05/04/2023 .....   | 5-4  |
| Figure 5-3 Vertical heat of hydration temperature distributions for the (a) solid and (b) voided T-beams on 04/04/2023 to 05/04/2023 .....   | 5-5  |
| Figure 5-4 Transverse heat of hydration temperature distributions for the (a) solid and (b) voided T-beams on 04/04/2023 to 05/04/2023 ..... | 5-6  |
| Figure 5-5 Vertical total thermal stress for the (a) solid and (b) voided restrained T-beams on 04/04/2023 to 05/04/2023 .....               | 5-8  |
| Figure 5-6 Transverse total thermal stress for the (a) solid and (b) voided restrained T-beams on 04/04/2023 to 05/04/2023 .....             | 5-9  |
| Figure 5-7 Cracking between web and flange section of solid T-beam.....  | 5-10 |
| Figure 5-8 Shrinkage measurements of selected points.....  | 5-11 |

Figure 5-9 Effective stress development over time for the (a) solid and (b) voided restrained T-beams ..... 5-14

Figure 5-10 VWSG positions for curvature comparison ..... 5-15

Figure 5-11 Curvature plane and gauge readings for temperature at 07:00 on 27/04/2023 ..... 5-16

Figure 5-12 Curvature plane and gauge readings for temperature at 13:30 on 28/04/2023 ..... 5-17

Figure 5-13 Curvature plane and gauge readings for shrinkage on 28/04/2023 ..... 5-17

Figure 5-14 Total curvature stresses for the solid T-beam on 28/04/2023 at 13:30 ..... 5-21

Figure 5-15 Total curvature stresses for the voided T-beam on 28/04/2023 at 13:30 ..... 5-22

Figure 5-16 Total curvature stresses for the solid T-beam on 27/04/2023 at 07:00 ..... 5-23

Figure 5-17 Total curvature stresses for the voided T-beam on 27/04/2023 at 07:00 ..... 5-24

Figure 5-18 Total bending moment over time ..... 5-25

Figure 5-19 Self-equilibrating stress at selected positions of the (a) solid and (b) voided T-beam .. 5-26

Figure 5-20 Total curvature stress at selected positions of the (a) solid and (b) voided restrained T-beam ..... 5-27

## LIST OF SYMBOLS

| Symbol        | Description  | Units           |
|---------------|--|-----------------|
| $A$           | cross-sectional area   | mm <sup>2</sup> |
| $A_i$         | area of the $i^{\text{th}}$ segment a section  | mm <sup>2</sup> |
| $CF$          | vibrating wire strain gauge calibration factor                                       |                 |
| $\Delta_{cs}$ | shrinkage deformation from TMH7:1989   | $\mu\epsilon$   |
| $E$           | modulus of elasticity of concrete  | GPa             |
| $E_s$         | modulus of elasticity of steel   | GPa             |
| $f_c$         | concrete compressive strength  | MPa             |
| $f_{ct}$      | concrete tensile strength  | MPa             |
| $h$           | height above the soffit  | mm              |
| $h_e$         | effective thickness  | mm              |
| $I$           | second moment of area about the axis through the centroid                            | mm <sup>4</sup> |
| $k_L$         | partial coefficient for shrinkage deformations dependent on environmental conditions |                 |
| $k_c$         | partial coefficient for shrinkage deformations dependent on concrete composition     |                 |
| $k_e$         | partial coefficient for shrinkage deformations dependent effective thickness         |                 |
| $k_j$         | partial coefficient for shrinkage deformations dependent on time                     |                 |
| $l_0$         | original element length  | mm              |
| $\Delta l$    | change in length   | mm              |
| $\Delta M$    | bending moment   | kNm             |
| $NA$          | neutral axis   | mm              |
| $\Delta N$    | axial force  | kN              |
| $R_n$         | initial frequency reading  | Hz              |
| $R_{n+1}$     | subsequent frequency reading   | Hz              |

|                            |   |                              |
|----------------------------|---|------------------------------|
| $T_0$                      | temperature datum   | °C                           |
| $T_i$                      | temperature of the $i^{\text{th}}$ segment a section      | °C                           |
| $T_n$                      | initial temperature reading                               | °C                           |
| $T_{n+1}$                  | subsequent temperature reading                            | °C                           |
| $T_{eff}$                  | effective temperature                                     | °C                           |
| $T_{eff0}$                 | effective temperature at selected datum                   | °C                           |
| $T_{effavg}$               | average effective temperature                             | °C                           |
| $T_{effset}$               | effective temperature at final concrete setting time      | °C                           |
| $\Delta T$                 | change in temperature                                     | °C                           |
| $\Delta T_{eff}$           | change in effective temperature                           | °C                           |
| $\Delta T_{effavg}$        | change in average effective temperature                   | °C                           |
| $\Delta T_{(y)}$           | change in temperature at position y from the neutral axis | °C                           |
| y                          | distance from neutral axis                                | mm                           |
| $\alpha_c$                 | coefficient of thermal expansion of concrete              | $\mu\epsilon/^\circ\text{C}$ |
| $\alpha_{gauge}$           | coefficient of thermal expansion of VWSG                  | $\mu\epsilon/^\circ\text{C}$ |
| $\delta\text{Stress}$      | difference from total effective stress                    | MPa                          |
| $\delta\text{Shrinkage}$   | difference from effective shrinkage                       | $\mu\epsilon$                |
| $\delta\text{Temperature}$ | difference from effective temperature                     | °C                           |
| $\epsilon_0$               | axial strain at the centroid                              | $\mu\epsilon$                |
| $\epsilon_{ct}$            | concrete tensile strain                                   | $\mu\epsilon$                |
| $\epsilon_{dry}$           | drying shrinkage strain after 6months                     | $\mu\epsilon$                |
| $\epsilon_{free}$          | hypothetical free strain                                  | $\mu\epsilon$                |
| $\epsilon_m$               | mechanical strain   | $\mu\epsilon$                |
| $\epsilon_{plane}$         | plane strain  | $\mu\epsilon$                |
| $\epsilon_{seff}$          | effective shrinkage strain                                | $\mu\epsilon$                |

|                         |   |                  |
|-------------------------|---|------------------|
| $\varepsilon_{Seffset}$ | effective shrinkage strain from final concrete setting time | $\mu\varepsilon$ |
| $\varepsilon_t$         | thermal strain  | $\mu\varepsilon$ |
| $\varepsilon_{total}$   | total temperature compensated VWSG strain                   | $\mu\varepsilon$ |
| $\psi$                  | curvature   | $\text{mm}^{-1}$ |
| $\sigma_{Curv}$         | curvature stress  | MPa              |
| $\sigma_{restraint}$    | theoretical stress from artificial restraint                | MPa              |
| $\sigma_{Seff}$         | effective shrinkage stress                                  | MPa              |
| $\sigma_{Self-eq}$      | self-equilibrating stress                                   | MPa              |
| $\sigma_{Teff}$         | effective temperature stress                                | MPa              |
| $\sigma_{Total}$        | total thermal stress  | MPa              |
| $\sigma_{Totaleff}$     | total effective stress                                      | MPa              |



# 1 INTRODUCTION

## 1.1 BACKGROUND

Reinforced concrete bridges are among the most common types of bridges constructed globally. The appeal of reinforced concrete lies in its versatility and durability and reinforced concrete bridges are well suited for spanning various distances and supporting various intended design loads. Two prevalent cross-sectional types often used in concrete bridge design are the solid spine beam and slab, and the box girder configurations. Typically, where longer spans are implemented, deeper sections are required and box girders are preferred due to their reduced self-weight when compared to solid sections. In structural design, the expected loads govern design considerations. For bridge design, self-weight and live critical traffic loading will typically govern the design. However, designers also need to be cognisant of the environment conditions in which the bridge structure is constructed and remains for its expected service life. Due to concrete's material properties, it constantly responds to its environmental conditions, causing stresses within the structure, similar to that caused by dead and live loads. As such environmental conditions which cause stresses within structures will be referred to as environmental loading. Environmental loading is particularly important in the design of bridge structures, which are exposed to harsh environments throughout their lifespans.

Two mechanisms responsible for environmental loading are temperature, or heat transfer, and moisture exchange between the concrete and the atmosphere. Concrete will absorb and release heat energy in response to temperature changes of its surrounds. The energy transfer caused by temperature is accompanied by elongation or contraction of the concrete material. Similarly, concrete exchanges moisture with its surrounds based on the moisture content of the atmosphere. A loss of moisture is associated with concrete shrinkage and the addition of moisture will result in concrete swell. Typically, the relative humidity of the atmosphere is such that the moisture loss to the atmosphere over time is greater than the water absorption which takes place during and after rain events. As such, shrinkage is generally the main focus when considering moisture exchange with the environment. The sensitivity, or rate of response, of any concrete element to environmental loading is dependent on the material composition and geometrical dimensions of the element. For temperature, such sensitivity is referred to as thermal inertia. Concrete's thermal properties cause a slow response to temperature change when compared to steel but when concrete elements are compared to one another, large, solid concrete sections have greater thermal inertia than small, thin sections. This arises from the inherently longer diffusion paths present in large sections. High thermal inertia is a desired property of an element because smaller deformations would be exhibited when compared to elements with lower thermal inertia for the same change in temperature. For concrete shrinkage or swell, the response of the concrete is dominated by the distance water must travel to and from the concrete's hardened surfaces, which is known as the

diffusion path or distance. Thick sections have long diffusion distances from the centre to the surface of the element, resulting in slow moisture loss or gain and therefore a lower rate of deformation. On the other hand, thinner sections will produce higher rates of deformation because of shorter diffusion paths. Based on the thermal inertia and diffusion paths of concrete, it becomes clear that the type of cross-section selected for bridges will influence the response of the structure to environmental loading. Furthermore, it should be noted that a concrete structure's response to environmental loading differs from dead and live loading because the deformations which arise are unevenly distributed throughout a structure's cross section due to varying exposure levels to the atmosphere.

When any structure is free to move, the contraction and elongation caused by environmental loading can be measured in terms of strain and stresses will not develop within the section. However, when restraint is imposed on the structural element, preventing axial movement, rotation or deflection, stresses correlating to the applied boundary conditions will develop within any cross-section. For example, multi-span bridges have piers which support the deck and prevent deflection, or curvature, therefore curvature stresses will develop through the section. Similarly, continuous beams which are tied into columns or piers are restricted from axial movement and so axial, or effective, stress will develop throughout the beam cross-section. For integral bridges, the decks are connected directly to supporting piers and abutments, restricting both curvature and longitudinal movement. Therefore, both axial and curvature stresses develop within the cross section. While the boundary and support conditions of any structure dictate stress development, the necessity to maintain equilibrium within a cross-section causes additional stress within a section. Such stresses are referred to as self-equilibrating stresses and they develop to maintain compatibility when nonlinear temperature or shrinkage distributions occur within cross-sections. Concrete's low thermal conductivity causes nonlinear temperature gradients through the concrete element's cross section. This not only leads to temperature differentials between the top and bottom of the section, causing curvature, but also generates self-equilibrating stresses throughout the cross-section. Like temperature-induced stress differentials, the variations in shrinkage within a concrete element can also cause varied stress distributions through the cross section regardless of boundary conditions. Therefore, the stress development of any structure is dependent on a complex combination of factors such as external restraint, material composition and cross-section type.

While concrete's compressive strength is advantageous, it is inherently weak in tension. When subjected to tensile stresses which exceed the concrete tensile strength, cracking is a likely occurrence. In general, concrete is assumed to have little to no tensile strength and concrete sections are designed assuming the tensile regions of concrete section are cracked and so the steel reinforcement is designed accordingly. The optimal reinforced concrete design aims to limit the occurrence and widths of cracks within a section because cracking causes conditions for potential corrosion of the reinforcement steel, reducing the expected lifespan of the concrete structure. Environmental loading has the potential to

cause tensile stresses in regions not commonly considered critical for tensile reinforcement or impose additional tensile stress on critical regions determined for dead and live loading. Regardless, the stresses caused by environmental loading need to be accounted for in design to limit crack widths.

It becomes clear that stress development caused by environmental loading needs to be considered in bridge design and that cross-section type will influence the response of any structural element to environmental conditions. Even though bridge cross-sections are larger and are exposed to harsher environmental loading than most reinforced concrete elements, the same principles and trends are applicable to and present in smaller sections and elements. The behaviours of scale model sections are identical to full scale sections in all aspects apart from magnitude and rate of response. Considering the influence of size on thermal inertia and diffusion paths, smaller sections will be more sensitive (quicker to respond) to environmental loading but will show similar trends to large bridge cross-sections, nonetheless. Therefore, scaled T-beam models can also be used to analyse the combined effects of temperature and shrinkage on solid and voided sections and the trends would be applicable to larger spine beam and box girder bridge sections. The advantages of using scaled model T-beams are twofold: the practical plausibility of constructing smaller sections as opposed to full scale bridge sections, while maintaining the ability to observe the behavioural trends applicable to full scale sections; and the opportunity to analyse the effects of environmental loading on sections which are typically sized for beam and slab construction, extending environmental loading applications and required considerations beyond bridge design.

There is a need to develop an understanding of the stress development caused environmental loading of restrained concrete bridge sections. The behaviour of reinforced concrete sections is influenced by cross-section type as it effects the thermal inertia, diffusion path lengths and internal temperature and moisture distributions. It is important to understand the critical conditions for tensile stress development, such that cracking and crack widths can be limited. This can be achieved by analysing the response of statically determinate scale model concrete T-beams with solid and voided cross-sections to natural environmental loading.

## 1.2 OBJECTIVES OF THE STUDY

The main aim of this study was to determine the stress development caused by environmental loading in restrained concrete bridge sections. The investigation was focused on the response and comparison of two scale model T-beams with solid and voided cross-sections respectively, exposed solely to environmental loading conditions. The aim was reached through the primary and secondary objectives detailed below.

The primary objectives of the study include:

- Comparing the response of solid and voided reinforced concrete T-beam cross-sections to temperature and shrinkage variations, which characterises environmental loading. The individual effects of temperature and shrinkage as well as the combined effect were considered.
- Determining the theoretical strain and analysing measured strain, and by extension, calculate stress profiles in both vertical and transverse directions through the cross-sections caused by environmental loading and different restraint conditions.
- Comparing mathematical predictions of strains profiles caused by thermal loading to experimental results to establish whether analytical calculations and assumptions can accurately predict real strain behaviour of reinforced concrete beams.
- Establishing the key parameters and critical restraint conditions responsible for critical tensile stresses development. The tensile stresses were compared to the tensile strength of the concrete.

The secondary objectives of the study include:

- Establishing whether existing South African bridge design codes relating to temperature and shrinkage can be used to include environmental loading in the design of any reinforced concrete elements.
- Determining the magnitude and impact of self-equilibrating stresses individually and on total stress through the solid and voided reinforced concrete cross-sections.
- Investigating whether rainfall should be considered as an important part of environmental loading conditions and considerations.

### **1.3 SCOPE OF THE STUDY**

The scope of the study was limited to experimental results and analytical calculations of scale model concrete T-beams exposed to environmental loading for applications in bridge design as well as in typical reinforced concrete beams. Two cross-sections were considered: a solid T-beam to mimic the behaviour of solid spine beam bridge decks as well as a voided T-beam to mimic box girder sections. The T-beams were cast with a single concrete batch and mix design, therefore, only a single source of aggregate and cement type were considered. The beams remained unsurfaced throughout the study and only the perpendicular ends were sealed to prevent moisture exchange with the environment, thereby emulate continuous conditions. The T-beams contained identical steel reinforcement and a single geographic location was used. Furthermore, only 6 months of data was recorded and analysed for this study. The time period included the seasons of Autumn, Winter and Spring.

### **1.4 METHODOLOGY**

Two T-beams with solid and voided cross-sections respectively, were cast and remained outside the Civil Engineering Laboratory of the University of Pretoria for the duration of the study. The beams were exposed solely to environmental loading, including the effects of direct sunlight and rainfall. The beams were supported to be statically determinate and were free to deform, making length change and therefore strain measurement possible. The T-beams were instrumented with gauges to record temperature and strain measurements for a time period of 6 months, starting at the time of casting. The temperature measurements were used to calculate effective temperatures and theoretical stresses caused by varied restraint while the strain measurements were used to verify the accuracy of theoretical calculations as well as determine the effective and differential shrinkage through the beams, along with the associated stresses. Concrete specimens which were used to determine the material properties applicable to the different strain and stress calculations, were cast and placed alongside the T-beams. The specimens were exposed to the same environment as the T-beams to produce representative values. Furthermore, the various components of thermal and shrinkage stress were mathematically calculated from the recorded measurements and evaluated individually and in combination to determine the key parameters responsible for critical tensile stress development caused by environmental loading in both T-beams.

## 1.5 ORGANISATION OF THE REPORT

The report consists of the following chapters and appendices:

- Chapter 1 serves as introduction to the report. It summarizes the objectives, scope, methodology and organisation of the report.
- Chapter 2 contains the literature study.
- Chapter 3 describes the experimental work and setup used for the study.
- Chapter 4 details the measured temperature and strain trends of the solid and voided T-beam cross-sections. In addition, the comparison of thermal stresses developed in each cross-section for a typical day is included. Furthermore, the comparison of measured and calculated strains is presented.
- Chapter 5 provides an overview of stress development from concrete final setting time. The individual components of temperature and shrinkage as well as their combined effect are investigated. The stress development for different restraint conditions is compared to the tensile capacity of the concrete to identify the possibility of cracking with different restraint conditions over time.
- Chapter 6 concludes with the main conclusions of the study and recommendations for further research and suggestions for design and construction of restrained reinforced concrete elements exposed to environmental loading.
- Appendix A contains the calculations for vertical temperature distributions according to TMH7:1981 Parts 1&2 as well as the calculations for predicted shrinkage according to TMH7:1989 Part 3.

## 2 LITERATURE REVIEW

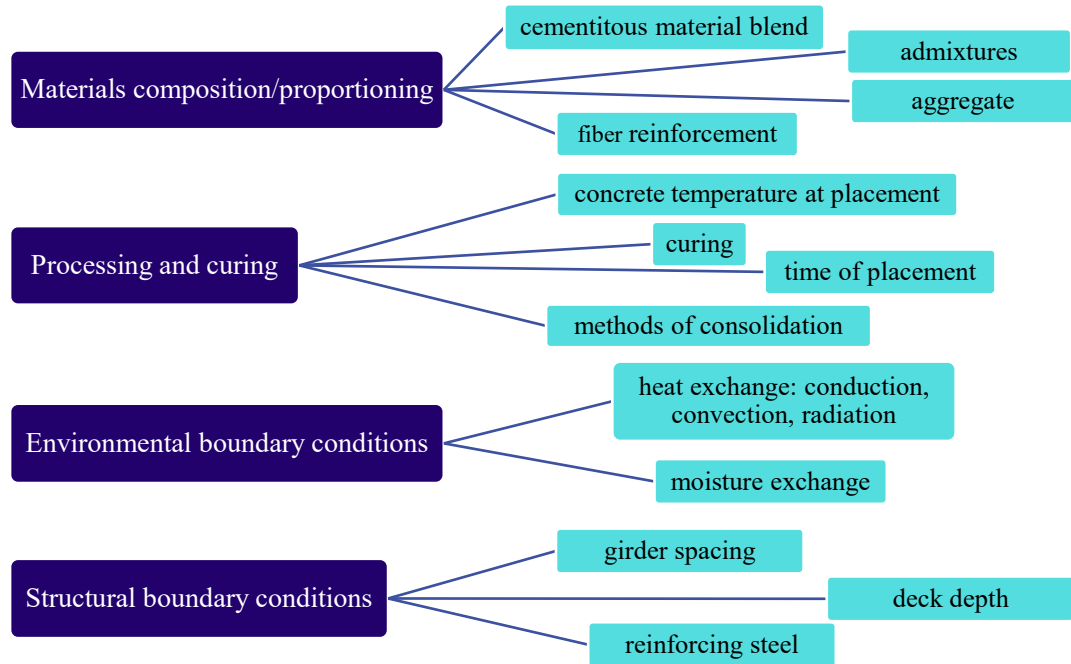
### 2.1 INTRODUCTION

This chapter serves to provide background knowledge on the extent of and the factors influencing the cracking of restrained reinforced concrete elements. The observed transverse cracking of various bridges and the specific effects of temperature and shrinkage are discussed. Furthermore, summaries are given of previous works based on experimental and numerical results.

### 2.2 CRACKING OF REINFORCED CONCRETE

Reinforced concrete is an omnipresent construction material and an integral part of human society. Its versatility, durability and availability, ensures its continued importance for all types of construction throughout the world. Structural concrete contains steel reinforcement to compensate for the low tensile strength of concrete (Naaman, 2001; Soutsos & Domone, 2017). Nonetheless, transverse cracks develop in restrained structural concrete when longitudinal tensile stresses exceed the tensile strength of the concrete. Since strain alone will not induce stress, tensile stresses develop when the concrete is prevented from making volumetric changes by a source of restraint. Significant durability and serviceability problems can arise from cracked concrete exposed to the environment as cracks provide avenues for corrosive agents to reach the embedded reinforcement. With premature and accelerated corrosion of reinforcement, the concrete's service life is substantially reduced (Nair et al., 2016).

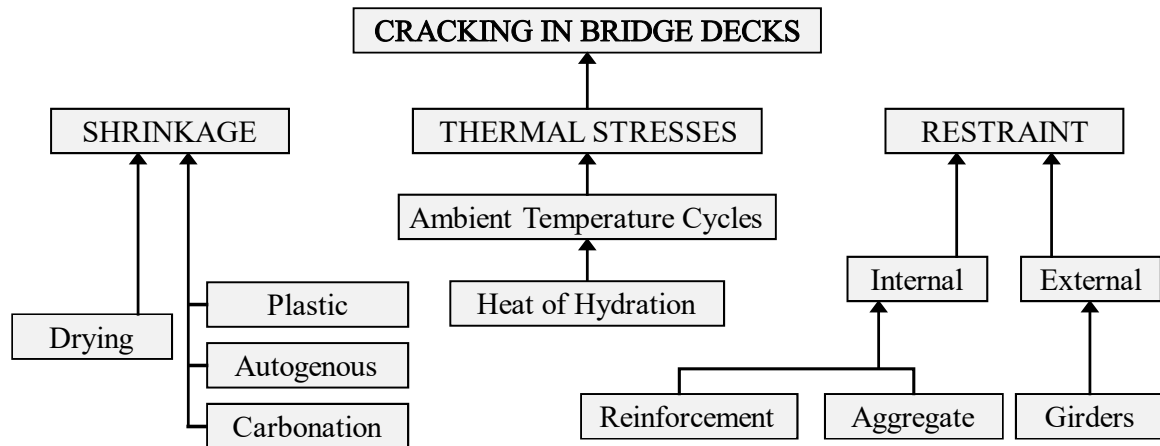
There are a multitude of factors which influence the cracking potential of concrete. Bolander (2018) categorized factors affecting cracking potential into four main groups as shown in **Figure 2-1**: 'Materials composition and proportioning'; 'Processing and curing'; 'Environmental boundary conditions' as well as 'Structural boundary conditions'. The first two categories have been studied extensively over the past several decades (Hadidi & Saadeghvaziri, 2005). While the cracking potential of concrete will be affected by the material composition and processing and curing, the environmental and structural boundary conditions will depend on the type of structure it forms part of. For example, some concrete members are somewhat sheltered from environmental conditions such as solar radiation and rain - as is the case for beams and slabs within buildings. The structural boundary conditions, characterized by the degree of restraint against axial and rotational movement, of a concrete element will also vary depending on its position and purpose.



**Figure 2-1 Design parameters affecting early-age concrete cracking**  
 (Adapted from Bolander et al., 2018)

Bridges are exposed to harsh environmental conditions and can have varying boundary conditions. As such, this literature review will primarily focus on concrete bridge decks and the different components related to their cracking. In 1996, Krauss & Rogalla completed a comprehensive report, the objective of which was to determine the major factors or combinations of factors which contribute to transverse bridge deck cracking of newly constructed bridges. The report further presents recommended guidelines for preventing the occurrence of such transverse cracking. In a survey completed for the report, respondents estimated that more than 100 000 bridges in the United States developed early age transverse cracking. The transverse cracks are typically full depth cracks along the length of the span approximately 1-3m apart. The survey included both steel-concrete composite and purely concrete bridges. Nonetheless, the primary factors found to affect the transverse cracking of concrete bridge decks, aside from the concrete composition, were shrinkage and temperature changes. Interestingly, the report found that heavy traffic volumes may ravel cracks, making them more visible but no evidence was found that daily traffic affected bridge deck cracking. Like Krauss & Rogalla (1996), Brown et al. (2001), presents shrinkage and thermal stresses as the major causes of bridge deck cracking. However, Brown et al. (2001) includes the concepts of internal and external restraint (**Figure 2-2**).





**Figure 2-2 Causes of bridge deck cracking  
(Adapted from Brown et al., 2001)**

Numerous authors have also documented extensive transverse cracking in their findings. French et al. (1999), presented a field investigation of 72 bridges including simply supported, prestressed girder, continuous steel girder and wide-flange girder bridges, the majority of which had developed transverse cracks in the concrete decks. It was concluded that differential shrinkage was the main cause of deck cracking. However, end conditions had a great effect on the extent of the transverse cracking, with the most extensive cracking associated with full restraint at either end. Furthermore, Frech et al. (1999) reported that transverse cracking was more prevalent in continuous spans compared to simple spans. William et al. (2008), Sharp & Moruza (2009), and Nair et al. (2016), reported transverse cracking in bridge decks attributed to drying shrinkage shortly after construction was completed. Thermal stresses induced within bridge decks are inevitable, whether from heat of hydration or daily and seasonal temperature cycles. Therefore, temperature conditions may also create tensile stresses large enough to induce transverse cracking (Maher, 1970; Priestly, 1976; Elbadry & Ghali, 1986; Brown et al., 2001; Feng et al., 2022).

Throughout literature, the main parameters responsible for transverse bridge deck cracking are stresses produced due to the restraint against movement or strain resulting from shrinkage and temperature variations. To better understand these primary causes of transverse cracking, the mechanisms behind concrete's response to temperature and shrinkage must be discussed. Therefore, the remaining literature review will focus on not only the thermal stresses caused by concrete's temperature response but also on concrete shrinkage. The restraint conditions will be discussed as part of each relevant section.

## 2.3 THERMAL STRESSES

Reinforced concrete structures are often exposed to thermal loadings, whether by design or otherwise. The thermal loads may be because of heat of hydration, solar radiation, ambient air temperature, service function or accidental loads such as fire. Thermal loading may seriously affect serviceability and structural integrity and must therefore be considered in the design of structures (Radolli & Green, 1975; Vecchio, 1986; Feng et al., 2022). The literature reviewed in this section focuses on the thermal strains and stresses generated in typical bridge sections by heat of cement hydration and temperature gradients produced by environmental conditions. These stresses may also be applicable to other reinforced concrete structures under certain circumstances. The temperature gradient design of concrete bridge sections according to the code for the design of highway bridges and culverts in South Africa is also discussed.

### 2.3.1 Heat of Hydration

Cement hydration is an exothermic reaction, therefore heat will be generated while concrete is poured and sets, before it cools down to ambient temperature. The amount of heat generated is directly related to the cement content per m<sup>3</sup> of concrete. When concrete is cast into a structure, heat produced by cement hydration will gradually be lost to the surrounding environment directly or through formwork. In some cases, elements are thick enough to create adiabatic conditions for the central regions of the concrete, which can result in the element achieving final set at a high temperature. As the hardened concrete cools down and thermally contracts, tensile stresses due to restraint may be of sufficient magnitude for the concrete to crack. The restraint may be caused by the surrounding structure and the reinforcement (Soutsos & Domone, 2017).

The considerations given to thermal stresses from heat of hydration in concrete primarily relate to concerns about cracking in mass concrete. According to ACI PRC-207.1-21 (2022), mass concrete can be divided into two classifications which are traditional mass concrete and thermally controlled concrete or reinforced structural mass concrete (RSMC). Both types have similar principles and basic assumptions, but RSMC consists of individual or distinct placements often constructed with commercial ready mixed concrete. In comparison traditional mass concrete refers to the concrete of structures such as dams, where the structure is constructed of intertwined placements. Furthermore, Bartojay (2012) describes RSMC as having higher cementitious material contents to produce higher compressive strength at early ages which subsequently leads to higher potential temperature rise. Even though mass concrete can be classified into these two types, there is no universally accepted definition for 'mass concrete' based on concrete characteristics or placements that require control of temperatures and temperature differences. ACI Concrete Terminology defines mass concrete as "*any volume of structural concrete in which a combination of dimensions of the member being cast, the boundary conditions, the*

*characteristics of the concrete mixture, and the ambient conditions can lead to undesirable thermal stresses, cracking, deleterious chemical reactions, or reduction in the long-term strength as a result of elevated concrete temperature due to heat from hydration”* (ACI Committee 207, 2022). This definition is devoid of definitive guidance related to the physical characteristics or dimensions of mass concrete. As such, the only distinguishing characteristic of mass concrete compared to other concrete work is its thermal behaviour which may cause loss of structural integrity and monolithic action (ACI Committee 207, 2022).

It should be noted that the thermal stress and potential cracking in mass concrete is focused on the restraint provided by the element itself due to its temperature differential. After set, the exterior concrete experiences thermal volume contraction as the outer regions are subject to greater heat losses. The exterior contraction is restricted by the high temperature expansion of the interior concrete, which has delayed temperature reduction due to a low thermal conductivity of the concrete material. When the thermal stress surpasses the tensile strength of the concrete, thermal cracking occurs along the exterior of the element (Bartojay, 2012). Furthermore, ACI SPEC-301-20 (2020) states that the maximum temperature in mass concrete after placement should not exceed 70 °C; and the maximum temperature difference between the centre and the surface of placement should not exceed 19 °C. Some of the parameters which influence heat of hydration temperatures are concrete composition, initial temperature, pouring sequence and shutter material. There are measures which can be put in place to reduce the peak temperature reached during concrete hydration namely reducing cement content (or increasing the use of pozzolans), using chilled water and casting in the evening (Krauss & Rogalla, 1996; Han et al., 2023).

However, temperature difference may cause thermal cracking even in structures not typically deemed large enough to be considered mass concrete, such as box girders for bridge construction (Han et al., 2023). Do et al. (2021a) stated that bridge structures often use high strength concrete with a higher cement content for early strength gain. When comparing high strength concrete (HSC) (> 65 MPa) to normal strength concrete (< 45 MPa), Do et al. (2020) found the HSC to have a greater temperature difference during hydration indicating a greater risk for thermal cracking. Furthermore, the authors predicted thermal stresses could be kept below the tensile strength of the HSC if insulation blankets were used to cover the structures.

Do et al. (2021b) analysed the impact of local volume-to-surface area ratio ( $V/A$ ) on the development of heat from cement hydration and found that high strength concrete segmental box girder diaphragms could generate temperature differentials of up to 32 °C, far exceeding the guide of 19 °C. Even with a high-volume fly ash mix, Do et al. (2021b) reported temperature differentials of approximately 20 °C. Similarly, Tia et al. (2016) reported that local  $V/A$  ratios (which exclude extremities) were a more

appropriate method than overall V/A ratios in classifying segmental bridge sections as mass concrete. Tia et al. (2016) recommended that a thermal analysis should be conducted if the V/A ratio exceeds or nears 0.3 m (1 foot). However, it should be noted that the V/A described by Tia et al. (2016) will only be specifically applicable to segmental sections because the area used in the ratio includes all the exposed surfaces of a segment, which is considerably larger than would be the case for continuous sections.

Weather conditions during casting may greatly affect the temperature and by extension the thermal stress which causes cracking within concrete. According to Hadidi & Saadeghvaziri (2005), both hot and cold conditions increase cracking and some guidelines were proposed for the ambient and concrete temperatures at placement:

- Minimum and maximum ambient temperature of 4 °C and 32 °C respectively (French et al., 1999)
- Maximum concrete temperature at concrete placement 27 °C (Krauss & Rogalla, 1996)

Throughout literature, the stresses caused by heat of hydration is focused on the temperature differential within the structure and very little emphasis is placed on the longitudinal axial contraction after final set resulting from the temperature decline as the heat from cement hydration dissipates. In general, such contraction and longitudinal movement because of shrinkage and creep is of little concern since it is provided for in most structures with expansion joints or bridge bearings (Reynolds & Emanuel, 1974; Roeder, 2003). For the cases where beams and slabs are cast monolithically with support structures or in the absence of bearing supports, the decrease in temperature after set and the associated volume contraction of the concrete can produce tensile stresses which exceed the tensile strength of the concrete. According to Krauss & Rogalla (1996), when bridge deck slabs are cast monolithically with concrete girders, thermal shrinkage stresses are reduced when compared to separate casting of the slab onto the girders because both the girders and deck generate heat and cool down concurrently, which reduces temperature differences. Nonetheless, it should still be noted that thinner parts will lose heat more rapidly compared to thicker parts and temperature differentials will still exist between the deck and the girders even if cast monolithically.

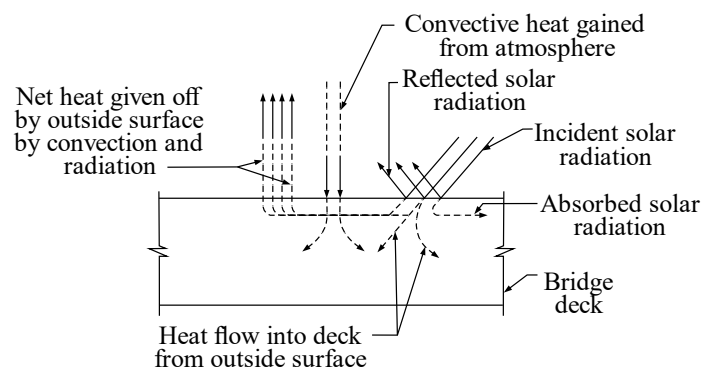
### 2.3.2 Temperature Distributions and Restraint

Reinforced concrete bridges are predominantly completely exposed to outside environmental conditions and as such the bridge superstructures are either heated or cool by the following points outlined by Radolli & Green, (1975):

- Convection to or from the surrounding atmosphere;
- Radiation from the sun; and
- Radiation from the sky or surrounding objects

The temperatures created vary as result of geometry, latitude of locality, orientation of the bridge deck to the sun, time of day and season, degree of cloudiness and relative humidity, nature and colour of the bridge deck surface, and thermal properties of the constituent materials of the bridge.

The above listed factors are depicted in **Figure 2-3** and are directly related to diurnal and seasonal temperature fluctuations amongst other factors. The seasonal variation of mean bridge temperature causes overall longitudinal expansion or contraction for simple spans and end moments and forces for restrained or continuous spans. The degree of restraint depends on the design characteristics of the structure such as the boundary conditions and relative stiffness between segments.




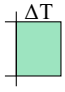
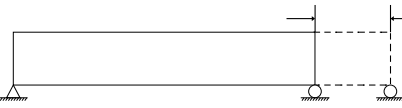

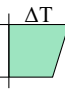
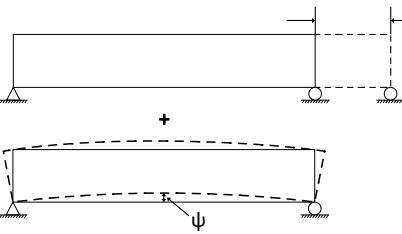

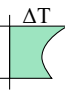
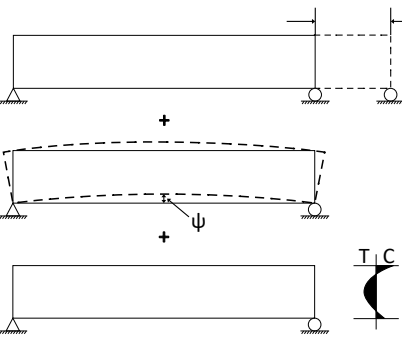
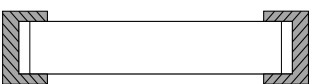
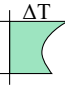
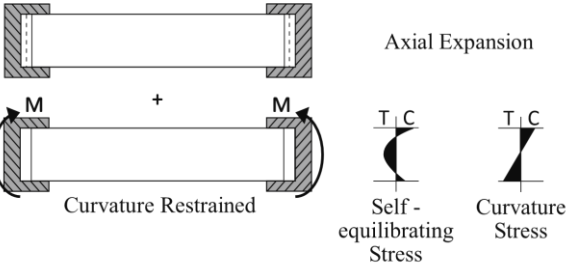
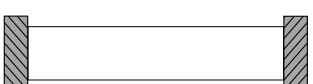
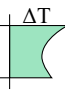
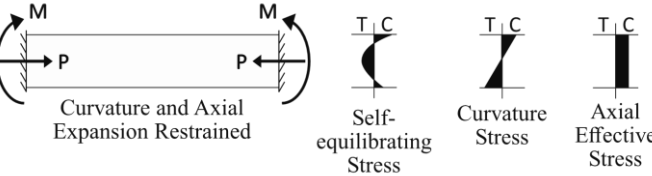
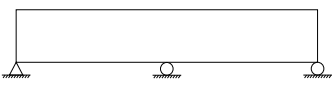
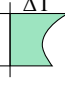
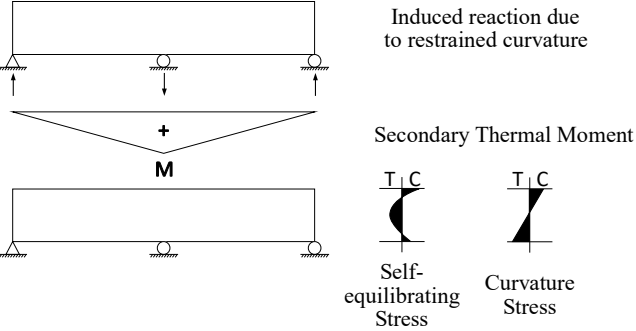
**Figure 2-3 Heat flow in an exposed bridge deck  
(Adapted from Radolli & Green et al., 1975)**

Concrete has high specific heat and low thermal conductivity and therefore large temperature variations can occur through the depth of a cross section with daily temperature cycles. With the implementation of longer spans and deeper sections in bridge construction, the temperature differentials within concrete elements have become of interest due to the potential to cause stresses of equal and greater magnitude than live load stresses (Potgieter, 1983). As such, many authors have studied temperature distributions which develop through the depth of concrete bridge decks and proposed various temperature prediction models including an array of input parameters (Priestly, 1978; Potgieter, 1983; Song et al., 2012; Feng et al., 2022). Temperature distributions can be described as uniform, linear or nonlinear and the stresses which develop in concrete elements due to temperature variations are dependent on the restraint

conditions as well as temperature distributions. Uniform distributions occur when the temperature throughout the section is constant therefore the expansion or contraction is constant from top to bottom of the member. Linear temperature distributions have a linear temperature gradient between the top and bottom of the member. With a higher temperature at the top upward hogging is caused if the member is not restrained. Similarly, sagging is caused by a greater temperature at the bottom of the element when compared to the top. Nonlinear temperature distributions have parabolic- or hyperbolic- like shapes for which the aforementioned authors used multivariable equations to quantify and predict. Even though the temperature varies through the element for a nonlinear temperature distribution, the top may still have a higher or lower temperature when compared to the bottom of the element, causing hogging and sagging as described for linear temperature distributions. Furthermore, for nonlinear temperature distributions, stresses referred to as self-equilibrating stresses are developed and can be derived from basic equilibrium criteria (Priestly, 1972). Self-equilibrating stresses arise due to incompatibility between the two requirements that plane sections remain plane according to Euler-Bernoulli beam theory, and that individual fibres would expand by an amount proportional to local temperature rise, if not restrained by adjacent fibres (Priestly, 1978; Elbadry & Ghali, 1986; Vecchio, 1987). Therefore, self-equilibrating stresses are produced due to nonlinear temperature distributions regardless of boundary condition.

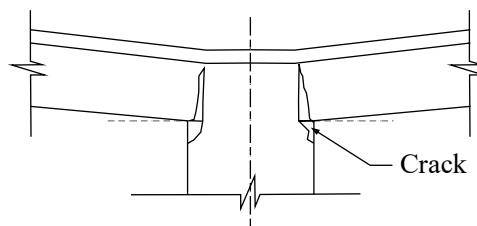
**Table 2-1** contains the induced thermal effects produced by different temperature distributions and boundary conditions on beam elements adapted from Radolli & Green (1975). In structures (a) and (b) only strains are produced because the boundary conditions allow axial expansion and hogging curvature due to (a) uniform and (b) linear temperature distributions respectively. Structure (c) has the same boundary conditions, but a nonlinear temperature distribution is applied causing self-equilibrating stresses. For structure (d), curvature ( $\psi$ ) is restrained and therefore curvature stresses are produced in addition to the self-equilibrating stresses due to the nonlinear temperature distribution. According to Elbadry & Ghali (1986), the curvature stresses are large in shallow sections, while the self-equilibrating stresses are large in deep sections. Structure (e) has the same curvature restraint as structure (d), but axial deformation is also restrained, therefore in addition to the self-equilibrating and curvature stresses, an axial effective stress is induced. The axial movement and therefore stress is governed by the section's effective temperature, which is described as a weighted average temperature of the section (Emerson, 1976). In continuous bridge decks where axial deformation is permitted, but restraint of upward (or downward) deflection is provided by internal supports, the induced effects are as given for structure (f). In this scenario, only curvature and self-equilibrating stresses are applicable. It should be noted that structure (e) would be applicable to continuous, tied-in beams present in most structures and integral bridges. For each case, the induced stresses must be added together to obtain the total thermal stress relevant to the structure. If the total thermal stresses in tension exceed the tensile strength of the concrete, cracking is likely to occur.

**Table 2-1 Induced thermal effects of temperature distributions and restraint**

| Structure  | Temperature distribution   | Induced thermal effect  |
|--|--|---|
|  <p>(a)</p>   |  <p>Uniform</p>     |  <p><math>\alpha\Delta T</math><br/>Axial Expansion</p>   |
|  <p>(b)</p>   |  <p>Linear</p>      |  <p><math>\alpha\Delta T_{\text{mean}}</math><br/>Axial Expansion</p> <p>Induced Curvature</p>  |
|  <p>(c)</p>   |  <p>Nonlinear</p>   |  <p><math>\alpha\Delta T_{\text{mean}}</math><br/>Axial Expansion</p> <p>Induced Curvature</p> <p>Self-equilibrating Stress</p>                |
|  <p>(d)</p> |  <p>Nonlinear</p> |  <p>Axial Expansion</p> <p>Curvature Restrained</p> <p>Self-equilibrating Stress</p> <p>Curvature Stress</p>                                  |
|  <p>(e)</p> |  <p>Nonlinear</p> |  <p>Curvature and Axial Expansion Restrained</p> <p>Self-equilibrating Stress</p> <p>Curvature Stress</p> <p>Axial Effective Stress</p>       |
|  <p>(f)</p> |  <p>Nonlinear</p> |  <p>Induced reaction due to restrained curvature</p> <p>Secondary Thermal Moment</p> <p>Self-equilibrating Stress</p> <p>Curvature Stress</p> |

\*(adapted from Radolli &amp; Green,1975)

The curvature stresses induced by linear or nonlinear temperature distributions are produced due to the prevention of curvature in statically indeterminate structures. The bending moments in indeterminate structure are proportional to the statically determinate curvature ( $\psi$ ) and the section's flexural rigidity. Therefore, curvature stresses will be dependent on the number and length of spans for a given structure. The studies conducted by Krauss & Rogalla (1996) and French et al. (1999) concluded that cracking was more prevalent for continuous spans than simple spans and for the continuous spans more cracking was observed in the middle spans than the end spans. The secondary thermal moments can be calculated using a compatibility or an equilibrium method (Clark, 1983). However, Vecchio (1987) stated that the application of conventional analysis techniques are not directly applicable to thermal loadings since the thermal stresses are partially governed by the effective stiffness of the member. The effective stiffness of a member is altered as cracks develop and propagate within concrete, thus causing relaxation in secondary thermal moments. Analytical methods proposed by Thurston (1978) and Vecchio (1987) which adequately account for factors of concrete tension, tension stiffening after cracking, nonlinear thermal distributions and nonuniformly cracked members, have however been substituted by commercial finite element analysis techniques (El-Tayeb et al., 2017). Accurate calculations of the bending moments are important in design as inadequate continuity reinforcement in beams and columns or piers will result in prying forces causing damage as shown in **Figure 2-4**.

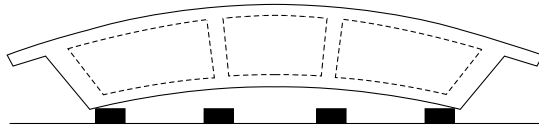


**Figure 2-4 Damage at support due to prying forces  
(Adapted from Elbadry & Ghali, 1986)**

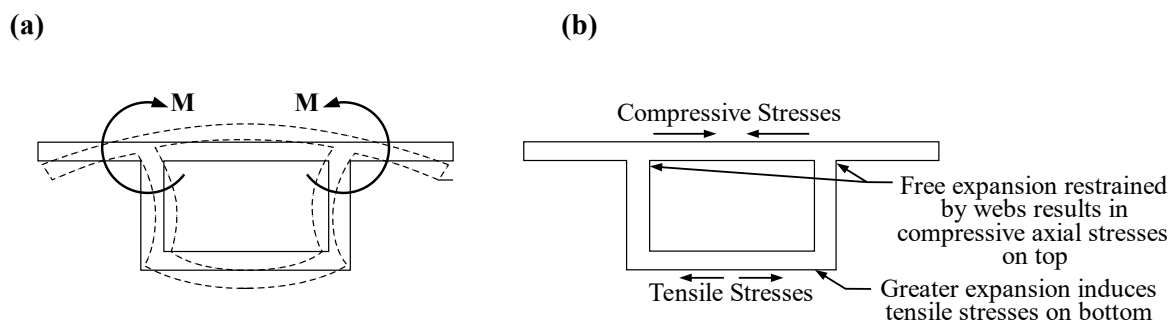
Discussions on thermal stresses relating to temperature distributions have been limited to concrete box-girders where temperature varies with depth but not in the transverse direction. This assumption can be justified for box-girders by the reasoning that the cantilever deck sections provide considerable shade to the webs and therefore when compared to the stresses produced by the vertical temperature distribution, the transverse stresses induced are unlikely to be significant. However, Priestly (1972) noted that the transverse effects can sometimes be critical for wide sections where outside bearings become overloaded due to transverse upward hogging of the end diaphragm deck cross section shown in **Figure 2-5**. Furthermore, transverse tensile stresses of up to 3.5 MPa are possible due to restrained transverse hogging in box girders (Leonhardt & Lippoth, 1970) as depicted in **Figure 2-6 (a)**. As is true for the longitudinal direction, with an increase in temperature the top deck will tend to expand in the transverse direction. For a box girder, the free expansion will be restricted by the webs and thus create compressive stresses in the deck and by extension tensile stresses in the bottom slab (**Figure 2-6 (b)**).



The authors also noted the development of bending stress within the webs due to the change in temperature of the top deck, however such bending stresses fall outside the scope of this study and will therefore not be discussed. Even though Priestly (1972), Clark (1983), Elbadry & Ghali (1986) as well as Larsson & Thelandersson (2012) have mentioned the importance of both directions, transverse stresses are not typically a primary concern in literature.



**Figure 2-5 Overloading of outside bearings due to transverse hogging of end diaphragm (Adapted from Priestly, 1972)**



**Figure 2-6 (a) Transverse constrained bending stresses and (b) axial stresses (Adapted from Radolli & Green et al., 1975)**

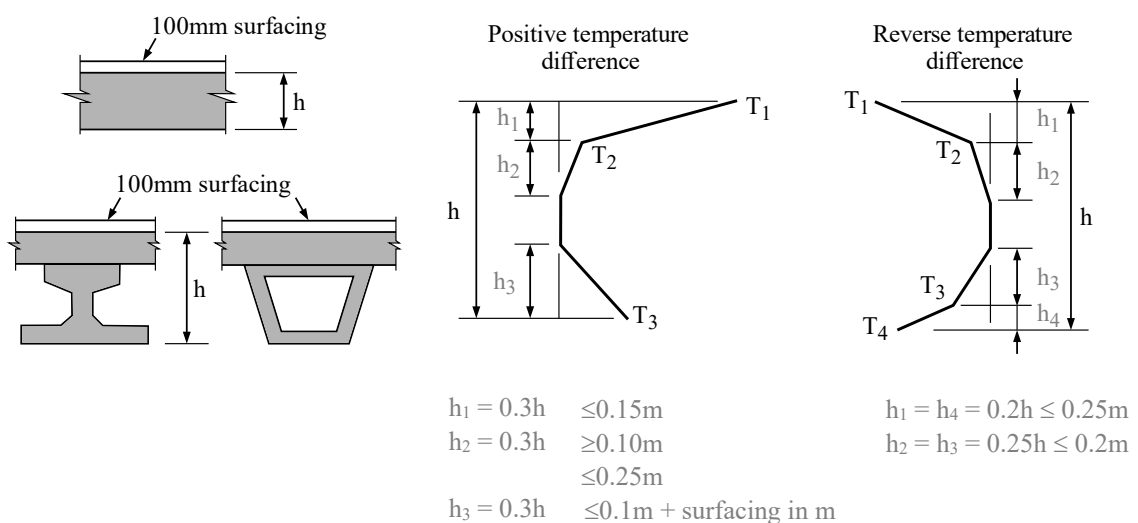
It should be highlighted that both the stress caused by restraint in integral structures and movement in structures with expansion joints due to temperature are important. For bridges which are free to move longitudinally, bridge engineers have few problems caused by thermal movements, but the correct selection and design of joints are dependent on accurate movement predictions. The general understanding related to stress developments due to temperature in integral structures is also important (Roeder, 2003).

Ng et al. (2011) defines thermal inertia as “*the property of a material that expresses the degree of slowness with which its temperature reaches that of the environment*”. Concrete’s high specific heat and low thermal conductivity yields a slow response to temperature change, resulting in a high thermal inertia compared to steel. However, the thermal inertia of a concrete member can be altered by changing its cross-section – more specifically the area of the cross section per unit width (Emerson, 1976; Skorpen, 2020). By increasing the ratio of area per unit width, the thermal inertia of the section is also increased. Therefore, sections which have solid cores would have higher thermal inertia compared to voided sections with the same external dimensions. Sections with higher thermal inertia will also have a smaller deformation response to changes in environmental temperature because the section itself

absorbs or releases large amounts of heat before its mean temperature changes. Considering restrained deformations result in stresses, sections with high thermal inertia could be beneficial in minimising tensile stresses created by temperature fluctuations.

### 2.3.3 TMH7:1981 Temperature Guidelines

In South Africa the design of bridges often refers to the Code of Practice for the Design of Highway Bridges and Culverts in South Africa (TMH7:1981 Parts 1&2). According to TMH 7:1981 Part 1&2, the daily and seasonal fluctuations in shade temperature, solar radiation and re-radiation cause changes in the overall bridge temperature (effective bridge temperature) creating temperature gradients through the depth of bridge cross sections. Furthermore, the code provides a temperature distribution guideline based predominantly on location, minimum and maximum effective bridge temperatures and the type of construction. **Figure 2-7** shows the temperature distributions for both positive and negative temperature differences as prescribed by TMH7:1981 Part 1&2 for concrete bridge construction. Positive temperature differences occur when conditions cause heat gain through the top surface of the superstructure which would typically occur in the afternoon after hours of surface exposure to direct sunlight. Conversely, reverse temperature differences typically occur early in the morning after heat is lost through the top surface of the bridge deck at night. The values of  $T_1$  to  $T_4$  are determined by the maximum and minimum effective bridge temperatures which are calculated from isotherms of shade air temperatures in South Africa presented in TMH7:1981 Part 1&2. The extrema are adjusted for depth of slab ( $h$ ) as well as for type and thickness of surfacing before being applied to create the temperature distribution guidelines as shown in **Figure 2-7**. Since temperature distributions are not considered in the design of typical beams and slabs, TMH7:1981 could potentially provide guidance on distribution shapes.



**Figure 2-7 Temperature distribution guidelines for concrete elements  
(Adapted from TMH7:1981 Part 1&2)**

## 2.4 SHRINKAGE

Shrinkage is an inevitable volume deformation of concrete, in both fresh and hardened states throughout its service life. While still in the plastic state, concrete may experience plastic shrinkage due to water evaporation and bleeding. Furthermore, a volume reduction occurs within concrete because of the internal consumption of water in cement hydration creates hydration products of lesser volume than the original constituents. This volume reduction causes the system to contract and is called chemical shrinkage. It is generally accepted that the majority of chemical shrinkage occurs when hydration proceeds rapidly but it continues over time (Soutsos & Domone, 2017). Drying shrinkage is the additional shrinkage caused by moisture loss from the concrete, over and above chemical shrinkage. In normal strength concrete, chemical shrinkage is typically at least an order of magnitude smaller than drying shrinkage that takes place over an extended period of time. The combination of the various types of concrete shrinkage results in free strain that typically surpass the tensile capacity and therefore if the concrete is restrained, it will crack (Alexander, 2021). It is important to highlight that the shrinkage of concrete is affected by various factors incorporated into the mix design such as water-cement ratio, cement composition, admixtures, aggregate type and fine to coarse aggregate proportion. These factors fall outside the scope of this study and will not be discussed.

The volume changes in hardened concrete due to environmental effects such as moisture loss or gain will be the primary focus of this section as thermal shrinkage was discussed as part of heat of hydration in **Section 2.3.1**. Furthermore, shrinkage referred to in this section is the combination of early age shrinkage and drying shrinkage, as both relate to the exchange of moisture and occur simultaneously. The shrinkage guideline presented in TMH7:1989 Part 3 is also discussed.

### 2.4.1 Differential Shrinkage

It is widely accepted and reported that size and shape influence the drying shrinkage of concrete (Alumudaiheem & Hansen, 1987; Bissonnette et al., 1999; Al-Saleh & Al-Zaid, 2006; Soutsos & Domone, 2017; Samouh et al., 2018; Zhang & Hubler, 2020). Drying of concrete occurs from exposed surfaces and by altering the geometry and dimensions of members, the moisture diffusion paths are also changed and therefore the rate and amount of shrinkage is affected. It stands to reason that longer moisture diffusion paths lead to lower shrinkage rates. As such, when exposed to the same conditions smaller sections have higher shrinkage rates and larger section lower shrinkage rates. However, the ultimate drying shrinkage of concrete is independent of shape and size (Alumudaiheem & Hansen, 1987; Kristek et al., 2005; Samouh et al., 2016).

The size effect has been taken into account through the use of an effective thickness by various shrinkage predictive models such as: ACI 209.2R-08 (2008), Rilem Models B3 and B4 (Bazant & Murphy, 1995; Wendner et al., 2013), Eurocode 2 (EN 1992-1-1:2004), fib MC2010 (2013) and

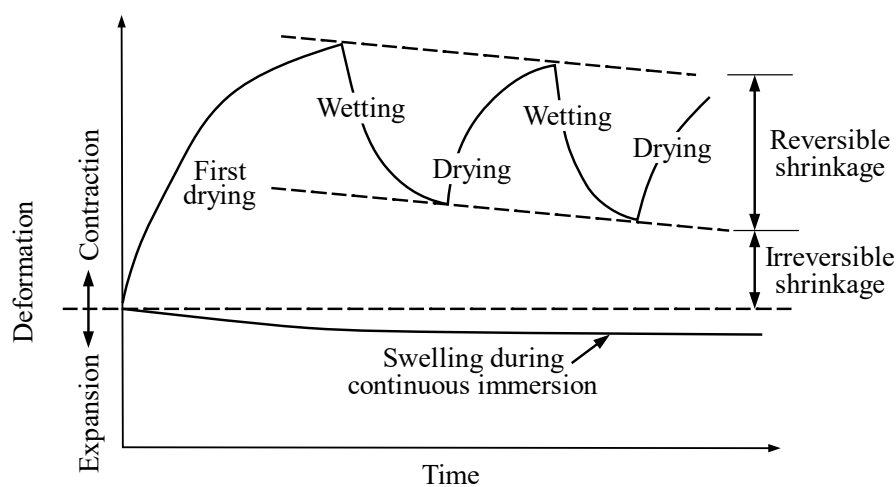
TMH7:1989 Part 3. The effective thickness can also be expressed as a volume-to- surface ratio and is based on the diffusion analysis of drying. TMH7:1989 Part 3 describes the effective thickness as the ratio of the area of the section to the semi-perimeter in contact with the atmosphere.

Throughout literature ‘differential shrinkage’ can have two possible interpretations. The first links to the moisture difference between the surface region and the centre, or core, of an element. The core region will undoubtedly have a higher moisture content than the surface and therefore a strain gradient exists through the depth of the member and the surface regions have a greater tendency to crack (Bissonnette et al., 1999). The second interpretation links to the difference in shrinkage between different parts of the same structure, that is in terms of varying thicknesses or age, as is the case with concrete T-beams, overlays cast on top of mature concrete and staged construction (Priestly & Wood, 1977; Silfwerbrand, 1997; Issa, 1999; Orta & Bartlett, 2014; Kadlec et al., 2017, Chijiwa et al., 2018). Orta & Bartlett (2014) stated that for bridge deck rehabilitation, a concrete overlay is often cast against sound, mature concrete (substrate). The rate of shrinkage of mature concrete is much slower than the fresh overlay and therefore the shrinkage of the overlay is restrained at the interface with the substrate. The restraint caused by the different shrinkage rates causes tensile stresses in the overlay which may be large enough to cause cracking. A similar mechanism occurs in concrete members which have varying thicknesses within the cross section. Since thinner sections will initially have higher shrinkage rates in comparison to thicker parts, in cross sections such as T-beams, stresses will develop at the intersection between the different thicknesses due to differential shrinkage. To the same effect, Priestly & Wood (1977) reported significant prestress redistribution in a complex trapezoidal box-girder bridge due to the shrinkage and creep differences of the soffit slab, deck slab and webs in the box-girder. According to Alexander (2021), shrinkage may affect the deflections of flexural members based on the positioning of the tensile reinforcement. For unsymmetrically reinforced members, greater free shrinkage of the concrete will be experienced in the compression zone than in the heavily reinforced tension zone, where the restraint caused by the reinforcement is greater (Gao et al., 2012). Consequently, the shrinkage of the concrete will increase the curvature and hence the deflection of the concrete member (Mosley et al., 2012). It follows that if the induced curvature is restrained by imposed boundary conditions, stresses will be induced in the member.

### 2.4.2 Environmental Effects

Concrete's composition, dimensions and geometry will affect its shrinkage but the environment in which it is placed will also have an influence. The environment comprises the extent of curing and the subsequent drying conditions, which includes weather conditions such as rain. According to Alexander (2021), the length of the curing period is generally not an important factor which influences normal-strength concrete shrinkage. Nonetheless, adequate and timely curing is a key factor to reducing cracking (Hadidi & Saadeghvaziri, 2005). Relative humidity has a direct impact on shrinkage strains. Bissonnette et al. (1999) reported a linear relationship between relative humidity and relative shrinkage for various specimen sizes and water-cement ratios. Similarly, Baroghel-Bouny & Godin (2001) found a linear relationship between relative humidity and shrinkage strains for a study conducted on a large range of concrete mixes.

The influence of temperature on drying shrinkage depends on the moisture condition experienced by the concrete as well as its age. For example, steam curing reduces shrinkage, but elevated temperatures increase drying shrinkage for mature concrete (Alexander, 2021). While the impact of rain is largely neglected in literature, some shrinkage will be reversed with the addition of water as is the case for the drying and wetting cycles depicted in **Figure 2-8** (Soutsos & Domone, 2017). The durations of rain events are typically not long enough to reverse all reversible shrinkage but will have a definite impact on the strains within the concrete. Chijiwa et al. (2018) confirmed that the influence of rain was not negligible in a study aimed at determining the cause of excessive deflections. For the experiment, scale box sections were cast outside and a comparison was made between sections completely exposed to the environment and protected by a roof structure. The authors concluded that the curvature and associated deflections of the box sections were influenced by yearly precipitation.



**Figure 2-8 Response of concrete to cycles of alternate drying and wetting (Adapted from Soutsos & Domone, 2017)**

### 2.4.3 TMH7:1989 Shrinkage Guidelines

As discussed in **Section 2.4.1** TMH7:1989 Part 3, makes provision for the size effect prevalent in concrete shrinkage. The guideline presents an equation to determine the shrinkage deformation at any instant in time, through the use of four partial coefficients as given in **Equation 2-1** (TMH7:1989 Part 3).

$$\Delta_{cs} = k_L \cdot k_c \cdot k_e \cdot k_j \quad \text{Equation 2-1}$$

where:

$\Delta_{cs}$  = shrinkage deformation

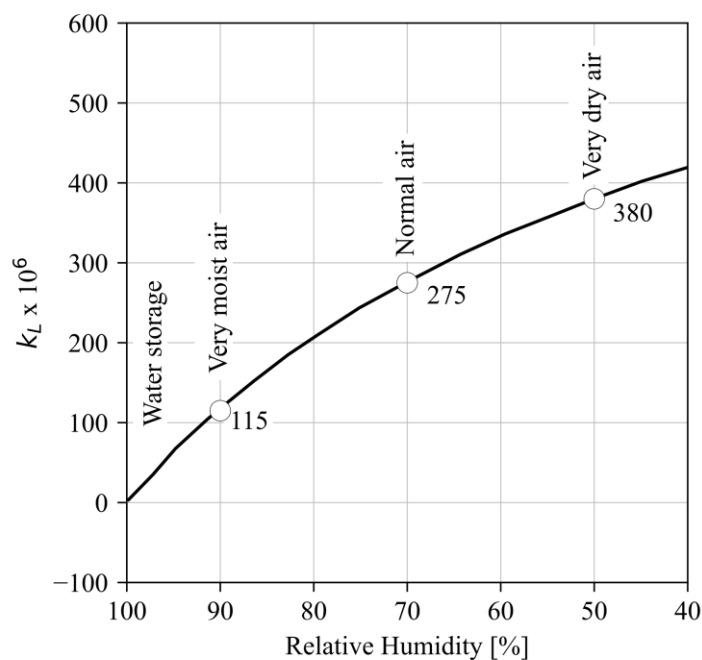
$k_L$  = depends on the environmental conditions

$k_c$  = depends on the composition of the concrete

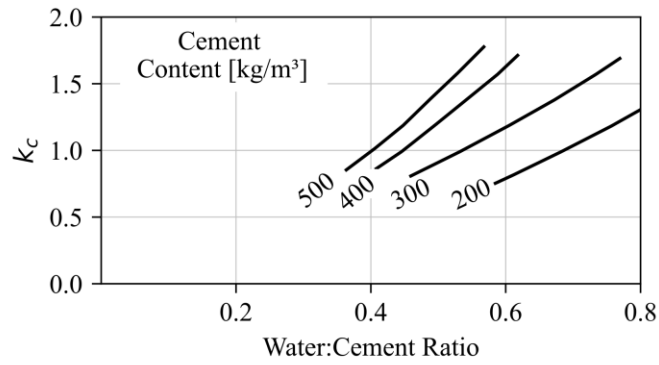
$k_e$  = depends on the effective thickness of the member

$k_j$  = defines the development of shrinkage as a function of time

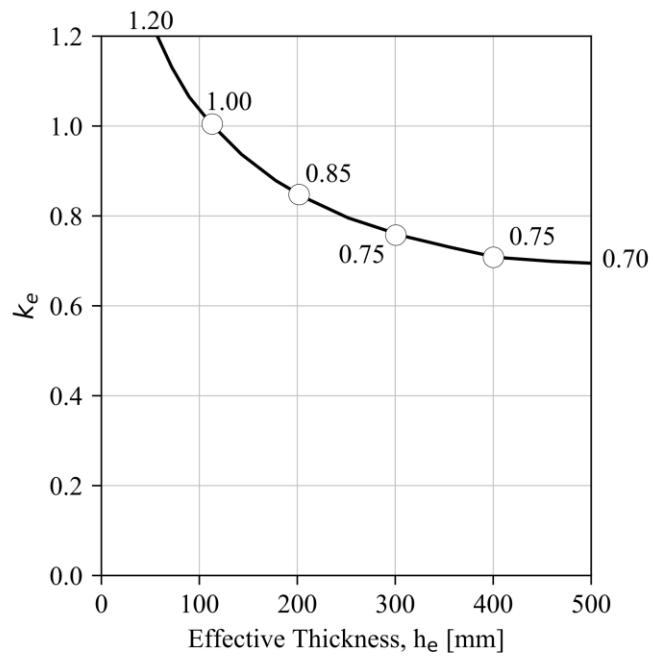
Each partial coefficient has its own graph from which the value can be acquired. For  $k_L$ , the environmental conditions refer to the relative humidity of the air and **Figure 2-9** can be used to determine the coefficient. The composition of the concrete is represented by  $k_c$ , which can be determined according to the water-cement ratio and cement content ( $\text{kg}/\text{m}^3$ ) from **Figure 2-10**.  $k_e$  is determined with the effective thickness ( $h_e$ ) and **Figure 2-11**. The effective thickness is the ratio of the area of the section to the semi-perimeter in contact with the atmosphere. Finally, the coefficient linked to the development of shrinkage over time ( $k_j$ ) is determined using ( $h_e$ ) and time from loading in days with **Figure 2-12**.



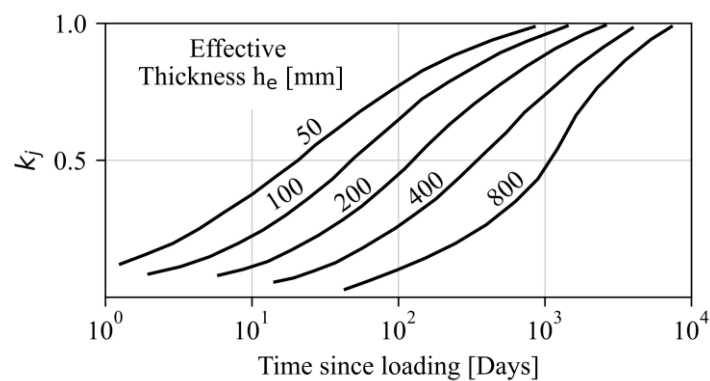
**Figure 2-9** Coefficient for environmental conditions -  $k_L$   
 (Adapted from TMH7:1989)



**Figure 2-10 Coefficient for concrete composition -  $k_c$**   
(Adapted from TMH7:1989)



**Figure 2-11 Coefficient for effective thickness -  $k_e$**   
(Adapted from TMH7:1989)



**Figure 2-12 Variation as a function of time thickness -  $k_j$**   
(Adapted from TMH7:1989)

TMH7:1989 Part 3 is intended for bridge design and is not used for other structures; however it can be used to produce a curve of predicted shrinkage over time, in contrast to SANS 10100-1:2000 which estimates shrinkage for only two time increments: 6 months and 30 years. Both SANS 10100-1:2000 and TMH7:1989 use effective thickness of elements and relative humidity to predict but TMH7:1989 takes additional factors into account. The advantage of both standards is that they were developed for South African conditions but both are based on values over 25 years old.

## 2.5 PREVIOUS FIELD, EXPERIMENTAL AND NUMERICAL WORK

The work completed by various authors relating the response of concrete structures to environmental loading is presented in this section. Emphasis is placed on concrete bridge decks and cross sections. **Table 2-2**, **Table 2-3** and **Table 2-4** present the previous field, experimental and numerical work completed by researchers.

The field work presented relates to full scale bridges which were instrumented and analysed. **Table 2-2** provides a comprehensive overview, encompassing the bridge description, measured parameters, recorded temperature profiles, the presence of shrinkage data, the methodology employed for stress calculations (where applicable), and the incidence of cracks observed on the bridge decks. The instrumentation used in these studies was either embedded within the concrete during the casting process for new structures or applied to the surfaces of pre-existing bridges that were analysed. Notable was that only one study presented shrinkage data (William et al., 2008) and only one other study included temperatures and stresses relating to the heat produced by cement hydration (Chen et al., 2009). Most authors described nonlinear temperature profiles through the vertical depth of the sections but only one reported the temperature profile across the width of the section. The vertical temperature profiles were taken through the centre of solid segments and I-girders but through the web segments of box-girders. In this study, the transverse direction referred to the temperature profile in the top, horizontal segment of box-girders or I-girders. The temperature profile in the transverse direction was also described as nonlinear as the outer extremities were affected differently by the environment. However, even though the extremities displayed different temperatures to the central portions, their temperatures were identical to each other and so the temperature profiles were near symmetrical about the centre vertical axis.

**Table 2-3** lists experimental work reported by authors examining the response of concrete structures to environmental conditions. This research encompasses experiments conducted under laboratory conditions and with exposure to outside environments. Full-scale or prototype models were constructed, instrumented and analysed. Priestly (1972) and Chijiwa et al. (2018) used scale models and noted the practical time-scale, or rate of response, for the concrete models as well as their applicability to full-scale structures. All instrumentation referenced was embedded within the concrete upon casting. The



measured parameters presented temperature profiles and comparisons of experimental data with design codes, models and calculations are included in **Table 2-3**. Some authors proposed new temperature prediction models or design temperature gradients which were all validated either against experimental or field results. Only Chijiwa et al. (2018) used measured strain values to quantify shrinkage and the influence of rain and other weather conditions on the deformation of the structure. Abid et al. (2014) were the only authors to include measured heat of hydration temperatures, but strain was not measured nor theoretically calculated and therefore the associated deformation was not analysed. The dominant focus across the compiled experimental work was solely temperature distributions, as such only two works presented included stress calculations or comparisons (Priestly, 1972; Abid et al., 2021)

The numerical findings from various researchers are summarized **Table 2-4**. Validation of numerical data is an important step in ensuring the reliability and credibility of research and so the program used to build finite element models and the validation of the applicable models for each of the presented works are also included in the table. The temperature distribution profiles were often neglected or only presented for the vertical direction. Furthermore, authors tend to focus on the temperature response based on various input parameters related to temperature but often neglect shrinkage and analysis of stress developed throughout the structures. Moreover, temperature inputs were focused on daily temperature fluctuations and only one author (Han et al., 2023) modelled the temperature and stress relating to heat of hydration.

Based on the reviewed literature it is clear that research works are often only focused on individual parameters such as temperature and shrinkage but do not consider their combined effects on strains or stresses. While it is true that stress levels depend on varying restraint conditions dictated by the structure's type and purpose, stress distributions become particularly crucial, especially in the context of concrete structure response and cracking. As such, more research is required that not only considers various restraint effects but also combinations of environmental loading on cross-section stress profiles. This is especially important considering that environmental loads have the potential to surpass anticipated live loads.

**Table 2-2 Previous Field Work**

| Author                  | Bridge Description  | Measured Parameters (Location)  | Temperature Distribution (Direction) | Shrinkage Included? | Stress calculation (Technique) | Crack occurrence on Deck |
|-------------------------|---|---------------------------------|--------------------------------------|---------------------|--------------------------------|--------------------------|
| William et al. (2008)   | 3-span concrete deck on continuous steel girders                    | Temperature & Strain (Embedded) | Linear (V)                           | Yes                 | Yes (A)                        | Yes                      |
| Chen et al. (2009)      | 3-span continuous prestressed box girder                            | Temperature & Strain (Embedded) | Nonlinear (V)                        | No                  | Yes (NS)                       | No                       |
| Rodriquez (2012)        | Integral 2-span prestressed multicell box girder                    | Temperature & Strain (Surface)  | Nonlinear (V)                        | No                  | Yes (FEA)                      | No                       |
|                         | Integral single span deck on concrete girders                       |                                 |                                      | No                  | Yes (FEA)                      | No                       |
| Peirettie et al. (2014) | Integral 4-span bridge with solid girder and prestressed solid slab | Temperature (Embedded)          | Nonlinear (V)                        | No                  | -                              | No                       |
| Gu et al. (2014)        | 3-span continuous box girder  | Temperature (Embedded)          | Nonlinear (V&T)                      | No                  | Yes (A)                        | Yes                      |

\*V - Vertical direction, T-Transverse direction

\*A - Calculated Analytically, FEA - produced by Finite Element Model and Analysis, NS-not stated

**Table 2-3 Previous Experimental Work**

| Author                        | Structure Shape        | Measured Parameters  | Temperature Distribution (Direction) | Comparisons made to Experimental Results   |
|-------------------------------|------------------------|----------------------|--------------------------------------|--|
| Priestly (1972)               | Single cell box girder | Temperature & Strain | Nonlinear (V)                        | Stress results vs: Analytical theory   |
| Kulprapha & Warnitchai (2012) | T-Section              | Temperature & Strain | Nonlinear (V)                        | Temperature results vs: FEM  |
| Lee (2012)                    | I-Girder segment       | Temperature          | Nonlinear (V&T)                      | Temperature results vs: FEM  |
| Lee et al. (2012)             | I-Girder segment       | Temperature          | Nonlinear (V&T)                      | -  |
| Abid et al. (2014)            | Single cell box girder | Temperature          | Nonlinear (V&T)                      | Temperature Gradients vs: EN1991   |
| Taysi & Abid (2015)           | Single cell box girder | Temperature          | Nonlinear (V&T)                      | Temperature Gradients vs: FEM<br>AASHTO 2012<br>New Zealand Bridge Manual                                |
| Abid et al. (2016)            | Single cell box girder | Temperature          | NS                                   | Temperature Gradients vs: New proposed Predicted temperature model                                       |
| Chijiwa et al. (2018)         | Hollow box section     | Temperature & Strain | NS                                   | Strains: FEM   |
| Hagedorn et al. (2019)        | I-Girder segment       | Temperature          | Nonlinear (V&T)                      | Temperature Gradients vs: Priestly design gradient<br>AASHTO 1989  |
| Abid et al. (2021)            | Single cell box girder | Temperature          | Nonlinear (V&T)                      | -  |
| Feng et al. (2022)            | Three-cell box girder  | Temperature          | Nonlinear (V&T)                      | Temperature Gradients vs: New proposed Predicted temperature model<br>Field results of full-scale bridge |

\*NS - Not stated, FEM - Finite Element Model, V - Vertical direction, T-Transverse direction \*All gauges were embedded in the concrete

**Table 2-4 Previous Numerical Work**

| <b>Author</b>          | <b>Structure Shape</b>              | <b>Temperature Distribution (Direction)</b> | <b>Shrinkage included in model?</b> | <b>Stress considered?</b> | <b>Crack or Crack Potential considered?</b> | <b>Program utilised &amp; model validation</b>  |
|------------------------|-------------------------------------|---|-------------------------------------|---------------------------|---|---|
| Branco & Mendes (1993) | T-section, single box girder & slab | Nonlinear (V)                               | No                                  | No                        | No  | Developed numerical technique, results validated against experimental results of another author                               |
| Wang et al. (2010)     | Single cell box girder              | Nonlinear (V)                               | No                                  | No                        | No  | Unspecified commercial program, results validated against field results of large span bridge                                  |
| El-Tayeb et al. (2017) | Rectangular continuous beams        | NS  | No                                  | Yes                       | Yes   | ABAQUS with three verification examples   |
| Kadlec et al. (2017)   | Double T-section                    | NS  | Yes (B4)                            | Yes                       | No  | Unspecified commercial program, results unvalidated   |
| Abid (2018)            | Three adjacent concrete I-girders   | Nonlinear (V&T)                             | No                                  | No                        | No  | Unspecified commercial program, results validated against experimental results presented by another author and to AASHTO 2012 |
| Han et al. (2023)      | Single cell box girder              | Nonlinear (V&T)                             | No                                  | Yes                       | Yes   | ABAQUS, no verification results presented   |

\*NS - Not stated, V -Vertical direction, T-Transverse direction

## 2.6 SUMMARY

Based on the previous research it is apparent that the predominant focus has been on single or multi-cell box girders. Some authors focused on concrete I-girder sections and others considered steel girders (not included in this study). Furthermore, research did not include the combination of temperature and shrinkage components along with reference to restraint conditions to establish critical tensile stress development. Research centred around the response of different cross-section geometries to environmental loading, is limited to a few numerical and analytical examples based on temperature, but which exclude shrinkage. While temperature distributions through the depths of sections are commonly considered, the transverse direction is neglected as are the stresses produced from daily and seasonal variations, especially considering different restraint conditions. Environmental conditions vary according to geographic location and purpose. Considering research into environmental response of concrete structures which considers South African conditions is scarce, there is a need to compare existing South African technical guidelines with recent experimental results caused by local conditions. In so doing, the potential to utilise existing technical guidelines (intended for bridges) for the improved design of any concrete element exposed to environmental loading can be explored.

The literature reviewed confirms that the temperature and shrinkage response is influenced by the geometric dimensions and cross-section. In the simple comparison between thick and thin elements, thinner elements will reduce the temperature generated by cement hydration, but early shrinkage is more rapid and thermal inertia is lower creating higher sensitivity to temperature change. The beneficial higher thermal inertia of a thicker element may be offset by higher heat of hydration temperatures.

While the literature presented focussed on bridges, the concepts are also applicable to other structures such as beams and slabs. This study presents the comparison of two T-beams (with solid and voided cross-sections respectively) in response to South African environmental loading, with focus on temperature and shrinkage characteristics. Furthermore, the stresses caused by internal equilibrium and restraint conditions for each beam was calculated and related to tensile stresses and crack potential.

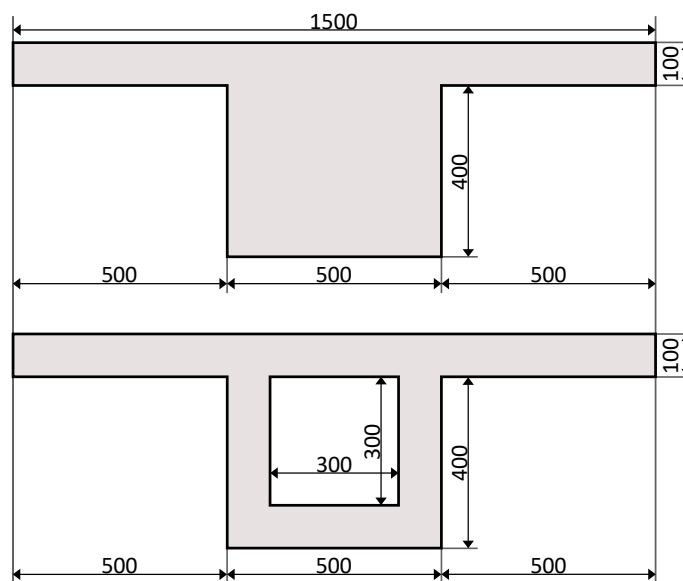
### 3 EXPERIMENTAL SETUP AND WORK

#### 3.1 INTRODUCTION

This chapter presents the methods and experimental setup used in this study to reach the objectives set out in **Chapter 1**. Two concrete T-beams with different cross-sections were cast for this study. Instrumentation was embedded into the T-beams to measure temperature and strain caused by exposure to the outside environment. The experimental setup was completed with the aim of measuring the strains of the statically determinate, free structures such that the induced stresses of fully restrained structures could be calculated and compared. The T-beam configurations are discussed along with the instrumentation position and applicable analytical calculation techniques. Furthermore, the measured and calculated material and cross section properties are presented.

#### 3.2 T-BEAM CONFIGURATION

The cross-sectional dimensions for the T-beams cast and analysed in this study are shown in **Figure 3-1**. The first section was a solid T-beam with a centre depth and width of 0.5 m and 1.5 m respectively. This cross-section will be referred to as the ‘solid’ T-beam, beam, or section. The solid T-beam’s dimensions were chosen to create a half scale model of the spine beams used in the integral bridge presented by Skorpen (2020). In order for the beams to have different thermal inertias whilst maintaining comparability, the second T-beam had identical outer dimensions but with a 0.3 m square void in the centre portion of the beam. The T-beam including the void will be referred to as the ‘voided’ T-beam, beam, or section. The thin sections on either side of the 0.5 m square segment will be referred



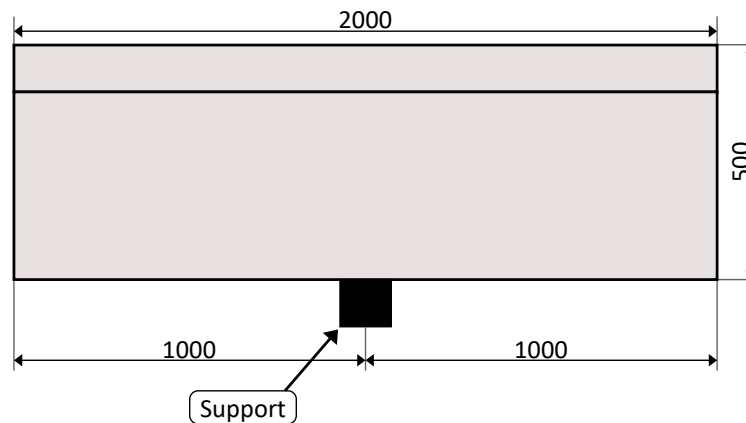
*dimensions in mm*

**Figure 3-1 Cross sectional dimensions of T-beams**

to as flange sections for each beam. The voided beam can be compared to the box-girders evaluated in literature.

The two selected cross-sections were expected to exhibit different thermal and shrinkage behaviours despite the identical external dimensions. The solid T-beam had a larger thermal inertia due its larger cross-sectional area per width compared to the voided T-beam. The flange sections of both beams were 100 mm thick, but the voided section had uniform thickness throughout while the solid section had a much greater thickness in the central solid portion. The different thicknesses affect moisture diffusion paths as well as heat retention and diffusion, influencing both thermal and shrinkage strain development. As such it was expected that the voided section would be more sensitive to temperature change, but also develop lower heat of hydration temperature and exhibit uniform shrinkage.

Since strains can only be measured when the structure is free to move, the intension was to cast the beams in such a manner that they were unrestrained by external support as far as possible. If the unrestrained strains can be measured, the restrained stresses can be calculated. Therefore, a cantilever setup was chosen. To ensure self-weight and creep strains were small enough to be considered negligible, the spans were kept small. The cantilever arrangement can be seen in **Figure 3-2**.



*dimensions in mm*

**Figure 3-2 Elevation view of cantilever arrangement**

In most scenarios beams or bridge sections are not open to the environment on either end. Therefore, moisture exchange and temperature interactions with the environment would only occur through the surfaces open to the environment. To emulate these conditions, the end surfaces of both beams were coated with a sealant to lessen the moisture loss or gain. For the voided section, the opening was closed off with 50 mm thick polystyrene to minimize the temperature change within the void caused by outside temperature – as would be the case in a continuous bridge deck or tied-in beam.

### 3.2.1 Mould Construction

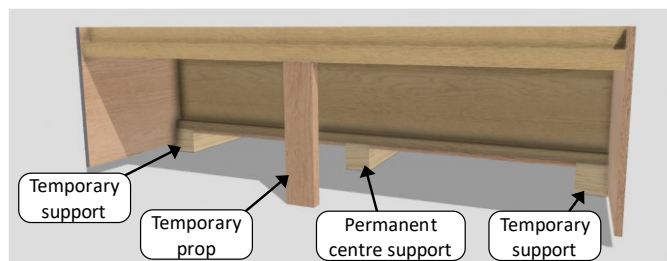
To achieve the cantilever configuration described, moulds needed to be constructed in a way that allowed the props and shutterboards to be removed, without lifting or moving the beams. Such actions would cause unwanted strains on the early age concrete. Three-dimensional renderings of the moulds built for the solid and voided beams are shown in **Figure 3-3** and **Figure 3-4** respectively. The moulds were constructed in an identical manner apart from the void former included for the voided beam. The void former was created by assembling shutterboards in a square shape and securing it to the end shutterboards on either side with brandering. To ensure the void former would not deform from the concrete weight on top, or uplift from the bottom, bracing was added to the inside of the void former to increase its rigidity. Because the beams were to cantilever from the centre outwards, the beams needed to be raised from the ground. Therefore, ground supports were added at each end and in the middle of each mould. The middle support remained in position to become the permanent centre support, while the supports at either end were removed once the shutters had been stripped. Temporary props were added to the centre of the flange sections to avoid excessive deflections, and these were also removed once the shutters had been stripped. The different supports and props are displayed in **Figure 3-5**. The moulds were constructed using film faced shutterboards and varnished wood to ensure minimal moisture absorption from the concrete by the moulds. **Figure 3-6** shows the completed solid T-beam mould and **Figure 3-7** shows the mould with the reinforcement cage detailed in **Section 3.2.2**, positioned inside the mould before casting.



**Figure 3-3 Solid T-beam mould 3D rendering**



**Figure 3-4 Voided T-beam mould 3D rendering**



**Figure 3-5 Mould support layout**





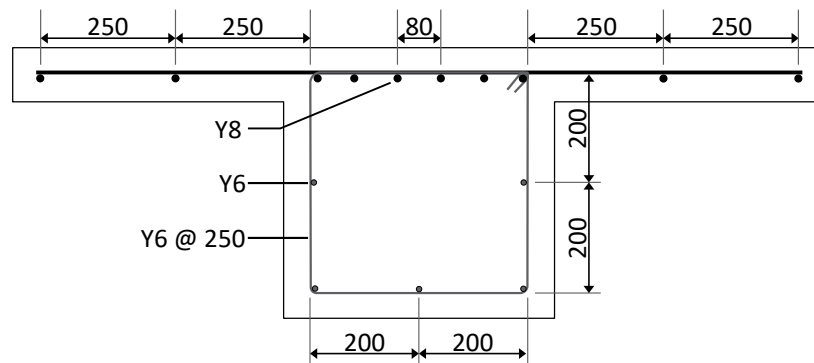
Figure 3-6 Completed solid T-beam mould



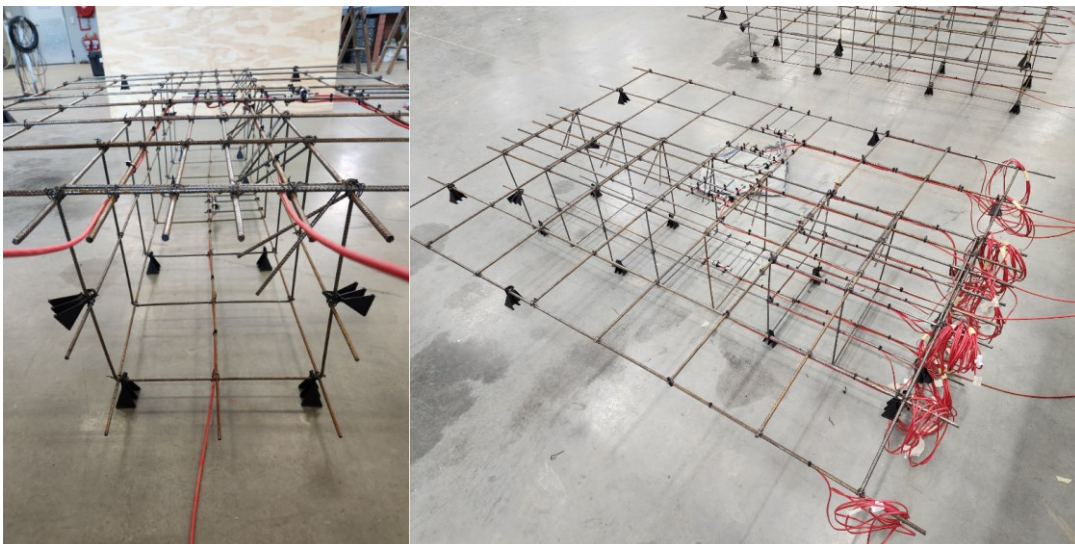
Figure 3-7 Solid T-beam mould with reinforcement cage

### 3.2.2 Reinforcement

The T-beams would be exposed to exclusively environmental loads and because the T-beams cantilevered from the centre to either side, the reinforcement was calculated for a hogging bending moment. The required reinforcement was calculated according to Eurocode 2 for the self-weight of the solid T-beam, but minimum reinforcement governed the reinforcement requirements. The reinforcement layout is shown in **Figure 3-8** and was used for both the solid and voided sections. Y8 bars were used for the main longitudinal and transverse reinforcement while Y6 bars were used for the stirrups and distribution steel. A top cover of 50 mm was used and stirrups and traverse reinforcement bars were spaced at 250 mm centres. The minimal reinforcement allows the concrete response to environmental loading measured without substantial influence from the reinforcement. **Figure 3-9** shows photos of the reinforcement cages and cover blocks, with the instrumentation gauges and cables described in **Section 3.3**, fastened to the reinforcement with zip ties.



**Figure 3-8 Reinforcement layout**

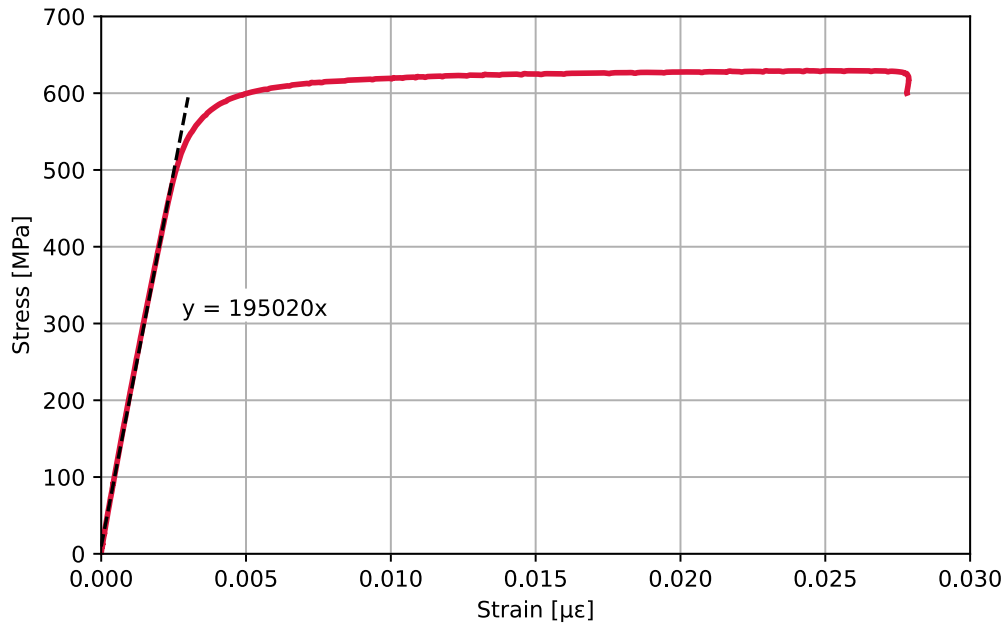


**Figure 3-9 Reinforcement cages**

In the transformed section calculation, only the main Y8 bars were taken into account. Multiple tensile tests were conducted on Y8 bars from the same manufacturing batch as used to build the reinforcement

cages used in this study. The stress-strain relationship was used to determine an average modulus of elasticity for the steel as 195 GPa.

**Figure 3-10** shows the stress-strain relationship until failure of one of the tensile tests conducted. The gradient of the trend line through the linear portion of the graph indicates the modulus of elasticity of the tested bar in megapascals.



**Figure 3-10 Reinforcement stress versus strain relationship**

### 3.3 INSTRUMENTATION

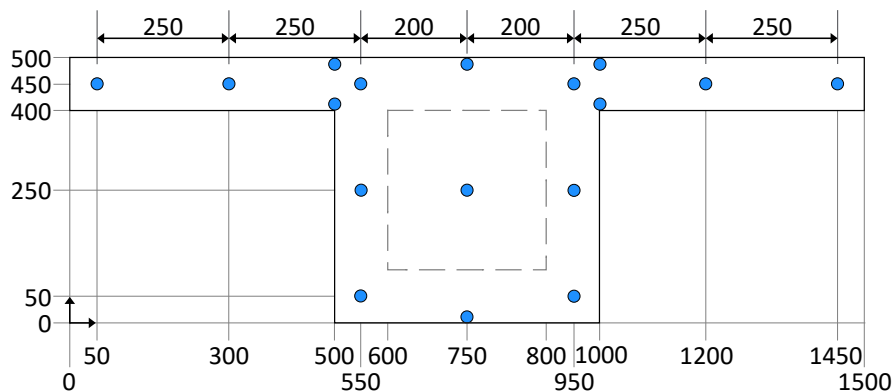
#### 3.3.1 Introduction

Temperatures and strains in the beams were measured by means of thermocouples and vibrating wire strain gauges (VWSGs) respectively. The thermocouples were logged by Graphtec GL820 midi loggers and the VWSGs by a Campbell Scientific CR6 data logger. Both loggers captured data at 15 min intervals for the duration of the study.

The thermocouple temperatures were calibrated against the VWSG thermistors to ensure the compatibility between the measurements obtained from the different instruments. This facilitated their concurrent use for the same calculations. Furthermore, the theoretical strains calculated from the temperatures recorded by the thermocouples were validated by comparison to the measured strains captured by the VWSGs. In this way, the theoretical stresses calculated from measured temperature were calibrated and could be used in further calculations. This calibration process ensured the accuracy of the temperature-based theoretical stress calculations, making them suitable for subsequent calculations.

### 3.3.2 Thermocouples

To capture the temperature distribution throughout the T-beams, thermocouples were positioned as shown in **Figure 3-11**. The thermocouple wires were fastened to the reinforcement to keep them in the correct positions. The placement of the thermocouples was identical for the solid and voided beams; the only difference in temperature measurement was for the centre point position (750, 250) in **Figure 3-11**. In the solid beam it measured the concrete temperature and in the voided beam it measured the air temperature of the void.



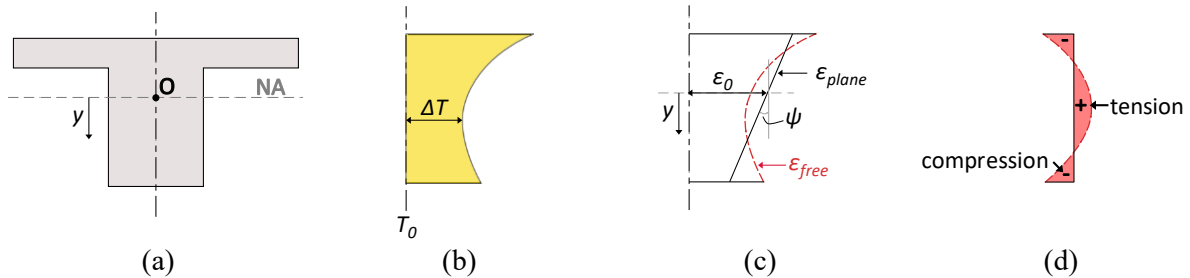
**Figure 3-11 Thermocouple positions**

Temperature variations cause strains within the concrete which are proportional to the material's coefficient of thermal expansion, but the stress distribution is mainly dependent on the restraint conditions imposed on the structure. For the stresses calculated in this study it is assumed the structure is fully restrained, as such axial movements and curvature are prevented. These restraint conditions emulate continuous, tied-in or monolithically cast beams. With these boundary conditions bending, or curvature, stresses and axial effective stresses develop as described in **Table 2-1** for structure (e). There is an additional stress which develops for non-linear temperature distributions regardless of boundary condition, which is referred to as self-equilibrating stress. This stress develops as result of the incompatibility between the nonlinear hypothetical free strain caused by a temperature change and the plane strain which must be linear, as per Euler-Bernoulli beam theory.

The thermocouple temperatures were used to calculate the strains and associated stresses within the beams because of temperature fluctuations of the environment. These stresses were calculated theoretically with the following assumptions:

- Plane sections remain plane during bending (Euler-Bernoulli beam theory holds).
- The beams remain uncracked and therefore effective stiffness remains constant.
- Material properties are considered to be independent of temperature.
- Thermal stress can be considered independent of stress and strain from other loading (Principle of superposition is applicable).

The self-equilibrating stress calculation procedure is explained for a cross section with an arbitrary nonlinear temperature rise and with the methodology described by Priestley (1978), Ghali & Favre (1986) and Elbadry & Ghali (1986). The datum for the temperature change is represented by  $T_0$ . The datum is typically the temperature at a time where the temperature variation through the cross section is minimal. **Figure 3-12** illustrates how the self-equilibrating stresses were calculated.



**Figure 3-12 (a) Section, (b) Vertical nonlinear temperature distribution, (c) strain profile, (d) self-equilibrating stress**

For the cross-section in **Figure 3-12(a)** the environmental temperature change induces a non-linear temperature rise, as shown in **Figure 3-12(b)**, through the depth of the section. If each fibre in the beam was not restrained by the adjacent fibres and was free to expand, the hypothetical free strain would be of the same shape as the temperature distribution in **Figure 3-12(b)**. The hypothetical free strain ( $\epsilon_{free}$ ) is indicated by the dashed line in **Figure 3-12(c)** and can be calculated at any coordinate using **Equation 3-1**.

$$\epsilon_{free} = \alpha_c \cdot \Delta T_{(y)}$$

**Equation 3-1**

where:

$\epsilon_{free}$  = hypothetical free strain

$\alpha_c$  = coefficient of thermal expansion of concrete

$\Delta T_{(y)}$  = change in temperature from datum at point y

If the strain is artificially prevented the artificial stress required is given in **Equation 3-2**:

$$\sigma_{restraint} = -E \cdot \alpha_c \cdot \Delta T_{(y)}$$

**Equation 3-2**

where:

$\sigma_{restraint}$  = theoretical stress from artificial restraint

$E$  = modulus of elasticity of the material (assumed to be constant)

$\alpha_c$  = coefficient of thermal expansion of concrete

$\Delta T_{(y)}$  = change in temperature from datum at point y

The resultant artificial stress may be presented by an axial force ( $\Delta N$ ) and bending moment ( $\Delta M$ ) given in **Equation 3-3** and **Equation 3-4** respectively.

$$\Delta N = \int \sigma_{restraint} dA \quad \text{Equation 3-3}$$

$$\Delta M = \int \sigma_{restraint} y dA \quad \text{Equation 3-4}$$

The resulting axial strain at the centroid and curvature are given by **Equation 3-5** and **Equation 3-6**.

$$\varepsilon_0 = -\frac{\Delta N}{EA} \quad \text{Equation 3-5}$$

$$\psi = -\frac{\Delta M}{EI} \quad \text{Equation 3-6}$$

where:

$\varepsilon_0$  = axial strain

$\psi$  = curvature

$A$  = area of the cross section

$I$  = second moment of area about the axis through the centroid

With the assumption that plane cross sections tend to remain plane and therefore produce linear strain profiles, the resulting plane strain ( $\varepsilon_{plane}$ ) at any fibre is given by **Equation 3-7**.

$$\varepsilon_{plane} = \varepsilon_0 + \psi(y) \quad \text{Equation 3-7}$$

The resulting stress from difference between the plane strain and the hypothetical free strain is called the self-equilibrating stress ( $\sigma_{self-eq}$ ) given by **Equation 3-8**.

$$\sigma_{self-eq} = E \cdot (-\varepsilon_{free} + \varepsilon_0 + \psi(y)) \quad \text{Equation 3-8}$$

The self-equilibrating stress distribution is shown in **Figure 3-12(d)** and the sign convention for this study was as follows: positive stress indicates tension and negative stress indicates compression relative to the planar stress produced by the plane strain.

For the boundary conditions described, bending and axial stresses will occur in addition to the self-equilibrating stress explained before. Longitudinal axial movement is governed by the effective temperature ( $T_{eff}$ ) of a cross section given in **Equation 3-9** (Emerson, 1976).

$$T_{eff} = \frac{\sum A_i \cdot T_i}{\sum A_i} \quad \text{Equation 3-9}$$

where:

$T_{eff}$  = effective cross section temperature

$A_i$  = area of the  $i^{\text{th}}$  segment of the section

$T_i$  = temperature of the  $i^{\text{th}}$  segment of the section

$T_{eff}$  is the weighted average temperature of the cross section. Any change in  $T_{eff}$  would result in axial strain distributed evenly across the section. Therefore, a uniform axial stress would occur if this axial strain were prevented.

Upon inspection of **Equation 3-3**, the change in temperature defined to calculate the axial force  $\Delta N$  applied at the sections centroid, is equivalent to the change in effective temperature (**Equation 3-10**).

$$\frac{\int \Delta T dA}{\int dA} = \frac{\Sigma A_i \cdot \Delta T_i}{\Sigma A_i} = \Delta T_{eff} \quad \text{Equation 3-10}$$

Therefore, the axial stress associated with temperature is a direct result of the change in  $T_{eff}$  and will consequently be referred to as effective temperature stress ( $\sigma_{T_{eff}}$ ) in this study (**Equation 3-11**).

$$\sigma_{T_{eff}} = -E \cdot \alpha_c \cdot \Delta T_{eff} \quad \text{Equation 3-11}$$

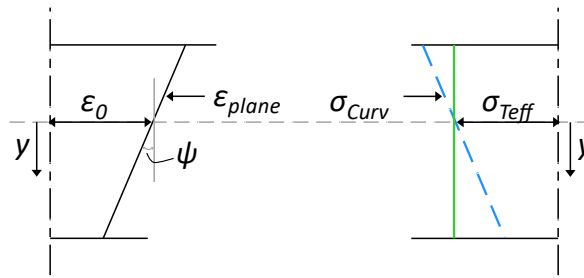
As tensile stresses are taken as positive, a reduction in  $T_{eff}$  relative to the datum  $T_0$ , would produce a positive stress in the section, as shortening of the beam would be prevented. Since any change in temperature is relative to the datum  $T_0$ , the time (and therefore temperature) at which the element is considered to be restrained has a large influence on the axial stress induced.

If curvature ( $\psi$ ) as shown in **Figure 3-12(c)** is prevented, curvature stresses ( $\sigma_{Curv}$ ) develop and can be calculated through **Equation 3-12**.

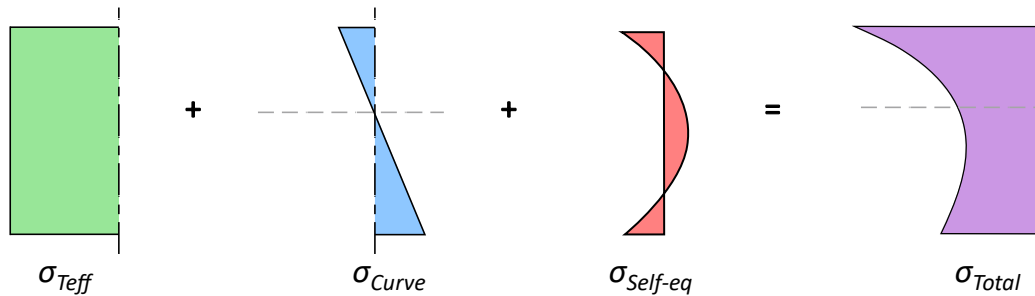
$$\sigma_{Curv} = \frac{M \cdot y}{I} = E \cdot \psi \cdot y \quad \text{Equation 3-12}$$

The calculated curvature stresses are not directly applicable to a specific span configuration or position but rather act as a basis for comparison between the two cross sections. For the comparison of stresses to the tensile capacity of the concrete to identify possible cracking, the stresses would be more applicable to the interior spans in multi-span structures.

**Figure 3-13** illustrates how the effective ( $\sigma_{T_{eff}}$ ) and curvature stresses ( $\sigma_{Curv}$ ) can be calculated from the strain profile of the cross section for an arbitrary temperature rise. **Figure 3-14** shows how the individual stress components are added to produce the total stress profile ( $\sigma_{Total}$ ) caused by a nonlinear temperature distribution in a fully restrained structure. In the case where axial movement is permitted but curvature is restrained, the total stress would simply be the sum of the curvature and self-equilibrating stresses.



**Figure 3-13 Strain profile with effective and continuity stresses**



**Figure 3-14 Components of total thermal stress**

The above explanation referred specifically to the vertical temperature distribution, strains and related stresses. In this study, the transverse direction refers to the measured temperatures and by extension strains and stress in the centre of the top 100 mm of each T-beam, that is, at the position 450 mm above the soffit. Self-equilibrating stress in the transverse direction is mostly neglected through literature but for the purposes of this study, calculated theoretical strains are equal across the width of the section because plane sections tend to remain plane. Therefore, the self-equilibrating stress in the transverse direction was calculated as the difference between the hypothetical free strain and the strain calculated at a height of 450 mm.

### 3.3.3 Vibrating Wire Strain Gauges

The VWSGs have embedded thermistors so that the strain readings can be temperature compensated, but this also conveniently provides additional temperature readings at the positions of the VWSGs. The strain readings need to be temperature compensated because the gauge itself has a different coefficient of thermal expansion than the concrete it is imbedded into. A VWSG measures frequency which is converted into strain by means of a gauge calibration factor. This initial strain needs to be temperature compensated for the gauge's coefficient of thermal expansion. Therefore, the total strain ( $\epsilon_{total}$ ) measured in the concrete at any point in time can be calculated with **Equation 3-13** (RST Instruments LTD., 2019).



$$\varepsilon_{total} = (R_{n+1}^2 - R_n^2) \cdot CF + (T_{n+1} - T_n) \cdot \alpha_{gauge} \quad \text{Equation 3-13}$$

where:

$\varepsilon_{total}$  = total strain ( $\mu\varepsilon$ )

$R_n$  = initial frequency reading ( $\text{Hz} \times 10^{-3}$ )

$R_{n+1}$  = subsequent frequency reading ( $\text{Hz} \times 10^{-3}$ )

$CF$  = gauge calibration factor (given by manufacturer: 3.476)

$T_n$  = initial temperature reading ( $^{\circ}\text{C}$ )

$T_{n+1}$  = subsequent temperature reading ( $^{\circ}\text{C}$ )

$\alpha_{gauge}$  = coefficient of thermal expansion of the gauge:  $12.2 \mu\varepsilon/^{\circ}\text{C}$

The total strain calculated using **Equation 3-13** includes thermal strain ( $\varepsilon_t$ ) caused by temperature changes within the concrete. Therefore, to calculate the strain independent of temperature ( $\varepsilon_m$ ) the thermal strain must be removed from the total strain with **Equation 3-14** (RST Instruments LTD., 2019). The strain values which are independent of temperature are required to calculate the effects of shrinkage or deformation strains.

$$\varepsilon_m = (R_{n+1}^2 - R_n^2) \cdot CF + (T_{n+1} - T_n) \cdot (\alpha_{gauge} - \alpha_c) \quad \text{Equation 3-14}$$

where:

$\varepsilon_m$  = mechanical strain ( $\mu\varepsilon$ )

$R_n$  = initial frequency reading ( $\text{Hz} \times 10^{-3}$ )

$R_{n+1}$  = subsequent frequency reading ( $\text{Hz} \times 10^{-3}$ )

$CF$  = gauge calibration factor (given by manufacturer: 3.476)

$T_n$  = initial temperature reading ( $^{\circ}\text{C}$ )

$T_{n+1}$  = subsequent temperature reading ( $^{\circ}\text{C}$ )

$\alpha_{gauge}$  = coefficient of thermal expansion of the gauge:  $12.2 \mu\varepsilon/^{\circ}\text{C}$

$\alpha_c$  = coefficient of thermal expansion of concrete ( $\mu\varepsilon/^{\circ}\text{C}$ )

The positions of the VWSG within the cross sections and in plan are shown in **Figure 3-15**. **Figure 3-16** shows the portion of the reinforcement cage in the voided T-beam mould to which the VWSGs were attached. The gauges labelled 1 to 4 were orientated to measure strain in the longitudinal direction, while gauges 5 and 6 were orientated orthogonally. The sign convention for the VWSGs is as follows: negative strain values indicate a shortening of the gauge caused by concrete contraction, while positive strains indicate elongation of the gauge and concrete. Therefore, negative measured strains in the free beams represent the development of tensile stresses for restrained conditions.

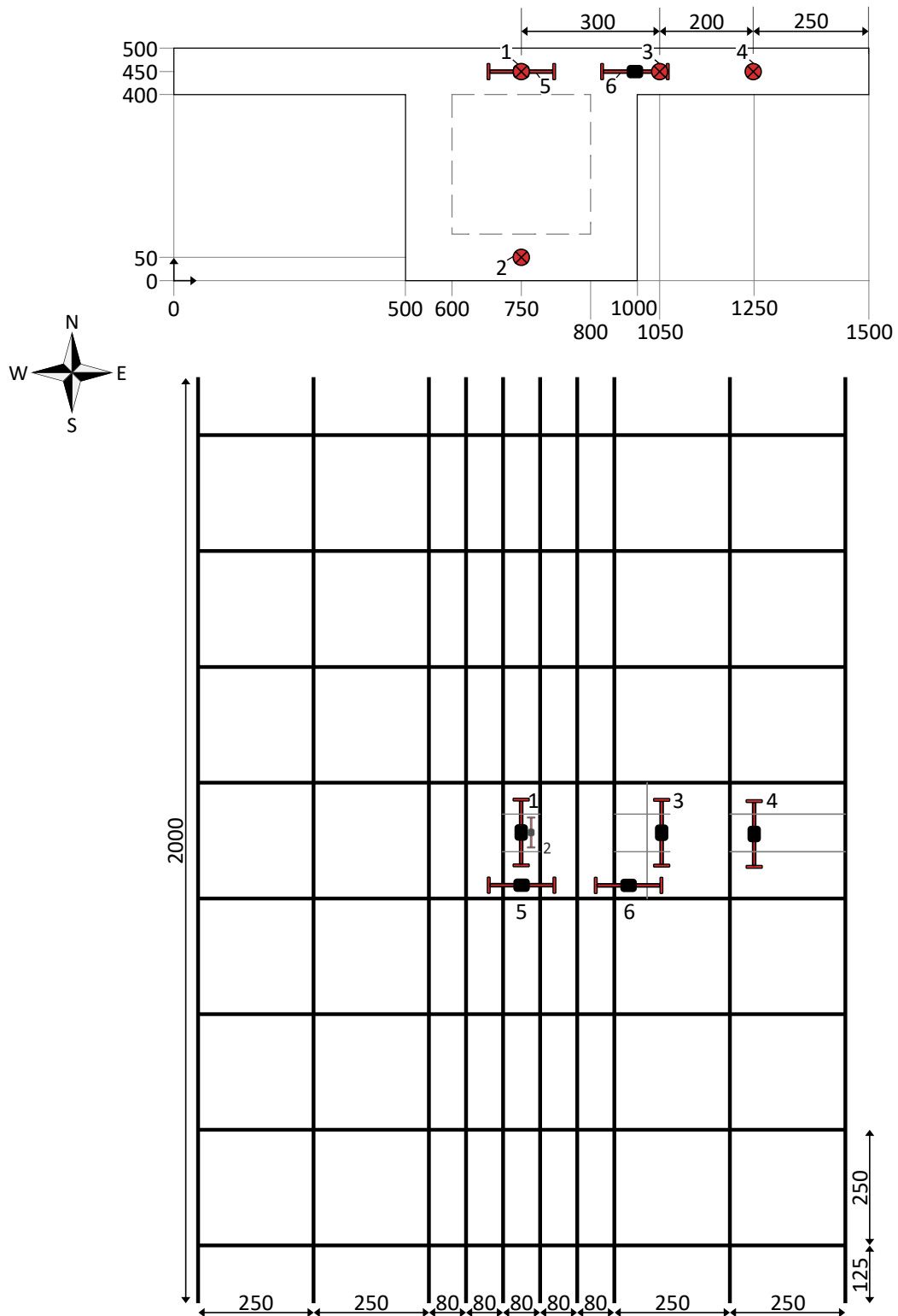
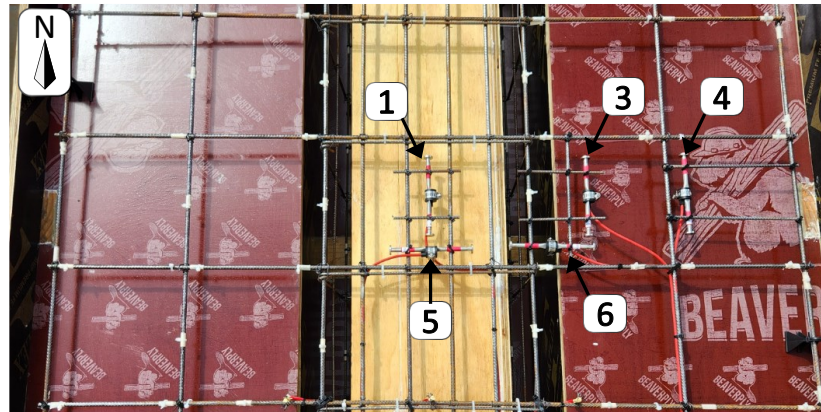


Figure 3-15 VWSG positions



**Figure 3-16 Plan view of VWSGs fixed to steel in voided T-beam mould**

### 3.3.4 Weather Station and Ambient Temperature

In addition to the sensors cast into the concrete, the data from the weather station positioned on the roof of Engineering 4.0 was also captured. The weather station was installed in late 2020, therefore the historical outside temperature data for 2021, 2022 and portion of 2023 included in this study, were available. The precipitation data for the time period of the study was also collected from the weather station.

As a result of the configuration used to complete casting, the final beams were only elevated from the ground slab by approximately 100 mm. Therefore, the temperature in the vicinity of the beams would differ from the temperature recorded by the weather station at any point in time. As such, there was an additional thermocouple placed in the shade underneath the void T-beam that gave an indication of the ambient temperature surrounding the beams. The minimum temperatures recorded by the thermocouple were higher than the weather station minimum temperatures. This difference can be attributed to the thermal inertia of the concrete of the beams themselves as well as the adjacent building and ground slab the beams were cast on (described in **Section 3.4**). Due to the high thermal inertia of concrete, the heat energy stored in the concrete during the day is slowly released in the evening. Consequently, the temperature surrounding the concrete surfaces remain relatively warm during the evenings; accounting for the higher temperature recorded by the thermocouple placed close to the beams. When compared to the maximum outside temperature recorded by the weather station, the maximum daily temperature of the thermocouple was greater even though the thermocouple was placed in the shade of the beam and not in direct sunlight. A similar explanation to the minimum temperatures exists, as the thermocouple was placed close to various concrete surfaces which absorb and deflect heat resulting in higher maximum temperatures.

### 3.4 CONCRETE CASTING

The T-beams were cast and remained outside Engineering 4.0 - the Civil Engineering Laboratory of the University of Pretoria, situated in Hillcrest, Pretoria, South Africa. The beams were cast on an existing ground slab, strategically placed adjacent to one of the building's exterior walls. This location was chosen to provide convenient access to power for instrumentation while ensuring that the cables remained as protected as possible from potential interference. The chosen position allowed the beams to be exposed to direct sunlight and/or rain throughout the day.

#### 3.4.1 Mix Design

Due to the scale of the T-beams, a concrete mixer truck was required to provide a large enough volume of concrete to cast the beams and material property samples in a single cast. A standard flowable, durability concrete mix (typical for bridge construction in South Africa) was ordered. The mix design proportions are given in **Table 3-1**. The water-cement ratio was 0.66 and the target characteristic compressive strength was 40 MPa. The concrete slump was measured as 140 mm.

**Table 3-1 Concrete Mix Proportions**

| Material                       | Proportion | Unit [m <sup>3</sup> ] |
|--------------------------------|------------|------------------------|
| AfriSam High Strength Cement   | 273.0      | kg                     |
| Fly Ash                        | 77.0       | kg                     |
| Ferro quartzite stone          | 960.0      | kg                     |
| Ferro quartzite sand           | 707.0      | kg                     |
| Washed filler                  | 318.4      | kg                     |
| Chryso-Optima Superplasticiser | 2.1        | ℓ                      |
| Water                          | 180.2      | ℓ                      |

#### 3.4.2 Casting and Curing Conditions

Casting of the T-beams commenced at 14:50 on the 3<sup>rd</sup> of April 2023 and was completed by 15:50 on the same day. Throughout the casting process, particular care was taken to ensure sufficient compaction through the use of a poker vibrator. The vibration along with the concrete workability allowed the concrete to flow easily beneath the void of the voided T-beam. **Figure 3-17** shows the moulds and concrete mixer truck before and during casting and **Figure 3-18** shows the surface finishing of one of the beams before the T-beams and cast specimens were covered with curing blankets. The specimens were required to determine representative concrete material properties and were therefore exposed to the same environment as the T-beams. All the cast elements were kept covered until the blankets were removed 24 hours after casting was completed. **Figure 3-19** shows the elements covered by the curing blankets the morning of the 4<sup>th</sup> of April 2023. It should be noted that in practise, the bottom segment of the voided beam would be often cast before the top due to formwork practicality. Similarly, the rectangular segment of the solid T-beam could be cast before the top, or deck slab, is cast on top. This would induce marginal temperature and shrinkage differences between the segments because of the

slight difference in concrete age. The casting process used in this study provides conditions for simultaneous commencement of temperature and shrinkage development because all segments of the T-beams were cast concurrently. Nonetheless, the results presented in this study are considered applicable because it provided ideal conditions for both temperature and shrinkage between different segments within the beams. The stresses which developed between segments of the same element cast simultaneously would be lower than when segments are cast separately.



**Figure 3-17** Moulds and concrete mixer truck before and during casting



**Figure 3-18** Concrete surface floating



**Figure 3-19** Curing blankets placed over beams

**Figure 3-20** displays the solid and voided T-beams after the shutters were stripped and the temporary props and supports were removed. The cables for the instrumentation were threaded through holes drilled into the end shutter closest to the building. When the other shutters were removed, the end shutter was pulled away from the concrete surface and placed on bricks for support. This allowed the cables to remain in place and undamaged while the concrete surface was exposed to the atmosphere. **Figure 3-21** shows the final cantilever position of the T-beams.



**Figure 3-20 Completed T-beams**



**Figure 3-21 T-beams in cantilever configuration**

## 3.5 CONCRETE MATERIAL PROPERTIES

### 3.5.1 Setting Time

The final setting time of concrete is important to consider as it marks the point where concrete loses its plasticity and becomes rigid. From this point onward the solid material develops strain and associated stresses. The setting time of the concrete was determined by adopting the “Derivatives” method described by Ge et al. (2009) and supported by Kang et al. (2020). The method defines the peak of the first derivative of the heat of hydration as final set. **Figure 3-22** displays the VWSGs considered for the determination of setting time. **Figure 3-23** shows the change in temperature recorded by VWSGs for the time from shortly after casting was completed, to the next morning. Gauges 1 to 4 are as labelled in **Figure 3-15**, where the ‘S’ and ‘V’ notation refers to the solid and void sections respectively. The first derivative of change in temperature with respect to time is shown in **Figure 3-24**. The peak of rate of change of temperature occurred at 21:15 and this was taken as the final setting time.

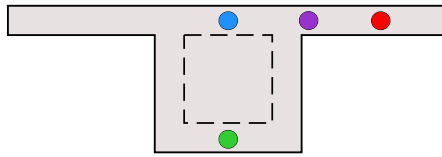


Figure 3-22 VWSG position for setting time determination

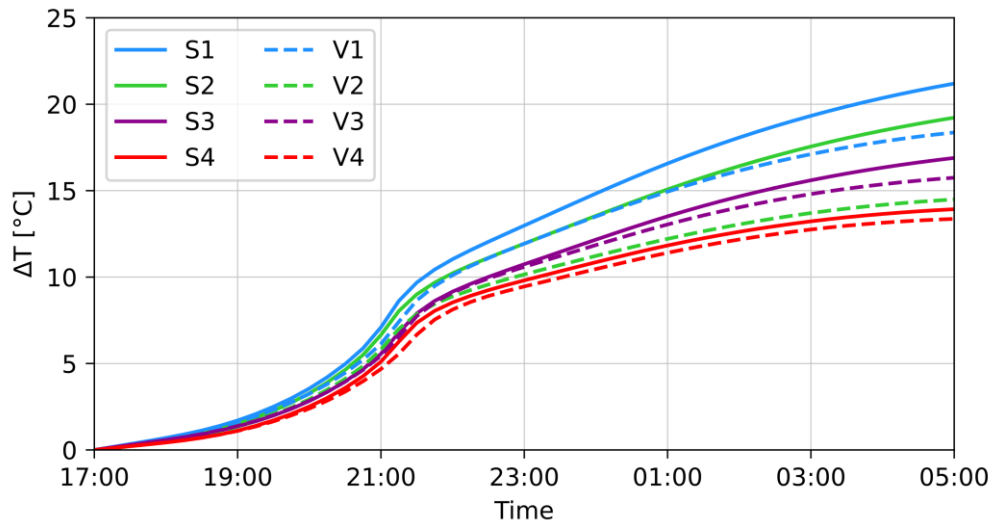


Figure 3-23 Change in temperature due to heat of hydration

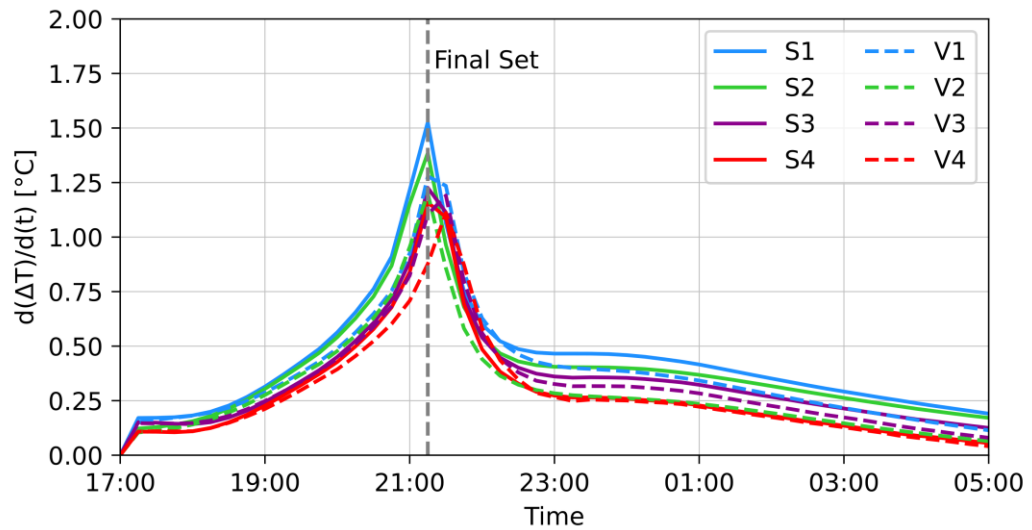


Figure 3-24 Derivative of hydration with time

### 3.5.2 Coefficient of Thermal Expansion

Alexander (2021) defines the coefficient of thermal expansion (CTE) as an indication of the magnitude of strain that develops in a material in response to a unit change in temperature. For a linear CTE the thermal strain is given by **Equation 3-15**:

$$\varepsilon_t = \frac{\Delta l}{l_0} = \alpha \cdot \Delta T \quad \text{Equation 3-15}$$

where:

$\varepsilon_t$  = thermal strain

$\Delta l$  = change in length of element with original length  $l_0$  due to a change in temperature

$l_0$  = original element length

$\Delta T$  = change in temperature

$\alpha$  = coefficient of thermal expansion of the material

The different components of concrete each have unique CTEs, which makes the CTE of concrete quite complex. The CTE of concrete will lie somewhere between that of the natural aggregate used and the hydrated cement paste. Alexander (2021) states that the CTE of concrete is a complex combination of hygral swelling and thermal dilation of the solid components of the material. After final set the CTE of concrete varies due to variations in its moisture content caused by the surrounding environment (Downie, 2005; Mateos et al., 2019). However, for the thermal strain calculations presented in this study, the CTE was to be considered constant. The CTE for the concrete used in this study was determined by using the same method as presented by Kada et al. (2002), which uses the strain and temperature readings recorded by a vibrating wire extensometer to determine the CTE soon after set. The readings from a VWSG placed in the centre of a 0.125 m<sup>3</sup> unreinforced cube, cast alongside the T-beams were used in this study (**Figure 3-25**). The CTE was calculated according to **Equation 3-16** as 11.9  $\mu\text{ε}/^\circ\text{C}$ .



**Figure 3-25 VWSG in unreinforced 0.5 m cube for CTE**



$$\alpha_c = \frac{\varepsilon_t}{\Delta T}$$

**Equation 3-16**

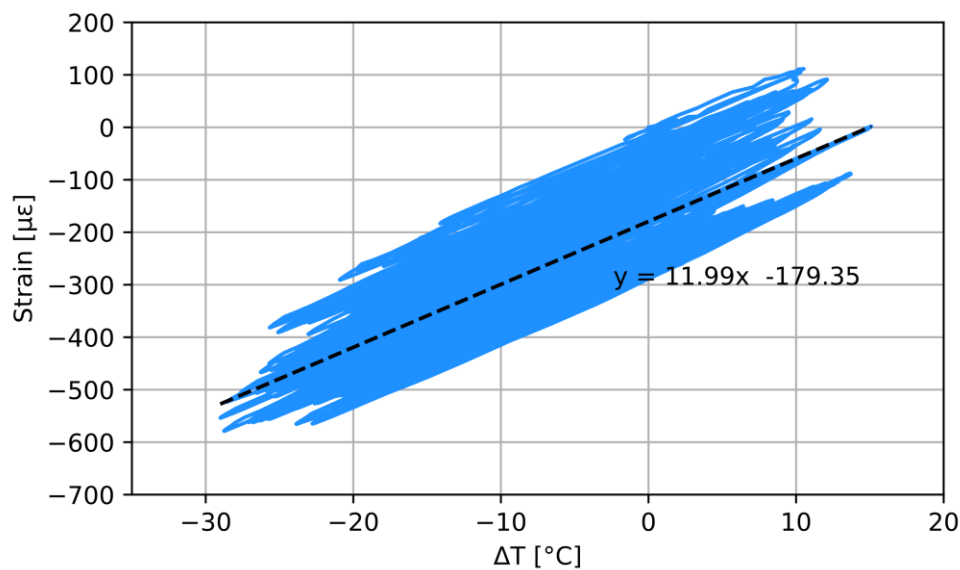
where:

$\alpha_c$  = CTE of concrete ( $\mu\varepsilon/^\circ\text{C}$ )

$\varepsilon_t$  = thermal strain ( $\mu\varepsilon$ )

$\Delta T$  = change in temperature ( $^\circ\text{C}$ )

Even though  $\alpha_c$  varies over time, the assumed value of  $11.9 \mu\varepsilon/^\circ\text{C}$  remains a good estimate. This can be seen by the correlation of the average slope plotted in **Figure 3-26** for the time period considered in this study, to the assumed  $\alpha_c$  value.



**Figure 3-26 Strain versus  $\Delta T$  for the duration of the study**

### 3.5.3 Compressive Strength

Twenty-one 100 mm cube specimens were cast with the T-beams so that the compressive strength could be tested on various dates according to SANS 5863:2006. The specimens were cast according to SANS 5861-3:2006. To determine the characteristic compressive strength of the concrete over time, six samples were placed in a water bath of between  $22^\circ\text{C}$  and  $25^\circ\text{C}$  after demoulding according to SANS 5861 3:2006. A deviation from the standard curing was made for the remaining specimens, as they were placed outside alongside the T-beams. This was done so that these samples could experience the same conditions as the beams and thereby give a representative value of the compressive strength of the beams over time. It is important to note the difference in strengths for the two curing methods, since testing the samples which experience the same conditions as the beams gives a more representative values, but designs are completed according to characteristic strengths. The tested strengths for both curing methods are shown in **Figure 3-27**. The 28-day characteristic strength of the concrete was  $41.5 \text{ MPa}$  and the 28-day strength of the samples left outside was  $37.8 \text{ MPa}$ . Over time the strengths

from both curing methods continued to increase up to 164 days; this continued strength increase can be attributed to the inclusion of fly ash in the mix design and its associated pozzolanic reaction.

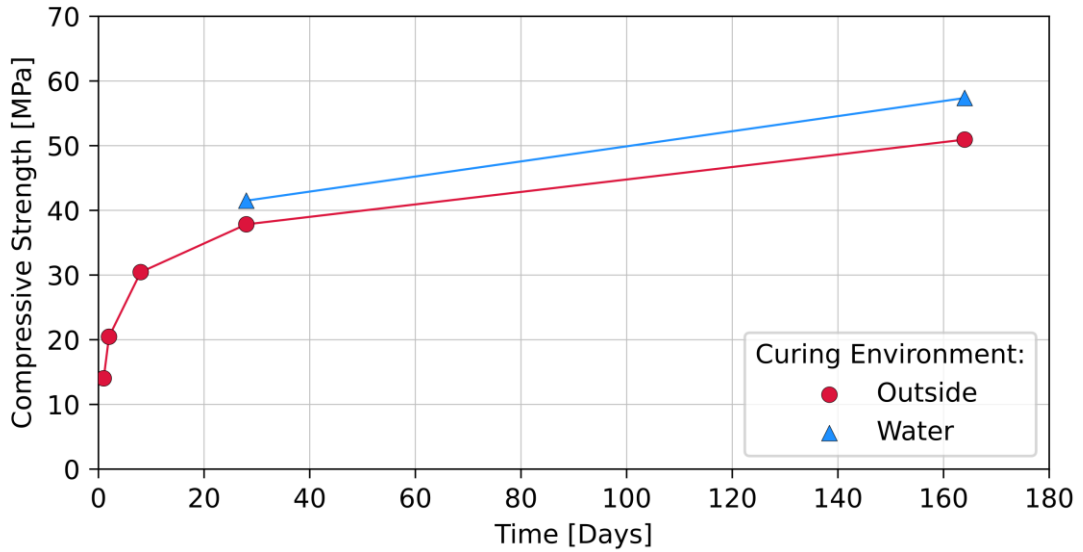


Figure 3-27 Compressive Strength

### 3.5.4 Tensile Strength

Literature indicates that concrete cracking can be related to the tensile strength of the concrete being exceeded (William et al., 2008). It is thus an important material property to consider. Cylinders with diameters and heights of 100 mm and 200 mm respectively were cast and cured in the same manner as described for the compressive strength specimens. For each test date and curing environment, two cylinders were cut in half and each of the halves tested according to SANS6253:2006. The test results are shown in **Figure 3-28**. The difference between the strengths obtained from the different curing environments are once again evident as the water cured samples were 16 % stronger after 28 days than the samples left outside. This difference increased with time.

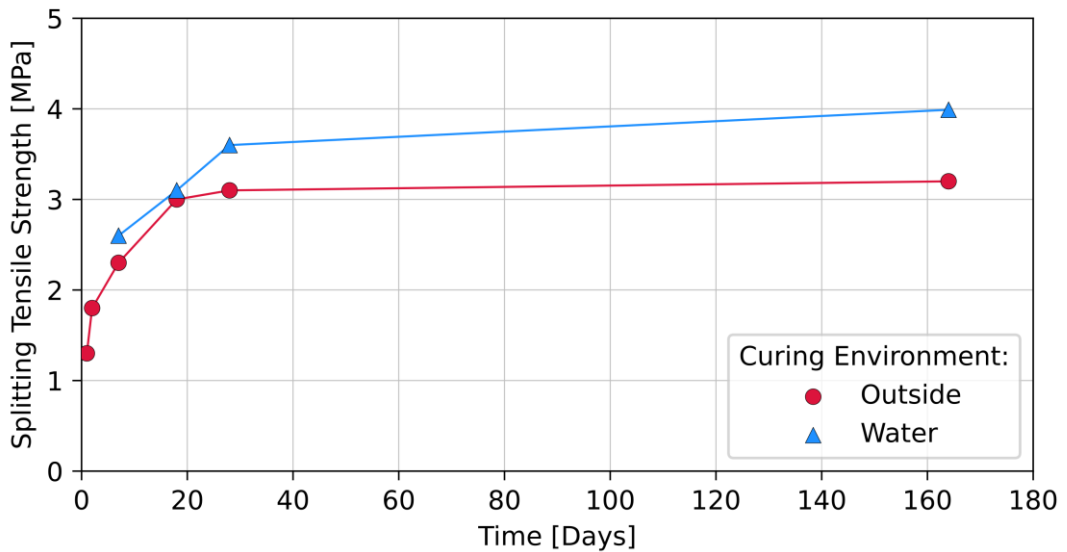
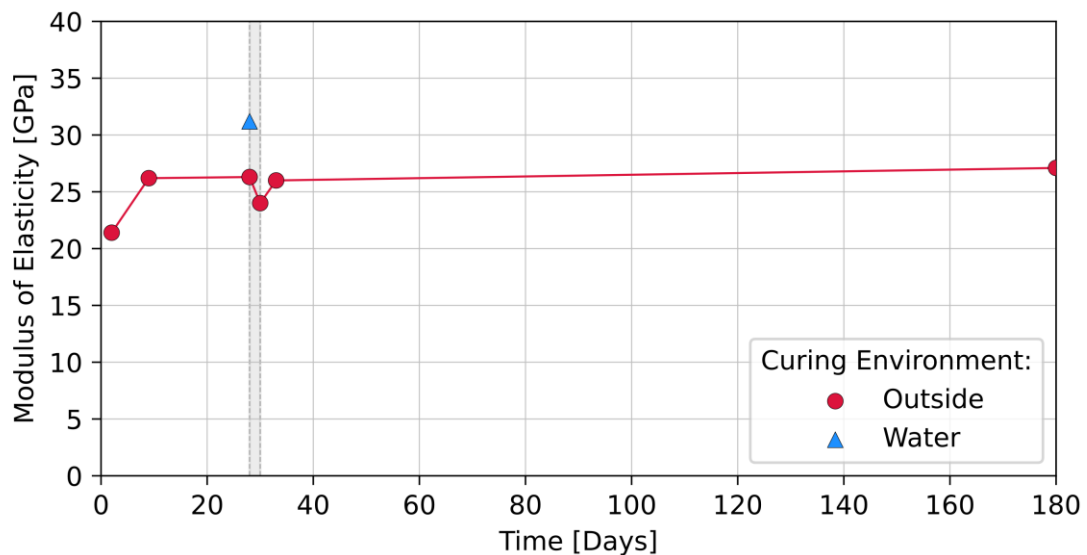


Figure 3-28 Tensile Strength

### 3.5.5 Modulus of Elasticity

The modulus of elasticity (E-value) of a material is defined as the ratio of uniaxial stress to the resultant axial strain (Alexander, 2021). As for the tensile strength, cylinders with diameters and heights of 100 mm and 200 mm respectively were cast to determine the E-value of the concrete. Once again, the two different curing environments were used and the results from testing the cylinders according to ASTM C469/C469M-22 are shown in **Figure 3-29**. At the 29-day mark there was a rainfall event, and the E-values of the outside specimens were tested again. It was interesting to note the decrease in E-value after the specimens were exposed to rain. The implication of this is that structures which are exposed to outside weather conditions will have varying stiffness depending on the weather conditions. For the calculations in this study, the E-value of the concrete was assumed to be constant and was taken as the 28-day E-value of the outside specimens of 26 GPa.

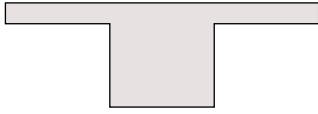
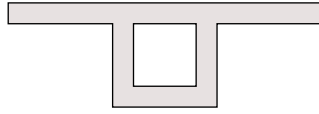


**Figure 3-29** Modulus of elasticity

### 3.5.6 Drying Shrinkage

The drying shrinkage of 100 x 100 mm unreinforced concrete prisms were determined using the change in length test method described in ASTM C157/C157M -17. After 6 months, the total drying shrinkage was measured to be 500  $\mu\epsilon$ . While the samples had the same thickness as the flanges of the T-beams, more of their surface area was exposed to the environment compared to their volume. As detailed in **Section 2.4.3**, TMH7:1989 provides a shrinkage prediction equation based on four partial coefficients dependent on effective thickness, relative humidity, concrete maturity and cement content. **Table 3-2** contains the predicted values calculated by using the equation detailed in TMH7:1989 (**Appendix A**).

**Table 3-2 TMH7:1989 predicted shrinkage values**

|   |  |  |
|---|--|---|
| Effective thickness ( $h_e$ ) according to TMH7:1989 [mm] | 175  | 130   |
| 28-day predicted shrinkage [ $\mu\epsilon$ ]              | 75   | 95  |
| 90-day predicted shrinkage [ $\mu\epsilon$ ]              | 155  | 205   |
| 180-day predicted shrinkage [ $\mu\epsilon$ ]             | 195  | 260   |

The values predicted by TMH7:1989 for 6 months is less than half of the measured drying shrinkage measured for the prism samples. SANS 10100-1:2000 also uses effective thickness and relative humidity to provide 6-month drying shrinkage predictions for plain concrete. SANS 10100-1:2000 predicted shrinkage strains of just below 200  $\mu\epsilon$  for the solid section and slightly above 200  $\mu\epsilon$  for the voided section.

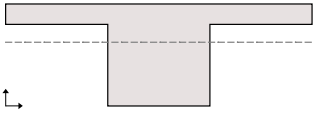
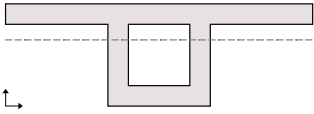
### 3.6 SUMMARY OF MATERIAL AND CROSS SECTION PROPERTIES

**Table 3-3** and **Table 3-4** present the representative material and cross-sectional properties of the concrete and T-beams respectively. The values given in **Table 3-3** are the 28-day representative values as recorded in **Section 3.5**. The E-value and CTE of concrete are considered constant for the duration of the study. Where applicable, the compressive and tensile strengths are used for comparison, the strengths for the date of comparison are used according to **Figure 3-27** and **Figure 3-28** respectively. The measured drying shrinkage at 180 days is also included as a material property, even though the measured prisms were unreinforced. The unreinforced measured shrinkage was compared to the effective shrinkage calculated for each cross-section in **Section 4.1.3**. The neutral axis value for each cross-sectional area is indicated from the bottom of the soffit upwards and all graphs indicating the height of the section using the same convention. The second moment of area for each cross section was calculated using the transformed cross section and hence the effect of the reinforcement was included. The effective thickness for each cross-section was calculated according to TMH7:1989 and the volume to surface area ( $V/A$ ) ratio was calculated as done by Tia et al. (2016) for comparison regarding heat of hydration. Furthermore, the area of each cross-section per unit width was included as it was used in conjunction with daily temperature ranges to compare to values presented by Emerson (1976), Black et al. (1976) and Skorpen et al. (2021).

**Table 3-3 Representative Material Properties**

| Material Property                    | Symbol           | Value                             |
|--------------------------------------|------------------|-----------------------------------|
| Casting time                         |                  | 14:50-15:50                       |
| Time of final set                    |                  | 21:15 03/04/2023                  |
| CTE of concrete                      | $\alpha_c$       | 11.9 $\mu\epsilon/^\circ\text{C}$ |
| 28-day Concrete compressive strength | $f_c$            | 37 MPa                            |
| 28-day Concrete tensile strength     | $f_{ct}$         | 3 MPa                             |
| 28-day Concrete E-value              | E                | 26 GPa                            |
| 180-day Concrete drying shrinkage    | $\epsilon_{dry}$ | 500 $\mu\epsilon$                 |
| E-value of reinforcement steel       | $E_s$            | 195 GPa                           |

**Table 3-4 Cross-section Properties**

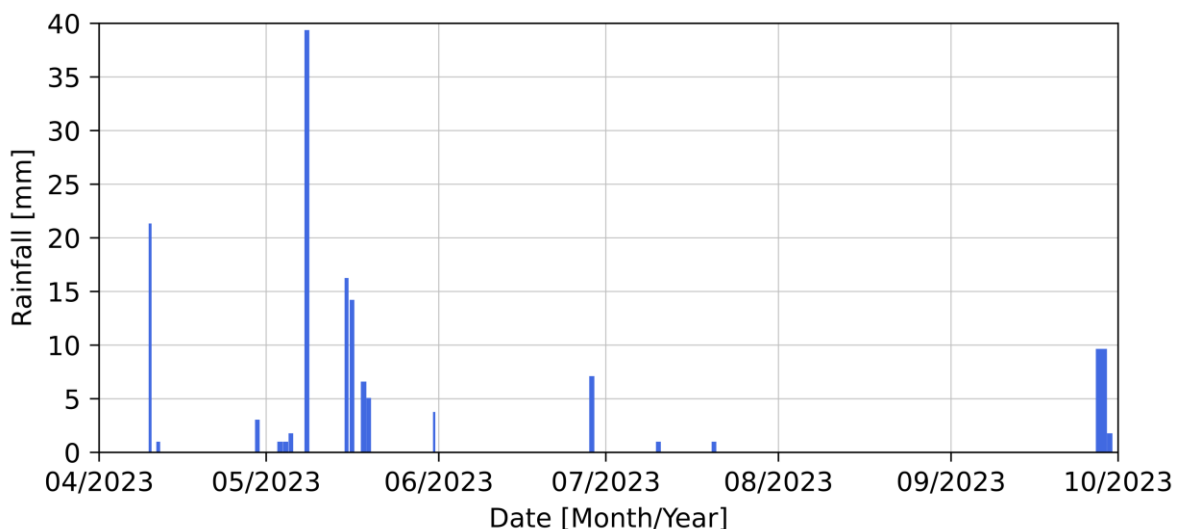
| Cross-section Property                                    |  |  |
|---|--|---|
| Cross-sectional area [m <sup>2</sup> ]                    | 0.35   | 0.26  |
| Neutral Axis (NA) [mm]                                    | 308.5  | 328.5   |
| Second moment of area (I) [mm <sup>4</sup> ]              | 8 216 853 676  | 7 128 544 803   |
| Effective thickness ( $h_e$ ) according to TMH7:1989 [mm] | 175  | 130   |
| V/A ratio after Tia et al. (2016) [m]                     | 0.70   | 0.54  |
| Area of cross-section per unit width [m <sup>2</sup> /m]  | 0.233  | 0.173   |

## 4 COMPARING SOLID AND VOIDED T-BEAM CROSS SECTIONS

In this chapter the response of the solid and voided T-beam cross sections to environmental loading is compared in terms of temperature and strain. The trends of effective temperature and strain over time are presented and discussed, along with a comparative analysis using existing literature and TMH7:1981, in terms of thermal inertia and temperature distributions. Furthermore, the stress profiles generated in response to temperature for a typical day are discussed and compared to the measured concrete tensile strength. The intention was to compare the different cross-sections response to environmental temperature loading and establish the tensile stress development based on typical temperature distribution for both sections.

### 4.1 MEASURED TRENDS

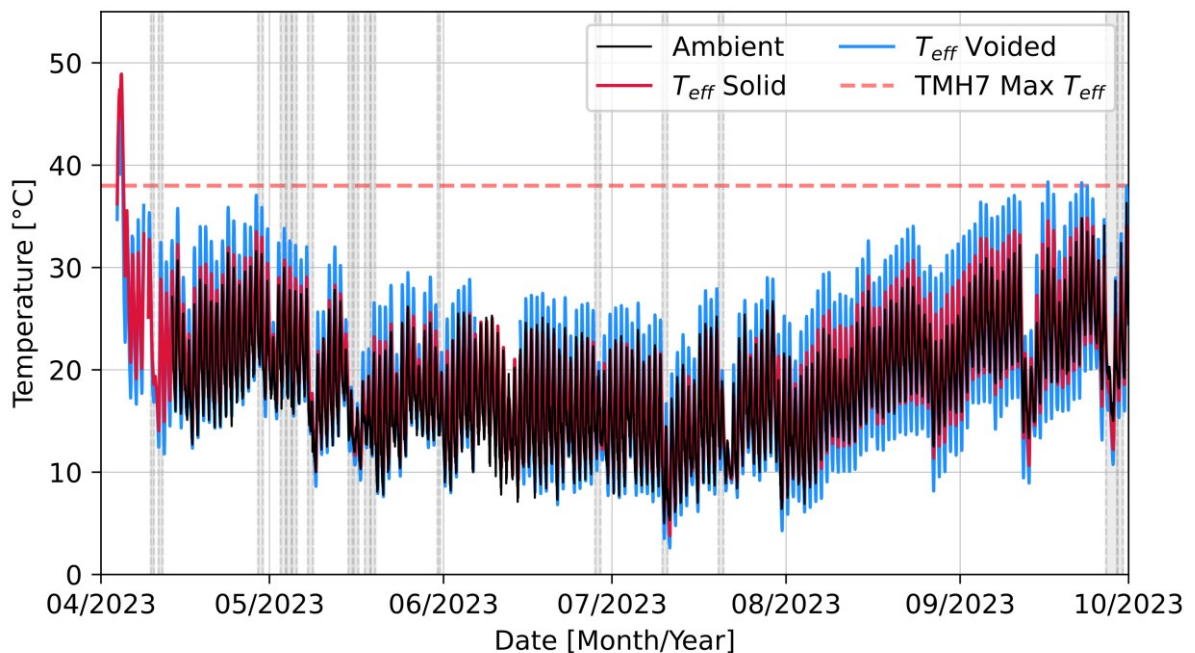
This section primarily focuses on the trends in temperature and strain caused by the environment over the duration of the study. It is important to note that the period of observation includes the seasons of Autumn, Winter and a portion of Spring for South Africa. The warmest time of the year is therefore not included in the study. The expected rainy season for Pretoria falls between October and March and therefore rain is typically not expected for the months included in this study. **Figure 4-1** displays the rainfall measured by the weather station for the duration of this study. There were uncharacteristically many rainfall events during the autumn to winter period and their effects were visible in the measured strains and correlate with decreased measured temperatures. For all subsequent graphs, rainfall events are denoted by vertical dashed lines and grey fill. This serves as a visual representation of the dates on which precipitation was measured and does not reflect the actual recorded quantity.



**Figure 4-1 Rainfall for the months of April to October 2023**

### 4.1.1 Temperature

The effective temperature ( $T_{eff}$ ) for both T-beams, along with the ambient temperature recorded by the additional thermocouple placed under the beams, is given in **Figure 4-2**. The effective beam temperatures follow the same trend as the thermocouple used for the ambient temperature. Both T-beams' effective temperatures surpass the minimum and maximum temperatures recorded by the thermocouple due to its placement detailed in **Section 3.3.4** and surroundings described in **Section 3.4**. As expected, the voided section was more sensitive to temperature changes; with a larger daily variation compared to the solid section throughout the recorded period. This behaviour can be attributed to its lower thermal inertia as discussed in **Section 3.2**. The daily effective ranges for each cross section were calculated and the average range as well as the maximum range is displayed in **Table 4-1**. On average, the daily variation for the voided section was 5 °C larger than the solid section and the difference in daily temperature range became more pronounced in the warmer months (from August onwards). This coincides with the time of the maximum temperature range given in **Table 4-1**. It is therefore likely that the difference in effective temperature between the sections would increase if the summer months were also included.



**Figure 4-2 Effective temperatures over time**

**Table 4-1 Effective Temperature Ranges**

| Daily Temperature Range [°C] | Solid | Voided |
|------------------------------|-------|--------|
| Average                      | 11.4  | 16.7   |
| Maximum                      | 16.5  | 23.4   |

The maximum effective temperature of 38 °C for the region and altitude suggested by TMH7:1981 Part 1&2 is denoted by the horizontal dashed line in **Figure 4-2**. The minimum effective temperature

from the same guidelines was calculated as  $-3\text{ }^{\circ}\text{C}$ . The temperatures for both sections remain within the ranges of  $-3$  to  $38\text{ }^{\circ}\text{C}$  for the majority of the time included in the study but during Spring,  $T_{eff}$  of the voided section started to surpass the maximum of  $38\text{ }^{\circ}\text{C}$ . It is expected that a dark asphalt surfacing would increase the recorded surface temperatures of both beams, further increasing the effective temperatures. However, it is worth noting that the TMH7:1981 guidelines are intended for larger bridge cross-sections which would be considerably larger and hence have lower effective temperatures. Thus, it is not of particular concern that the voided section reaches and surpasses the expected maximum presented by the guideline. It is also notable that neither section reached an effective temperature below  $4\text{ }^{\circ}\text{C}$ , even during the coldest time of the year. The maximum and minimum weather station and thermocouple data is given in **Table 4-2**. The difference between the weather station and ambient thermocouple was explained in **Section 3.3.4**. Since the minimum temperature recorded since 2021 is  $-2\text{ }^{\circ}\text{C}$  and temperatures in the area hardly ever reach far beyond sub-zero, it is unlikely that cross sections of any size will reach the  $-3\text{ }^{\circ}\text{C}$  set by the guideline.

**Table 4-2 Maximum and Minimum recorded Temperatures**

| Year    | Weather station |      |      | Ambient Thermocouple |
|---------|-----------------|------|------|----------------------|
|         | 2021            | 2022 | 2023 | 2023                 |
| Maximum | 34.4            | 35.8 | 35.4 | 37.6                 |
| Minimum | -2.0            | -0.7 | 0.5  | 6.5                  |

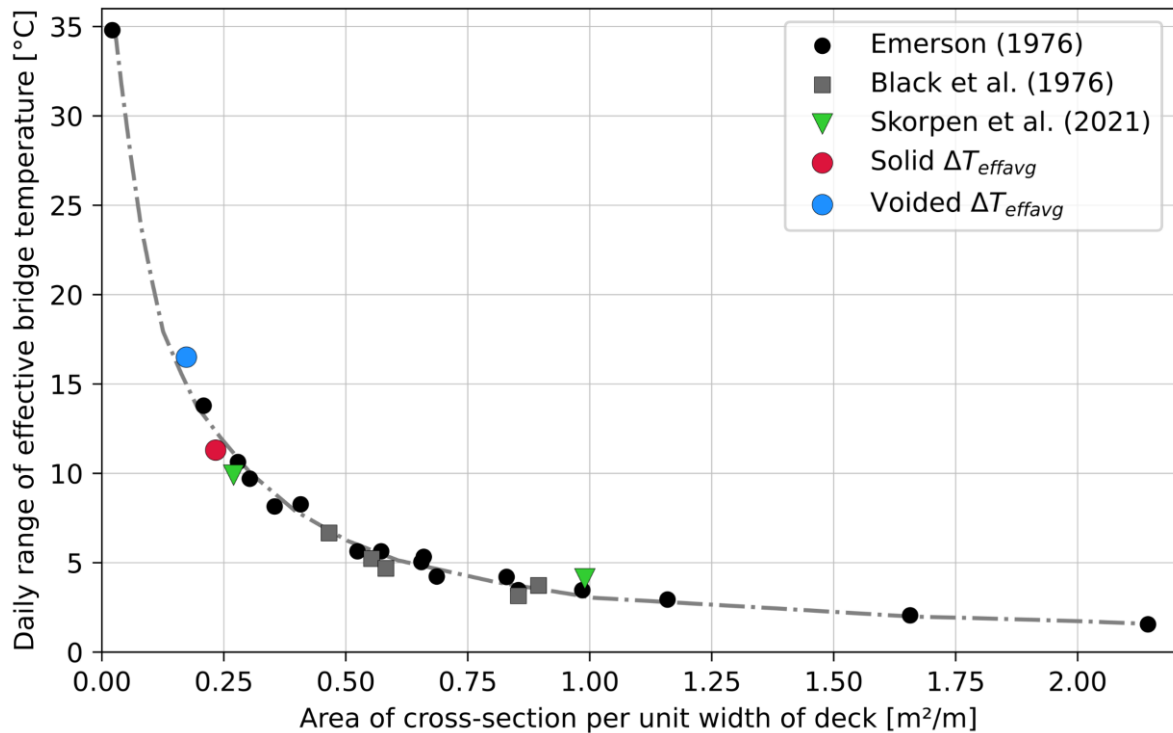
Black et al. (1976) showed that daily effective bridge temperature can be related to the area of the cross-section per unit width of deck. Emerson (1976) produced similar results by calculating the temperature range of sixteen different cross-sections; for a day with high solar radiation and a large range of shade temperature so that a large temperature range would be achieved. The calculation which produced the temperature ranges were made using input values applicable to the UK, therefore some differences in solar radiation and shade temperature are expected between the UK and South Africa. **Figure 4-3** includes the results presented by Black et al. (1976) and Emerson (1976) as well as points from an integral bridge in South Africa, reported by Skorpen et al. (2021). The average temperature range for each section with the applicable cross-sectional area per unit width calculated in **Section 3.6** are included in **Figure 4-3**. These results showed a good correlation with the trend observed by the mentioned authors.

**Figure 4-2** displays the results for the effective temperature of each cross section in comparison with the effective extrema in the TMH7:1981 guideline. However, TMH7:1981 also provides a vertical temperature distribution. **Figure 4-4** shows the comparison of the vertical temperature distributions for each section at the times corresponding to their minimum and maximum effective temperatures, to the positive and reverse temperature distributions calculated according to TMH7:1981 (**Appendix A**). For the purpose of comparison to TMH7:1981, the maximum effective temperatures produced purely by

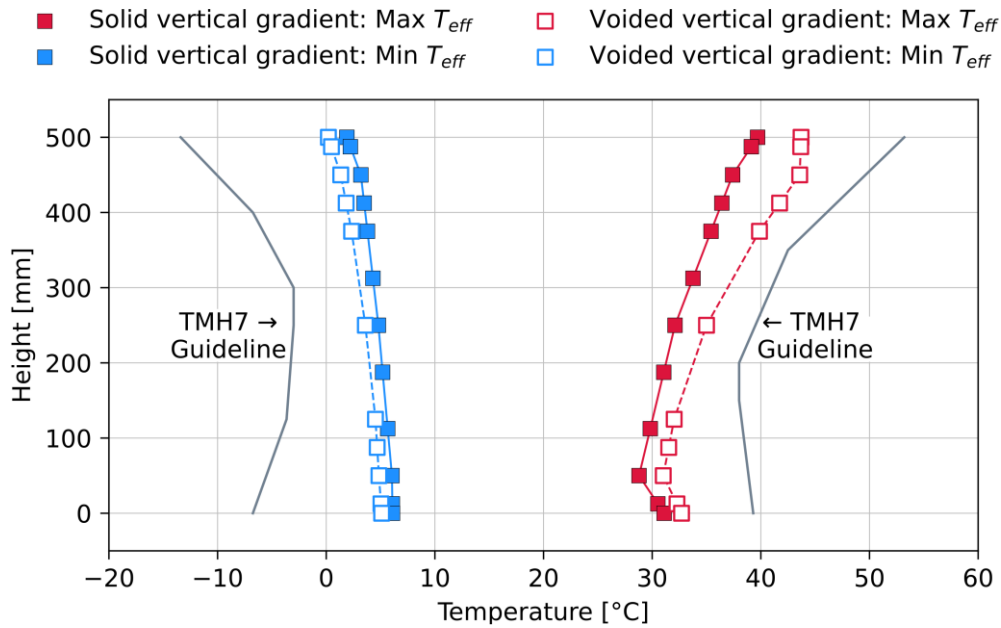


## COMPARING SOLID AND VOIDED T-BEAM CROSS SECTIONS

environmental conditions were considered, therefore the temperatures generated by the heat of cement hydration were excluded. The vertical temperature distribution for the solid section was generated by using temperature points through the section's centre. For the voided section, the distribution was compiled using temperatures through the web portion of the section. This was done throughout the study to accommodate the subsequent theoretical strain and stress calculations as no strain nor stress can develop in the void of the section. Furthermore, to assist with strain and stress calculations, additional temperature points were created through interpolation between measured points. Both measured and interpolated values are plotted for temperature figures and dependent strain and stress figures calculated from temperature. The minimum effective temperatures were 3.7 °C and 2.6 °C, while the maximum effective temperatures were 35.7 °C and 39.4 °C for the solid and voided beams respectively. The corresponding minimum and maximum ambient temperatures were 6.5 °C and 37.6 °C respectively. Again, as was shown in **Figure 4-2**, the voided section had more extreme temperatures. The vertical distributions remained within the TMH7:1981 guidelines and the measured distribution follows a similar shape to that created for the positive distribution by TMH7:1981. For the reverse distribution, the vertical temperatures for both sections remain uniform and this suggests the reverse distribution calculated according to TMH7:1981 may be exaggerated for the relatively small section sizes used in this study. Overall, the shapes and temperatures predicted by TMH7:1981 provided acceptable guidelines which can be applied to concrete elements in general, in addition to bridge sections.



**Figure 4-3 Daily effective temperature range versus area of cross-section per unit deck width**



**Figure 4-4 Comparison of vertical temperature distributions to TMH7:1981**

#### 4.1.2 Strain

The environmental conditions created strains within both T-beams. The strains discussed in this section are those recorded by the VWSGs introduced in **Section 3.3.3**. The total strains recorded for selected positions in each of the cross-sections are shown in **Figure 4-5**. The increasingly negative strain values for both sections indicated a general shortening of the beams over time, which was expected as the concrete experienced shrinkage. Since the beams were free to move, the shortening caused by shrinkage would have caused tensile stresses in the sections if they were restrained. The effect of daily temperature fluctuations was also evident in all strain readings but more so by the bottom gauges (S2 and V2), as the bottoms of the beams were somewhat shielded from the direct environmental effects experienced by the top gauges. For the solid T-beam, the flange section was more susceptible to daily temperature variations and experienced more shrinkage than the centre, which is shown by the larger daily strain range and greater increase in negative strain readings overtime when gauges S1 and S4 are compared. Contrastingly, the flange and centre portion of the voided T-beam experienced similar thermal stain and shrinkage as indicated by the comparable daily strain ranges and decrease in strain trends. The mechanical strains due to the self-weight of the beams were included in the total measured strain. At a height of 450 mm above the soffit, the strain induced by self-weight was calculated as  $3 \mu\epsilon$  and  $2 \mu\epsilon$  for the solid and voided sections respectively. At a height of 50 mm the strains were calculated as  $-6 \mu\epsilon$  and  $-5 \mu\epsilon$  in the same order. Due to the small magnitude of these strains, their influence was considered negligible. William et al. (2008) made a similar assumption, contending that temperature induced strains reaching up to  $150 \mu\epsilon$ , an order of magnitude greater than the  $6 \mu\epsilon$  attributed to self-weight.

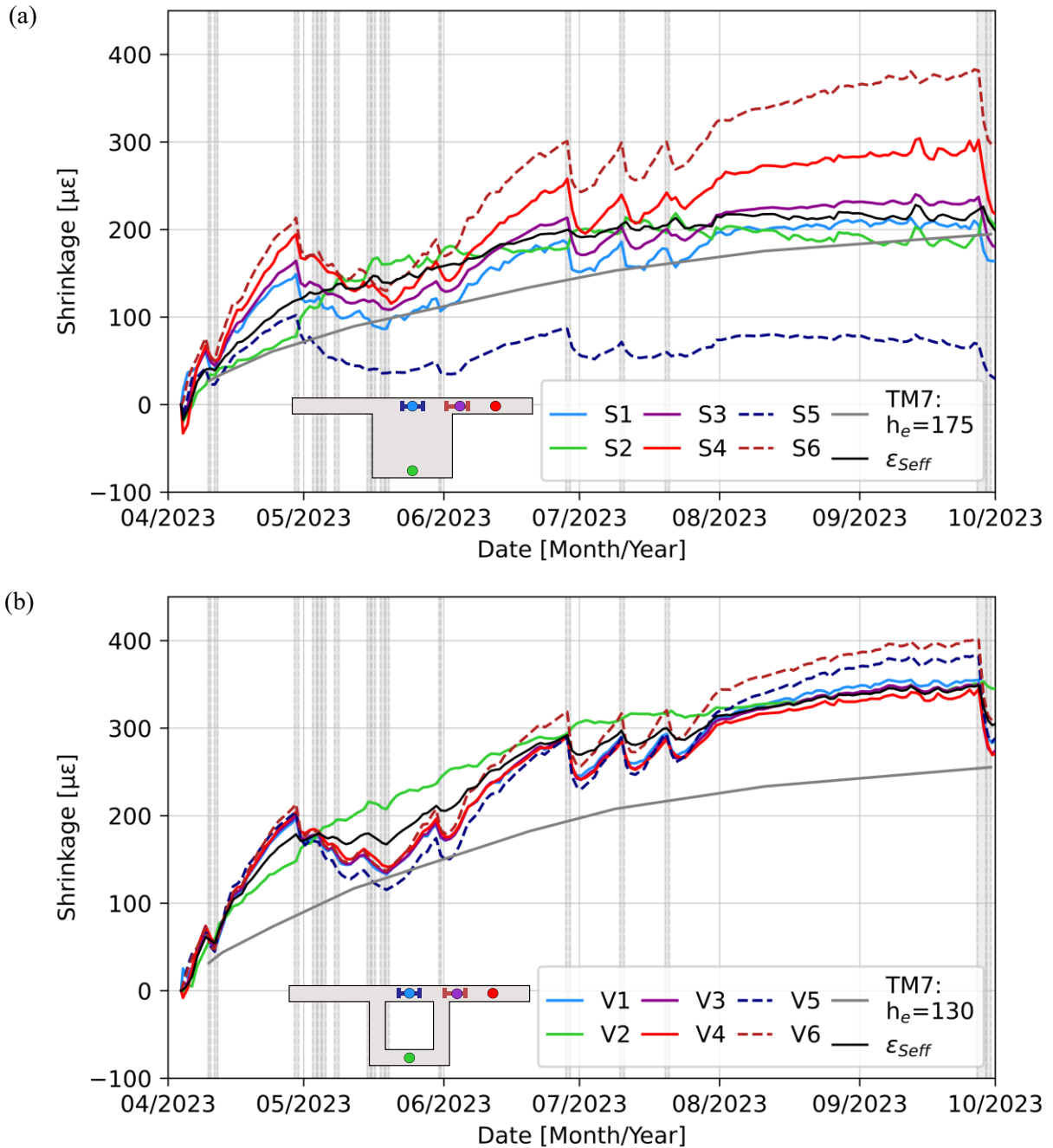
COMPARING SOLID AND VOIDED T-BEAM CROSS SECTIONS



Figure 4-5 Total measured strains at selected positions of the (a) solid and (b) voided T-beam

### 4.1.3 Shrinkage

The mechanical strain caused by shrinkage was calculated for each VWSG by removing the thermal strain component from the total measured strains. The strains were measured from the time of final set of the concrete and therefore the shrinkage strains contain both early age and drying shrinkage over time. Although shortening caused by shrinkage is recorded as a negative strain, shrinkage is plotted as a positive value. Therefore, negative shrinkage strains can be referred to as swell. The measured shrinkage for each gauge is plotted in **Figure 4-6**.



**Figure 4-6** Shrinkage measurements for the (a) solid and (b) voided T-beam

The dashed lines denote the VWSGs placed in the transverse direction while the solid lines denote the VWSGs placed in the longitudinal direction. For the solid beam, the shrinkage of the top section increased substantially from the centre outwards to the flange, whereas the voided beam showed similar shrinkage across the top portion. The effective shrinkage strain ( $\epsilon_{seff}$ ) is a weighted average shrinkage value for the longitudinal direction of each section, calculated using gauges 1 to 4, in the same way as the thermocouples were used to calculate effective temperature. Based on the effective shrinkage values, it is clear that the voided beam experienced larger shrinkage, with shrinkage reaching a near constant value in the region of  $350 \mu\epsilon$  after 5 months, compared to solid beam's  $210 \mu\epsilon$ . The effects of the rainfall events in Autumn were significant for both beams, particularly across the top portion of the beams. Approximately  $50 \mu\epsilon$  of shrinkage of the top portions was reversed by the rain events in May and it is arguable that the total measured shrinkage was reduced by the regular occurrence of rain. It is notable that the beams did not have any surfacing as would be present for bridges and buildings, therefore it is debatable whether the shrinkage behaviour would be altered in the presence of surfacing or sealants. However, a valid counter argument can be made that the majority of shrinkage deformation occurred within the first four months after casting and therefore within a construction timeframe, surfacing would not yet be applied and so the shrinkage behaviour should be considered. Furthermore, a difference in shrinkage can be seen between the top and bottom portions of both cross-sections. The difference was roughly  $50 \mu\epsilon$  between the bottom and top centre gauges for both beams before the rainfall took place at the end of April. The bottoms of both beams were shielded from the rain, as gauges S2 and V2 showed increased shrinkage throughout the observation period.

Irrespective of the occurrence of rain, the effective (weighted average) shrinkage estimated using the effective thickness ( $h_e$ ) and methodology described in TMH7:1989 underpredicts the measured shrinkage for both beams, especially within the first month after casting. At the 6-month mark, the prediction produced an underestimation of  $100 \mu\epsilon$  and  $30 \mu\epsilon$  for the voided and solid beams respectively. The measured drying shrinkage of  $100 \times 100$  mm unreinforced prisms after 6 months was  $500 \mu\epsilon$ , which was a much closer estimate of the effective shrinkage of the voided section than predicted by TMH7:1989. The thickness of the prisms was the same as the thickness throughout the voided section and the difference between the shrinkage values can be attributed to the presence of reinforcement in the T-beam and the difference in surface areas exposed to the atmosphere. Nonetheless, the drying shrinkage measured for the unreinforced prisms provided a good indication of potential effective shrinkage of the voided T-beam. Contrastingly, the drying shrinkage of the prisms vastly overestimates the shrinkage when compared to the solid section. For the solid T-beam, the most accurate prediction of shrinkage strains is produced by using SANS 10100-1:2000 which predicted shrinkage strains of close to  $200 \mu\epsilon$ , 6 months after casting. The disadvantage of SANS 10100-1:2000 is that a curve of shrinkage over time cannot be created and therefore development of shrinkage over the first few months after set cannot be predicted. These results highlight the need to develop shrinkage prediction models

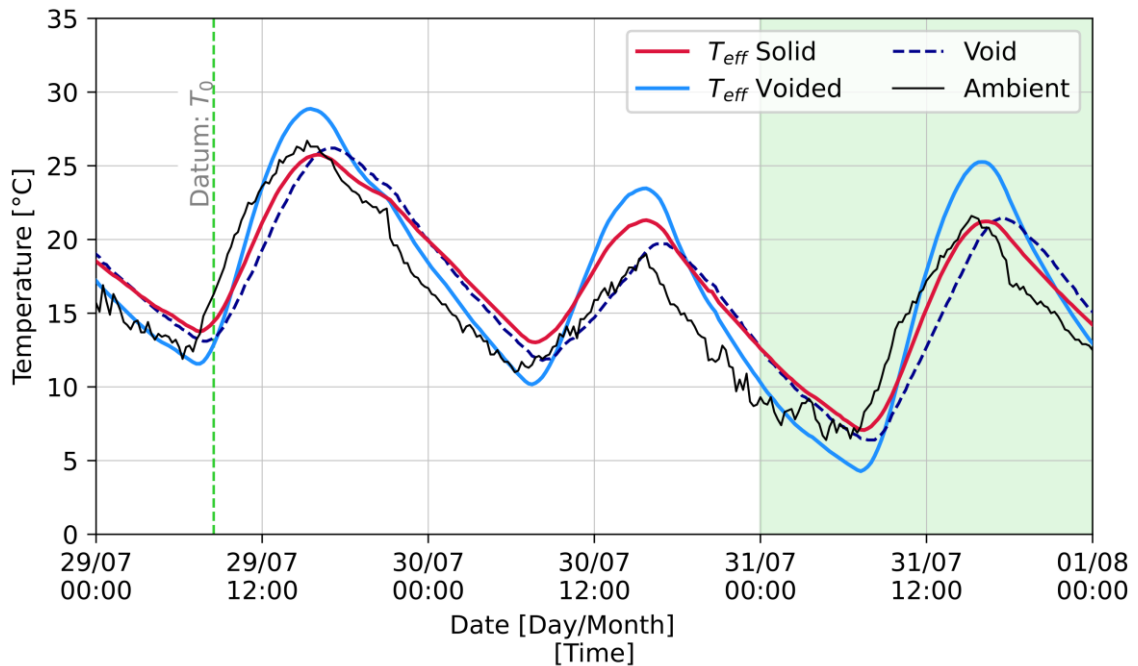
which can accurately predict shrinkage for different sizes of section and effective thicknesses for South African conditions, especially at early ages.

For the voided beam there were marginal differences between the shrinkage measured in the top section by the longitudinal and transverse gauges. Conversely, a large difference was evident between the transverse direction and the longitudinal direction for the solid beam. At the transition from solid central segment to flange, gauge S6 recorded shrinkage values very similar to those of the flange of the voided section, which suggests the shrinkage of the solid beam's flange is significantly restrained in the longitudinal direction by the adjacent solid section. VWSG S5 deviates from the other gauges in the solid section from the early stages. It measured less shrinkage than the other top gauges leading up to the Autumn rainfall and thereafter measured small deformations. This behaviour suggests that cracking occurred within the top portion of the solid T-beam, which will be discussed in **Section 4.5** and **Section 5.2**.

## 4.2 TYPICAL DAILY TEMPERATURE DISTRIBUTIONS

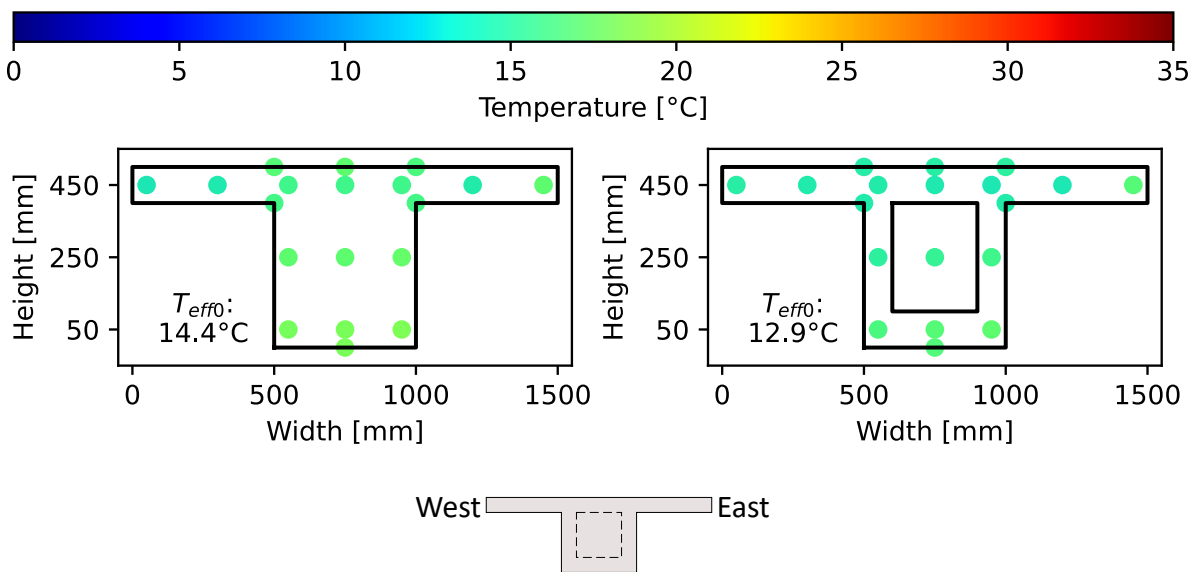
Changes in temperature cause strains within concrete, regardless of cross-section. The stresses which develop are dependent on restraint conditions as well as the type of temperature distribution as discussed in **Section 2.3.2**. Therefore, the temperature distributions are required to calculate subsequent strain and stress profiles within each cross-section. In this section, the temperature distributions for a typical day of both solid and voided T-beams are presented. The complete temperature distribution throughout the cross-section of both solid and voided T-beams are given for a typical day, after which the vertical and transverse temperature distributions for the same day are isolated and presented. Vertical temperatures refer to the measured temperatures through the depth of each beam and are denoted by height above the soffit. As mentioned in **Section 4.1.1**, the temperatures for the voided T-beam were taken through the web portion as opposed to the centre for the solid T-beam. Transverse temperatures refer to the temperatures across the width of the centre of the top 100 mm portion of each T-beam.

The effective temperatures (**Equation 3-9**) of both T-beams along with the ambient temperature and temperature recorded within the void of the voided beam are given for a 3-day period at the end of July 2023 in **Figure 4-7**. For the conditions included in this study, the effective temperatures in the 3-day period were considered representative of typical conditions. The temperature of the void was included to show that the polystyrene used to close off either end of the void was effective in simulating continuous conditions by minimising the temperature fluctuations caused by the ambient outside temperature.



**Figure 4-7 Effective temperatures for 29/07/2023 to 01/08/2023**

In order to complete subsequent strain and stress calculations presented in **Section 4.3** and **Section 4.4**, using the methodology detailed in **Section 3.3.2**, a datum temperature was selected at a time where the effective temperatures were similar for both T-beams and the temperature distributions throughout the cross-sections were as uniform as possible. The selected datum ( $T_0$ ) is denoted by the green dashed line in **Figure 4-7** and the temperature distributions for both T-beams are illustrated in **Figure 4-8**. The chosen datum allowed fair comparison of the different cross sections in both vertical and transverse directions. The effective temperatures for each cross-section at the selected datum are given as  $T_{eff0}$  in **Figure 4-8**.  $T_0$  essentially represents the temperature at the time which the boundary conditions are applied and therefore the reference point for stress development.

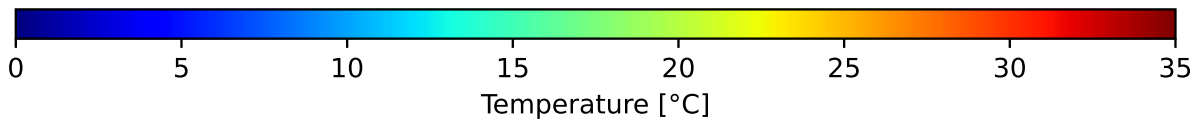


**Figure 4-8** Temperature distributions ( $T_0$ : 29/07/2023 at 08:30)

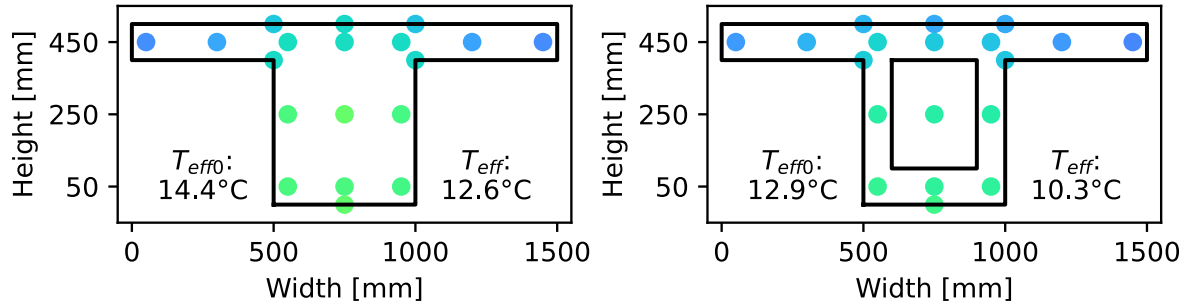
The 24 hours shaded in green in **Figure 4-7**, where selected as the day to compare the temperature distributions and behaviour of the different cross-sections, since it contained the largest range in ambient temperature of the 3 days. **Figure 4-9** and **Figure 4-10** contain the full temperature distributions for both cross-sections at intervals of 3 hours for the selected day. The orientation of the beams was the same as in **Figure 4-8**, where the flange denoted by the width measurement of 0 mm pointed toward the West and the flange denoted by the 1500 mm pointed toward the East. As in **Figure 4-8**, the effective temperatures at the selected datum are given at the bottom left as  $T_{eff0}$  for each time in **Figure 4-9** and **Figure 4-10**. Similarly, the effective temperature for each time and cross-section are given at the bottom right as  $T_{eff}$ .



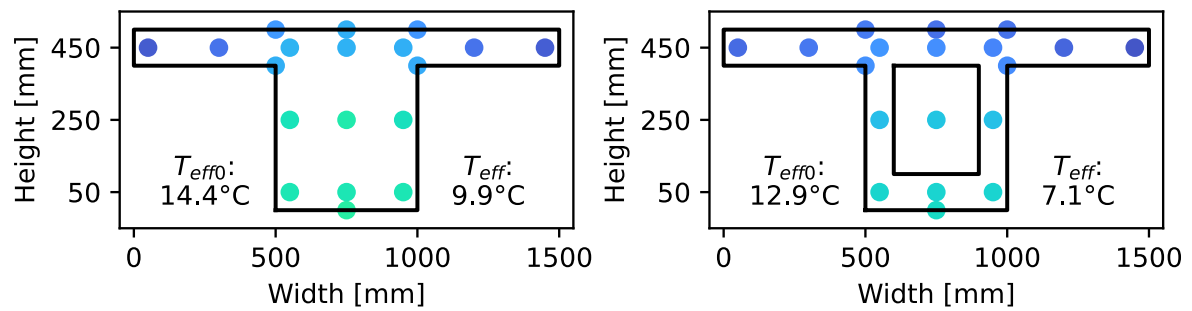
## COMPARING SOLID AND VOIDED T-BEAM CROSS SECTIONS



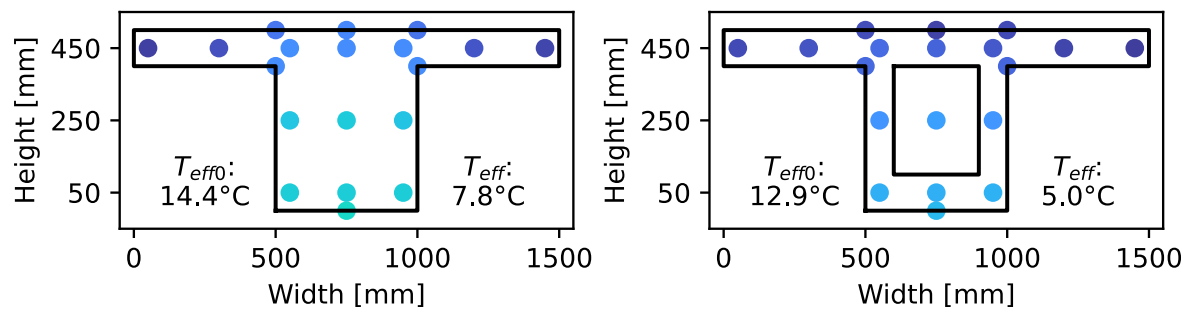
Time: 00:00



Time: 03:00



Time: 06:00



Time: 09:00

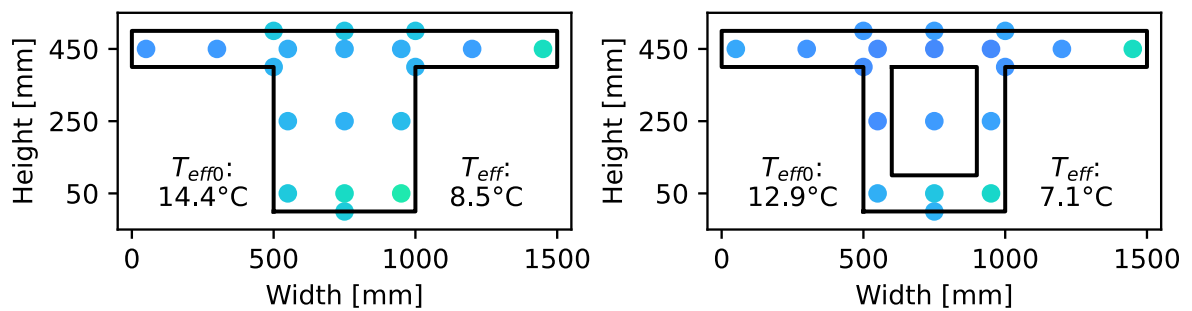
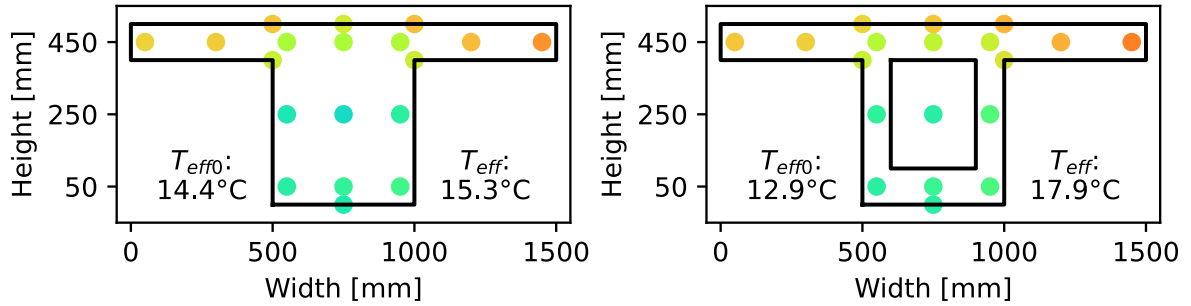


Figure 4-9 Temperature distributions from 00:00 to 09:00 on 31/07/2023

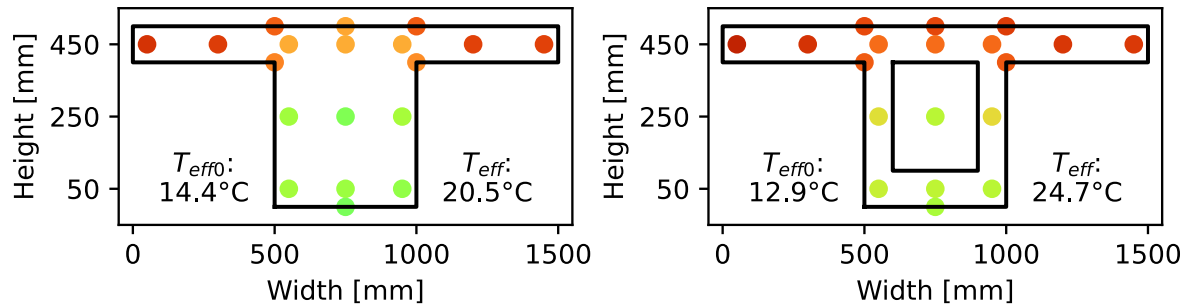
COMPARING SOLID AND VOIDED T-BEAM CROSS SECTIONS



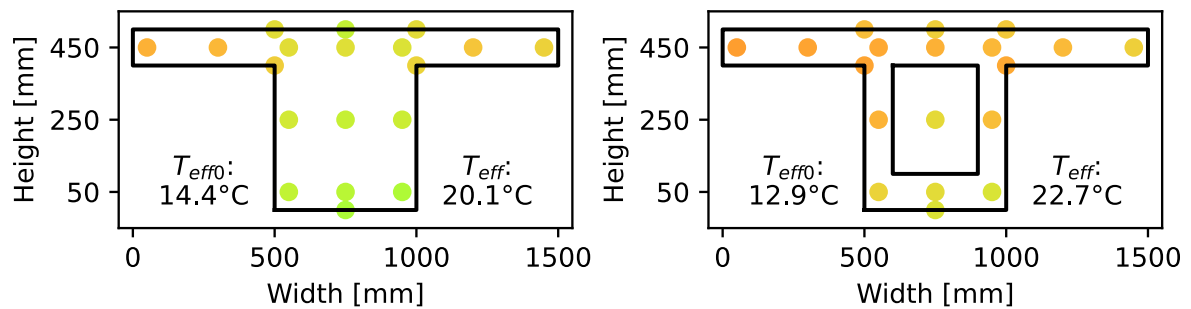
Time: 12:00



Time: 15:00



Time: 18:00



Time: 21:00

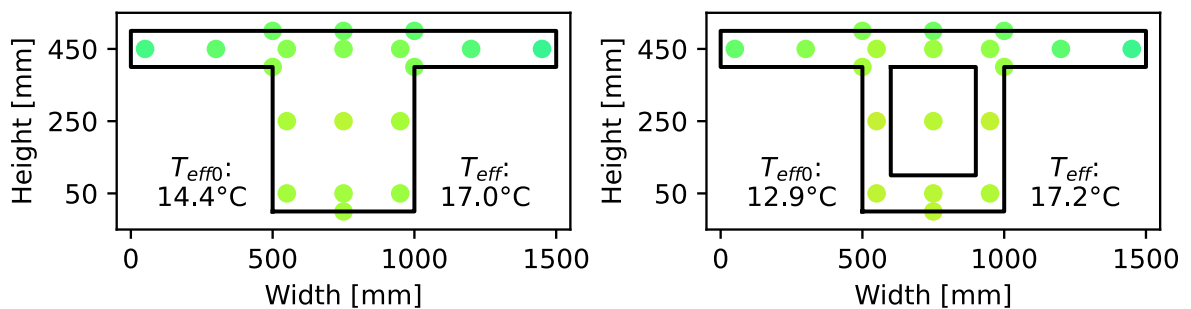


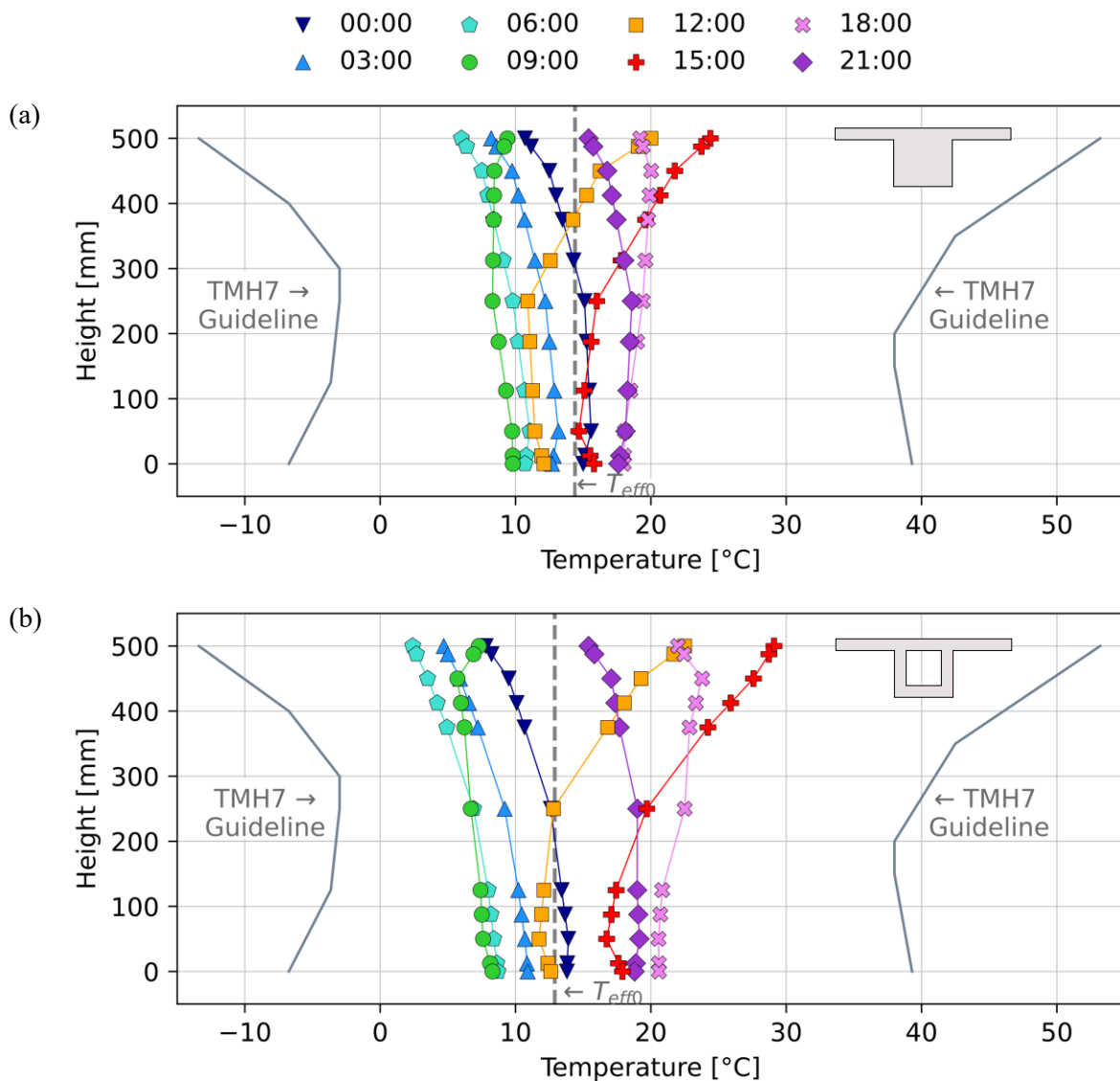
Figure 4-10 Temperature distributions from 12:00 to 21:00 on 31/07/2023

At 00:00 on 31/07/2023, both T-beams still retained some of the heat from the day before at their cores. The solid beam's core had a higher temperature than the voided beam which contributed to the higher effective temperature for the time as well but the flange temperatures were similar. The cores and flanges continued to cool down as the retained heat from both T-beams continued to dissipate. The lowest effective temperatures were reached at 06:00 and 07:00 for both beams. The core of the solid T-beam remained warmer than the voided T-beam's core while the edges of both beams' flanges dropped to below 5 °C. The sunrise was at 06:46 and as the sun rose, the East-facing flanges gained heat first, and as the time progressed to mid-day the top portions gradually displayed even temperatures. The maximum effective temperatures were reached shortly after 15:00, and while both T-beam's flanges showed temperatures of approximately 30 °C, the top centre part of the solid T-beam remained markedly cooler, whilst the top centre part of the voided T-beam reached similar temperatures than the flanges. As the sun descended (sunset at 17:41), the West-facing flanges retained their heat while the East-facing flanges began to cool down. Notably the effective temperatures at 21:00 were very similar for the two T-beams, but the voided section's temperature was quicker to respond environmental conditions, which was expected due to its lower thermal inertia.

The vertical temperature distributions for the selected day were isolated and plotted at 3-hour intervals to generate **Figure 4-11**. Based on this plot the difference in temperature range between the T-beams are once again evident. Additionally, the difference between top and bottom temperature for both beams are more clearly defined, albeit more prominent for the voided section. The presence of the void had a significant effect on the shape of the temperature distribution through the depth of the beam, creating a more prominent 'C-' or mirror 'C-' like shape at the warmest time, compared to the solid beam. The vertical temperature distribution shapes for both cross-sections match the nonlinear temperature profiles presented in literature of experimental work (Chen et al., 2009; Rodriguez 2012; Peirettie et al., 2014; Gu et al., 2014). Furthermore, both sections remain well within the TMH7:1981 guidelines for the selected typical day.

For each time and cross-section, a unique effective temperature can be calculated, which is the dominant factor in longitudinal movement. However, if the weighted temperatures and areas discretised for effective temperature are used in conjunction with the assumption that rotation takes place around a section's centroid and that planes remain plane during bending, a temperature plane can be created. The effective temperature of the section is still the temperature at the plane and section's centroid, but the difference between the top and bottom temperatures creates curvature within the plane section. Temperature planes for the solid section were plotted in **Figure 4-12** for times where the curvature in both the vertical and transverse direction could clearly be seen. **Figure 4-12 (a)** includes the vertical measured temperature distributions. The effect of the flange temperatures on the planes becomes clear since the measured vertical temperatures lie to one side of the plane for both time increments presented.

In **Figure 4-12 (b)** the transverse temperature distributions were plotted relative to the temperature planes to further demonstrate not only the effect of the flanges but how far measured values can be from the described temperature plane and even more notably, the effective temperature of a section at a given point in time. The same temperature planes could be plotted for the voided section, but the solid section was used as the example case for explanation purposes. Stemming from the difference between the measured values and the temperature plane created, the transverse temperature distributions for the same selected day were plotted in **Figure 4-13**. The transverse temperatures of the voided beam were fairly uniform for the flanges and centre portion, which can be explained by the uniform thickness across the top portion of the beam because of the void. The temperatures in the flanges of the solid beam were similar to the voided beam's flanges. Contrastingly, the solid beam's centre segment lagged behind the temperature in the flanges.



**Figure 4-11 Daily vertical temperature distributions for the (a) solid and (b) voided T-beams on 31/07/2023**

COMPARING SOLID AND VOIDED T-BEAM CROSS SECTIONS

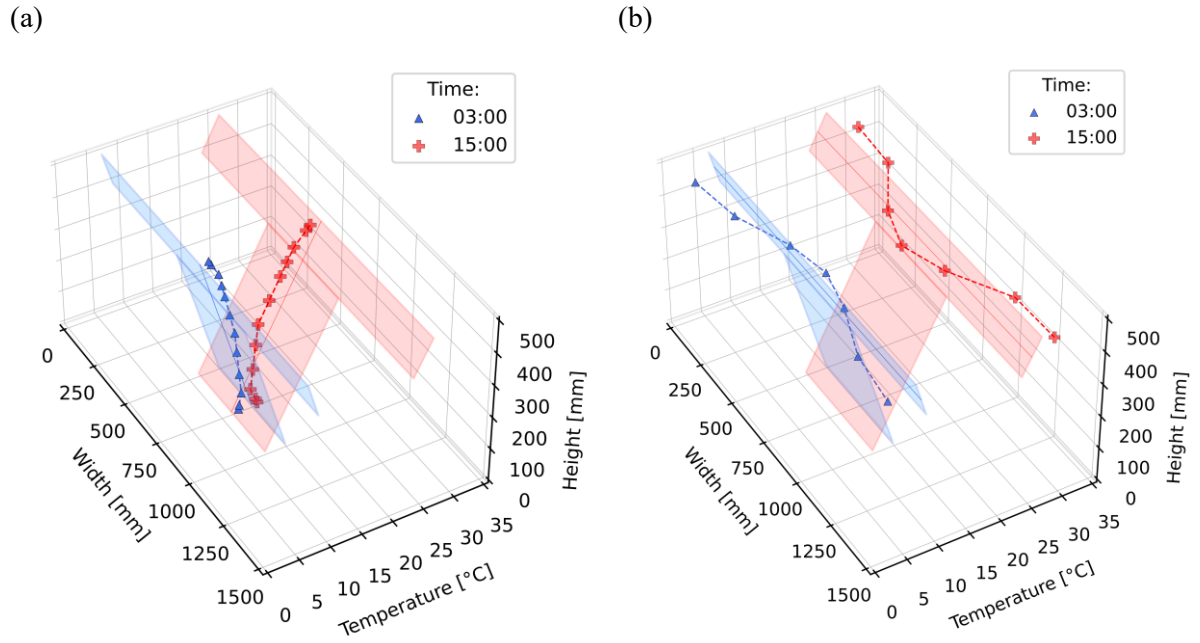


Figure 4-12 Temperature planes with (a) vertical and (b) transverse measured temperature distributions for solid T-beam

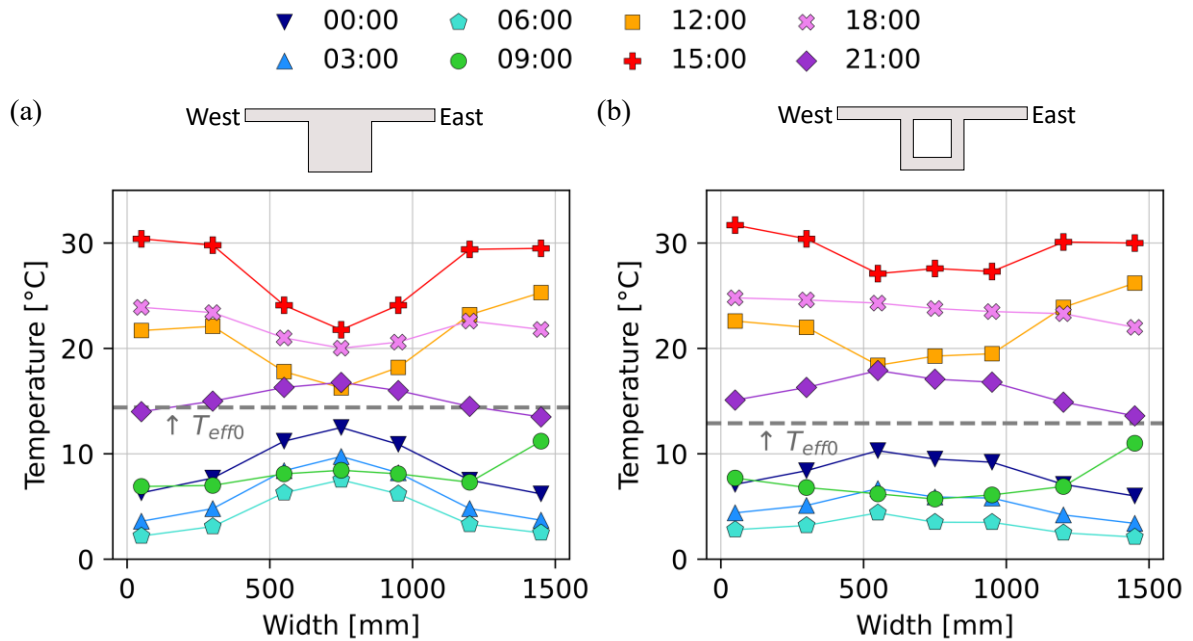
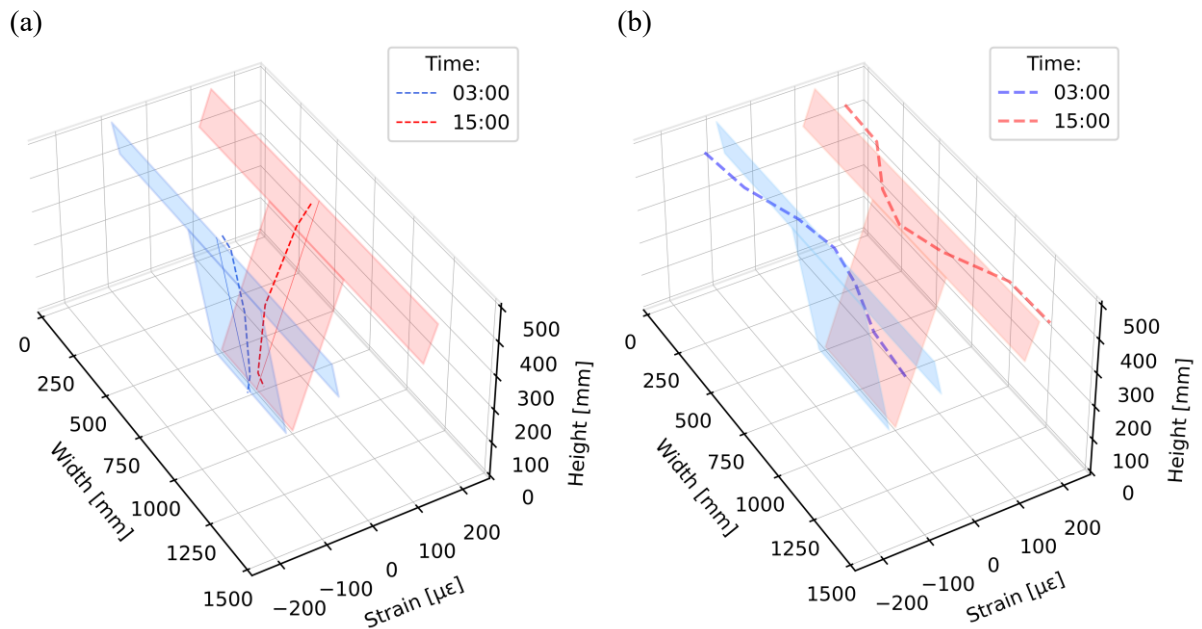


Figure 4-13 Daily transverse temperature distributions of the (a) solid and (b) voided T-beams on 31/07/2023

### 4.3 TYPICAL DAILY CALCULATED STRAIN

As discussed in **Section 3.3.2**, the change in temperatures in the cross-section causes strains in beams which are free to move and nonlinear temperature distributions will cause self-equilibrating stresses in sections regardless of boundary conditions. It follows from the temperatures presented before that the temperature distributions in both sections were nonlinear and hence self-equilibrating stresses would develop. In order to calculate the self-equilibrating stresses as well as the components of effective temperature stress and curvature stress caused by temperature, the strains caused by temperature variations at relevant points in time were evaluated. Furthermore, the effect of the flange temperatures on the temperature planes were clearly shown in the temperature distributions and highlighted why the transverse direction should also be considered. As such, the strains in both the vertical and transverse direction used to calculate the subsequent thermal stresses of both sections are presented in this section.

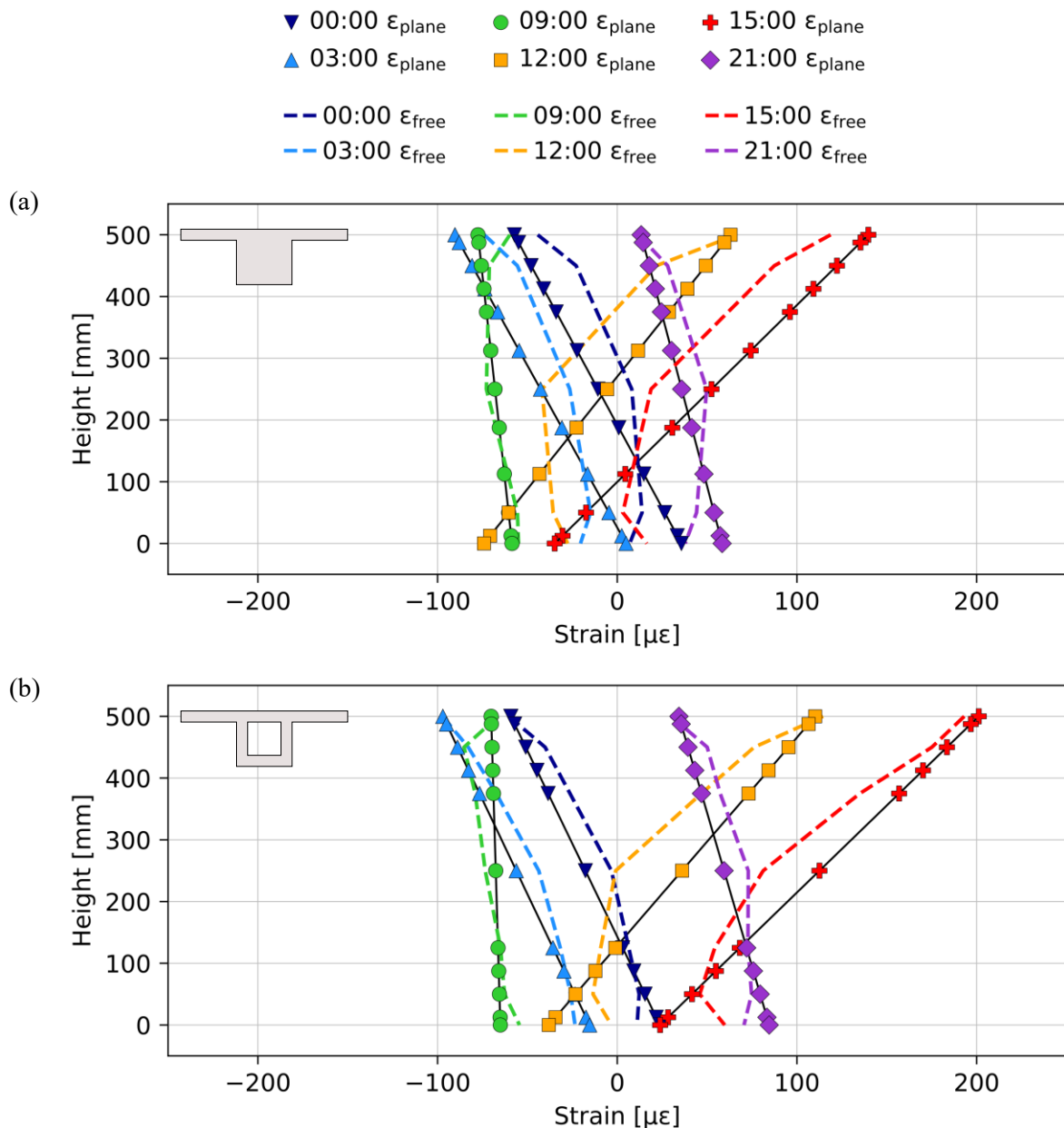
If the temperature planes described in **Section 4.2** are converted to strain planes ( $\epsilon_{plane}$ ) as detailed in **Section 3.3.2**, and the vertical and transverse hypothetical free strains ( $\epsilon_{free}$ ) are plotted concurrently, the incompatibility condition which gives rise to self-equilibrating stresses can be seen. The results for both the vertical and transverse direction of the solid T-beam are shown in **Figure 4-14**, with the strain planes shown by the shaded T-shapes and the hypothetical free strains indicated by the dashed lines, for two critical time increments.



**Figure 4-14 Hypothetical free (a) vertical and (b) transverse strains and strain planes for solid T-beam**

### 4.3.1 Vertical Thermal Strain

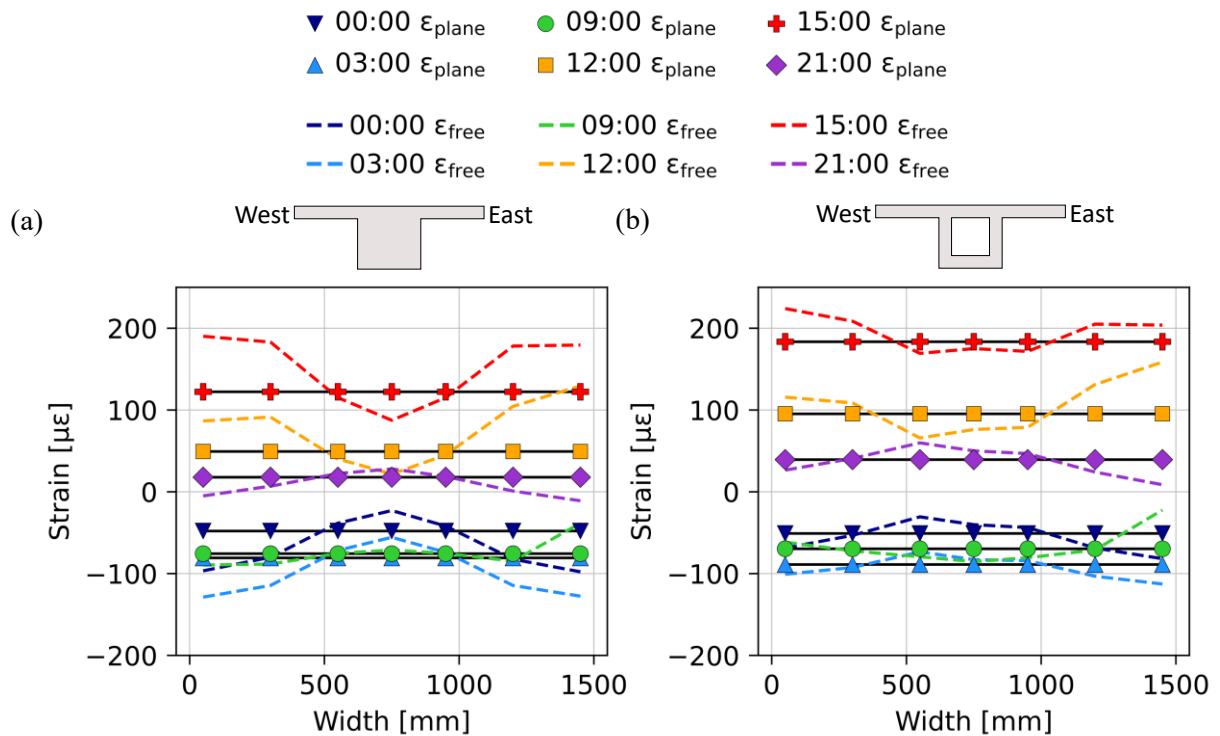
The vertical hypothetical free strains and the planar strains of both the solid and voided T-beams for the selected day detailed in **section 4.2**, are presented in **Figure 4-15**. In the interest of visual clarity, two time increments were omitted for each T-beam. The slope of the plane strain lines is directly related to the curvature induced by the temperature through the beams; steeper slopes have smaller differences from the vertical and indicate low curvature, while flat slopes have large differences from vertical and so reflect high curvature. The curvature of the two beams were similar, however, the deviation between the plane strain and the free strain was greater for the solid beam, especially in the centre and toward the top portion of the beam.



**Figure 4-15** Vertical hypothetical free and plane strain for the (a) solid and (b) voided T-beams

### 4.3.2 Transverse Thermal Strain

The transverse hypothetical free strain and plane strains caused by temperature variation for the same selected day are given in **Figure 4-16**. Since the Euler-Bernoulli beam theory is assumed to hold, the strain at a height of 450 mm in **Figure 4-15** was used as the plane strain across the width of the section in **Figure 4-16** for each section and time respectively. Because of the direct correlation of temperature to free strain, the free strain profiles directly mirror the temperatures shown in **Figure 4-13**. The difference between the plane strain and free strain for the voided section is noticeably smaller than for the solid beam, again reflecting the impact of the solid mass at the centre of the solid beam on the centre portion, while the flange portions deviate significantly from plane strains for most times of the day.



**Figure 4-16** Transverse hypothetical free and plane strain for the (a) solid and (b) voided T-beams



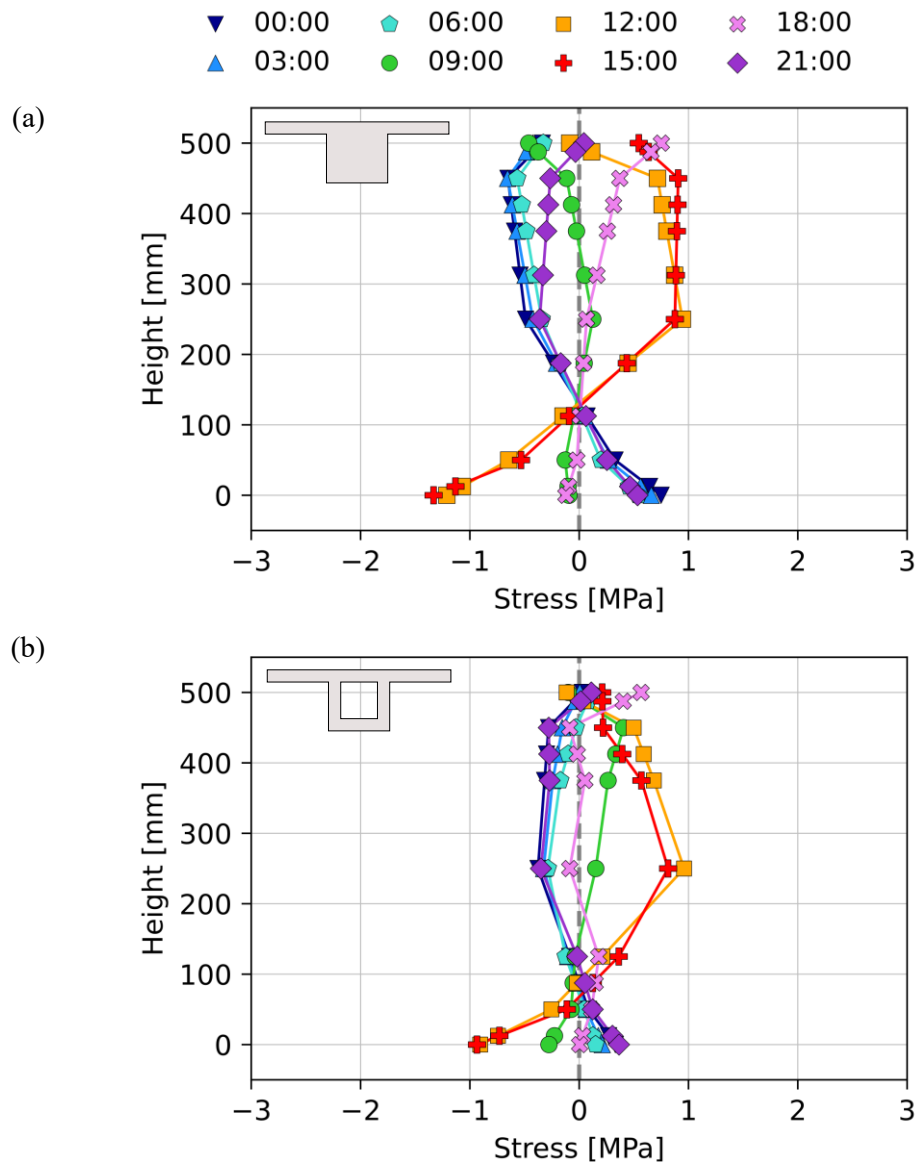
## 4.4 TYPICAL DAILY CALCULATED STRESS

The strains presented and discussed in **Section 4.3**, were used to calculate the total thermal stress profiles for fully restrained boundary conditions. Fully restrained boundary conditions results in two stress components which need to be considered in addition to the self-equilibrating stresses due to the nonlinear temperature distributions developed in the both sections, namely curvature stress ( $\sigma_{Curv}$ ) and effective temperature stress ( $\sigma_{Teff}$ ).  $\sigma_{Teff}$  develops as result of the restraint of the axial, or longitudinal, movement and  $\sigma_{Curv}$  as result of curvature restraint. The summation of all three components results in the total thermal stress profile within each section. To aid in the explanation of how the total thermal stress profiles were determined, the individual components are presented and discussed separately.

### 4.4.1 Self-equilibrating Stress

Due to the nonlinear temperature distributions, self-equilibrating stresses developed within both T-beams. The difference between the hypothetical free strains and plane strains presented in **Section 4.3**, cause such stresses and the vertical and transverse self-equilibrating stresses for the same selected day are given in **Figure 4-17** and **Figure 4-18** respectively. Tensile stresses are indicated by positive values and conversely, compressive stresses by negative values. Since concrete cracking is related to tensile strength, the tensile stresses which developed through the sections are of greater interest for this study.

In the vertical direction, the two profiles produce similar shapes, with near identical stresses at the centre of the sections. However, the solid section produced larger stresses at the top and bottom surfaces compared to the voided section. The vertical self-equilibrating stresses of box-girder sections, similar to the voided T-beam in this study, were the main focus throughout literature. The shape of the self-equilibrating stress profiles in this study are similar to those reported by Elbadry and Ghali (1986). Elbadry and Ghali (1986) however had a much larger section 2.74 m deep and recorded self-equilibrating tensile stresses of approximately 2.5 MPa in the beam's centre, which suggests deeper section may develop greater self-equilibrating stresses. In the current study, both cross-section's self-equilibrating stresses remained below the tensile strength of the concrete measured at just over 3 MPa at the time under consideration. Therefore, the vertical self-equilibrating stresses would not constitute cracking within either of these sections.



**Figure 4-17 Vertical self-equilibrating stress for the (a) solid and (b) voided T-beams**

In the transverse direction, the self-equilibrating stresses also remained below the concrete tensile strength and the largest stresses observed were compressive stresses in the flanges of the solid section. Even though the largest stresses were compressive, there was a significant difference in stress between the centre and the flanges of the solid beam for the warmest and coldest times of the day. Contrastingly, the stresses in the transverse direction were more uniform across the width of the voided section.

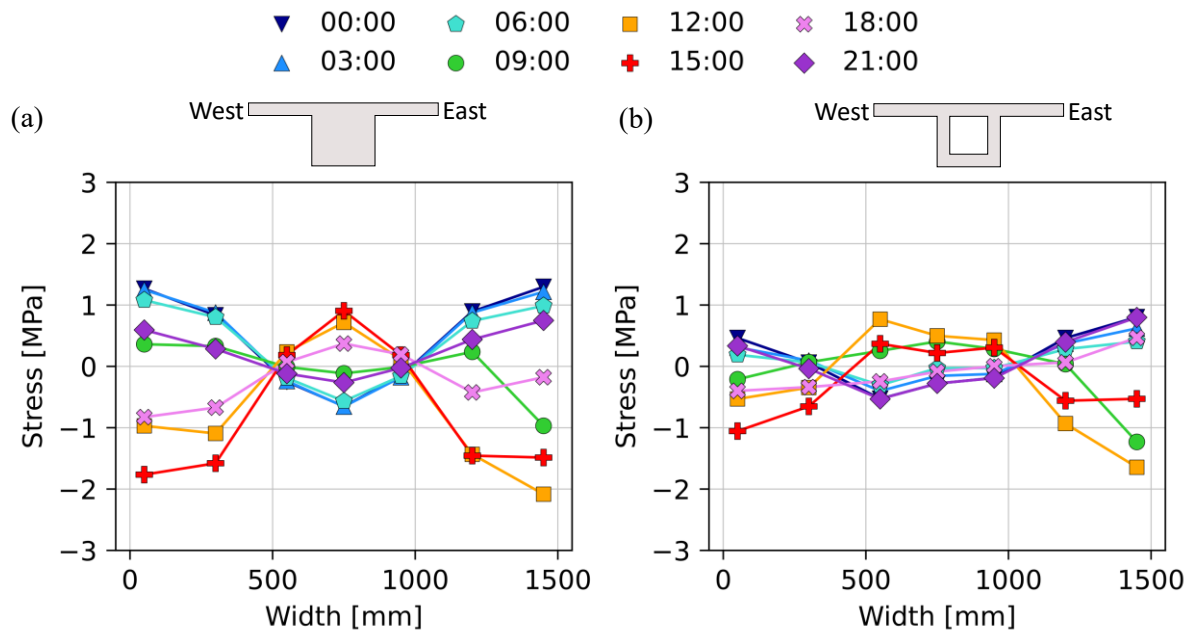
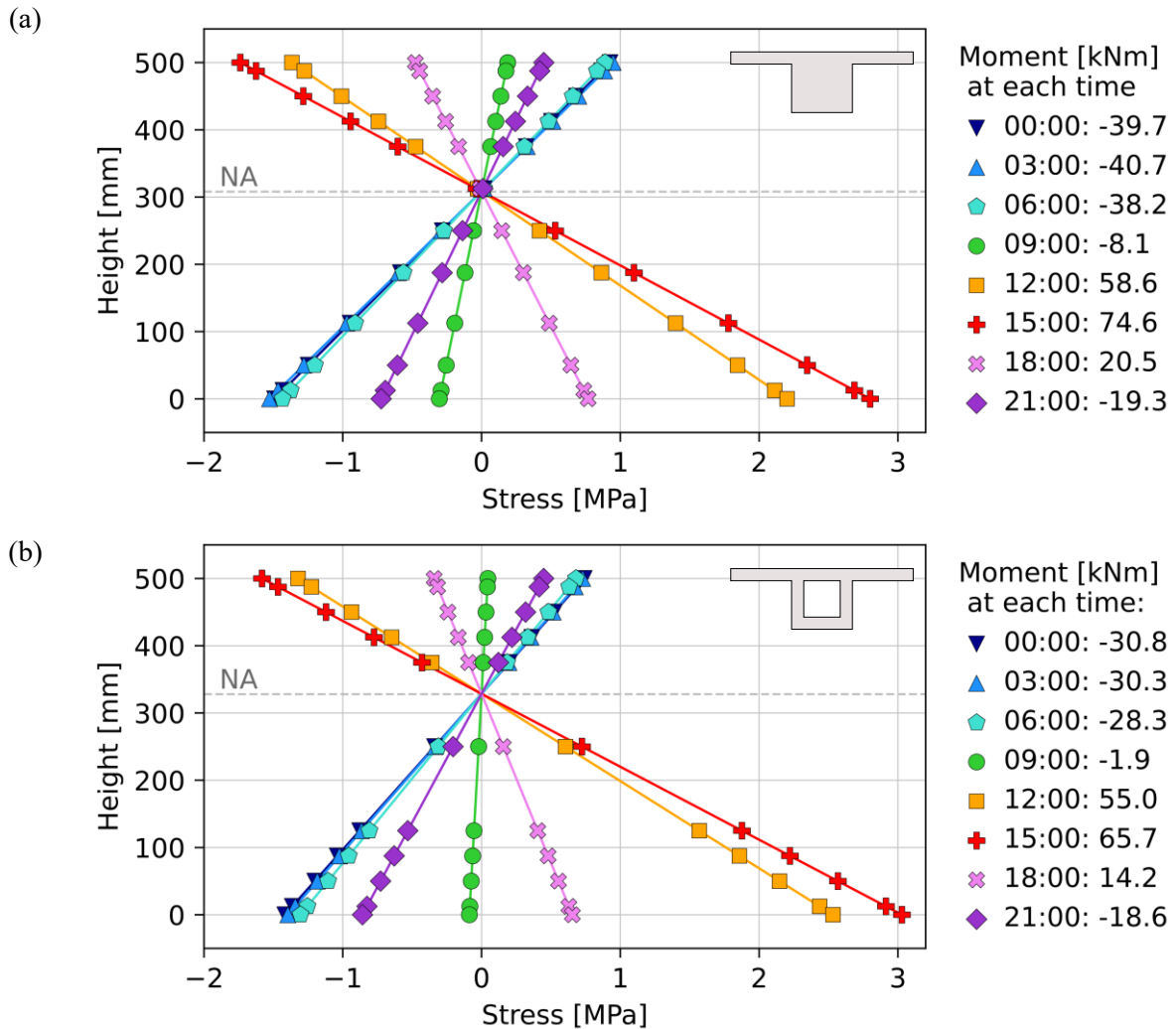


Figure 4-18 Transverse self-equilibrating stress for the (a) solid and (b) voided T-beams

#### 4.4.2 Curvature Stress and Secondary Thermal Moments

Self-equilibrating stresses develop as necessary to maintain equilibrium within a section regardless of the restraint conditions imposed on a member. However additional stress will develop if axial movement and deflections are prevented by applied boundary conditions. Most commonly curvature will be prevented in structures due to continuity and the presence of internal supports. **Figure 4-19** shows the stresses induced within both sections as result of curvature restraint, along with the associated secondary thermal moments which develop at each time through the selected day. Negative secondary thermal moment represent hogging as tension develops at the top of the beam, while positive secondary thermal moments represent sagging, with compression stresses created at the top of the beam. Little difference is seen between the curvature stresses generated for the different cross-sections; however, the secondary thermal moments exhibit considerable differences for most times of the day. The difference in moment arises from the distinct second moment of area ( $I$ ) values of the cross-sections, as other properties influencing the moments either remain identical or differ by a negligible amount. The curvature stress developed across each section's width in the transverse direction are the stress values at heights of 450 mm in each beam as was the case for the strains described earlier (**Figure 4-20**).



**Figure 4-19 Curvature stress and moment for the (a) solid and (b) voided restrained T-beams**

For structures which allow axial, or longitudinal, movement, the total vertical thermal stress created within a section would be the summation of the self-equilibrating stress in **Figure 4-17** and **Figure 4-19**. Likewise, the total transverse thermal stresses are the summation of stresses in **Figure 4-18** and **Figure 4-20**. The combination of the curvature and self-equilibrating stresses counteract one another in the topmost and bottommost parts of both T-beams where the largest curvature stresses are developed. At the centroid of both T-beams, the curvature stresses are minimal, but the self-equilibrating stresses are at their peak. It should be noted that the moments and curvature that develop within a member are dependent on the structural configuration, that is the position of the member and number of spans surrounding the member. For the assumptions made in the calculations detailed in **Section 3.3.2**, the curvature stresses would be more applicable to the centre spans of multi-span, continuous structures, than single span configurations. For the assumed configuration, these combinations of curvature and self-equilibrating stresses do not create conditions for the tensile strength of the concrete to be exceeded and therefore would not constitute cracking in either section. More

importantly, neither section could be considered to have lower or higher cracking potential, given the similarity in the developed stresses.

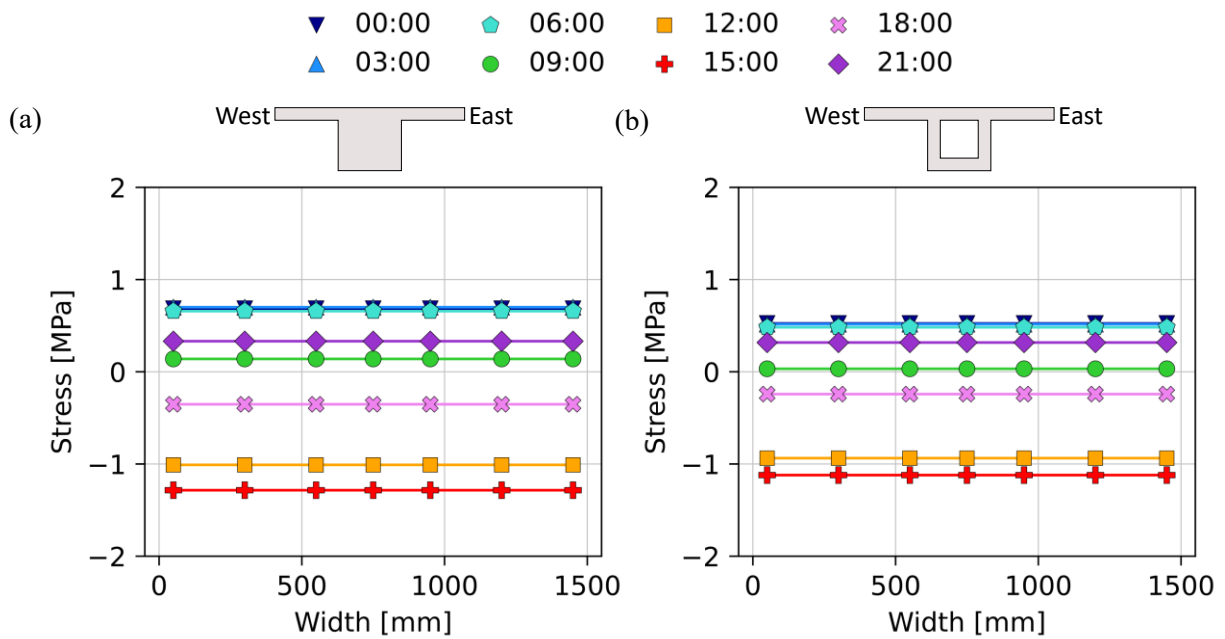


Figure 4-20 Curvature stress in transverse direction for the (a) solid and (b) voided restrained T-beams

#### 4.4.3 Effective Temperature Stress

For this study, the stresses which develop due to complete restraint of axial movement and curvature caused by environmental loading are the primary focus. Therefore, to calculate the total thermal stress in each cross-section, the stresses caused by longitudinal restraint (referred to as effective stresses) need to be considered and added to the self-equilibrating and curvature already presented and discussed. Unlike the curvature and self-equilibrating stresses caused by temperature changes, the effective stress is taken as constant across the entire cross-section. Therefore, the vertical and transverse effective stresses are equal. The effective stresses caused by temperature difference relative to the datum for each section and time are shown in **Figure 4-21**. Because the effective stress created by temperature change is directly related to the effective temperature for each section, it stands to reason that the voided section has a larger range of effective stresses. Furthermore, neither cross-section's effective stress surpasses the tensile strength ( $f_{ct}$ ) denoted by the red dashed line. Even though the primary focus was on full restraint conditions, it can be noted that in the absence of curvature restraint the total thermal stresses would be the sum of the self-equilibrating and effective stresses. With this combination, the tensile strength of the concrete was also not exceeded. It should be noted that the effective stresses are heavily affected by the selected datum temperature  $T_0$  because the change in effective temperature is in relation to  $T_0$ . The implication being, that if a higher datum temperature were selected, the drop in temperatures

would create greater tensile strengths, which could exceed the tensile strength of the concrete. Similarly, a lower  $T_0$  temperature would shift the effective stress values to the negative, or compressive, side.

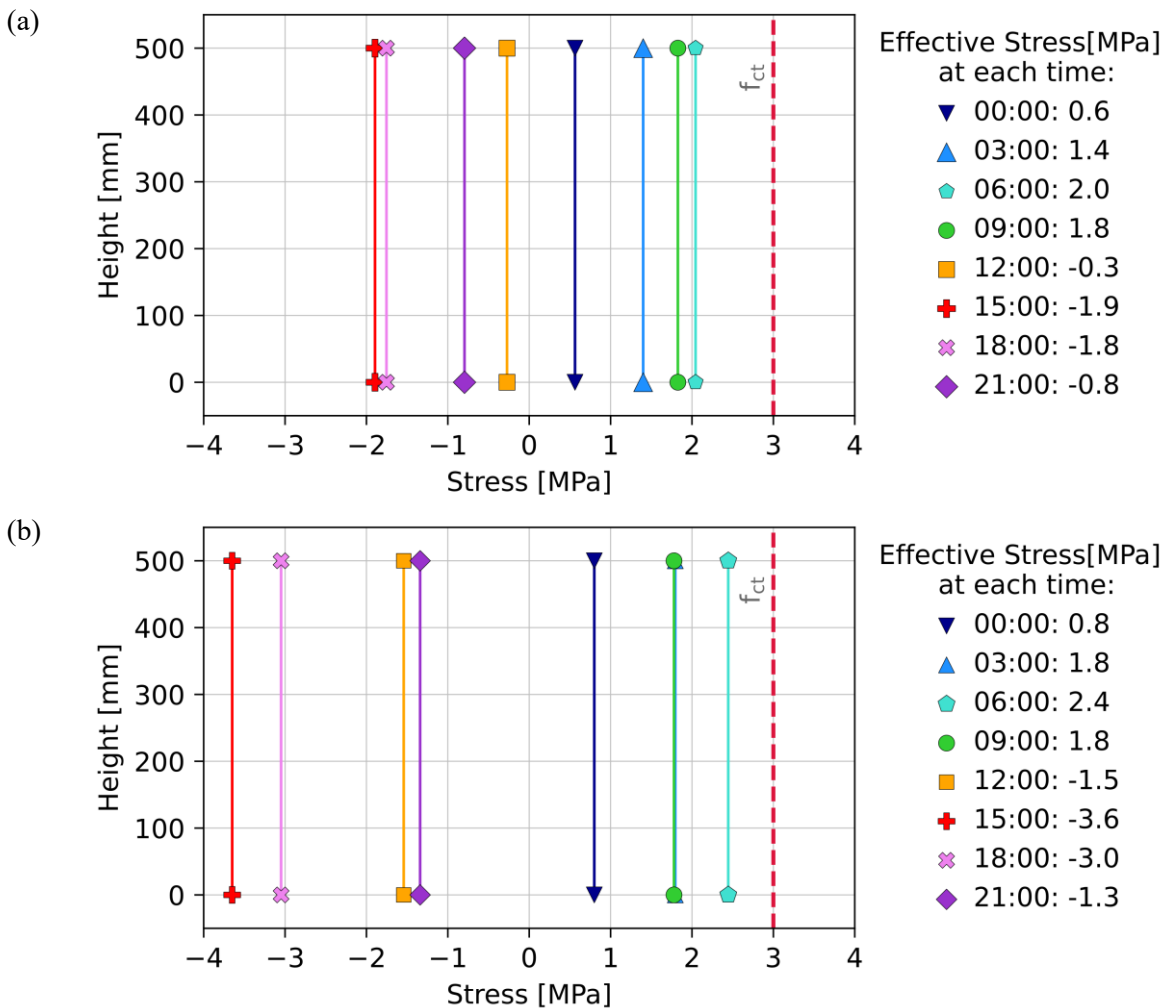


Figure 4-21 Effective temperature stress for the (a) solid and (b) voided restrained T-beams

#### 4.4.4 Total Thermal Stress

The summation of self-equilibrating, curvature and effective stress, equalling the total thermal stresses for fully restrained conditions, in the vertical and transverse directions are given in **Figure 4-22** and **Figure 4-23**. At the warmest time of the day, the total thermal compressive stress experienced by the voided T-beam exceeds that of the solid T-beam in both vertical and transverse directions. Similar tensile stress profiles were generated in the vertical direction at the colder times for the different T-beams but the voided section had slightly larger tensile stresses which marginally exceeded the tensile strength at the top of the section. Conversely, in the transverse direction, it was the solid beam's flanges which developed greater tensile stresses, which surpassed the concrete tensile strength.

COMPARING SOLID AND VOIDED T-BEAM CROSS SECTIONS

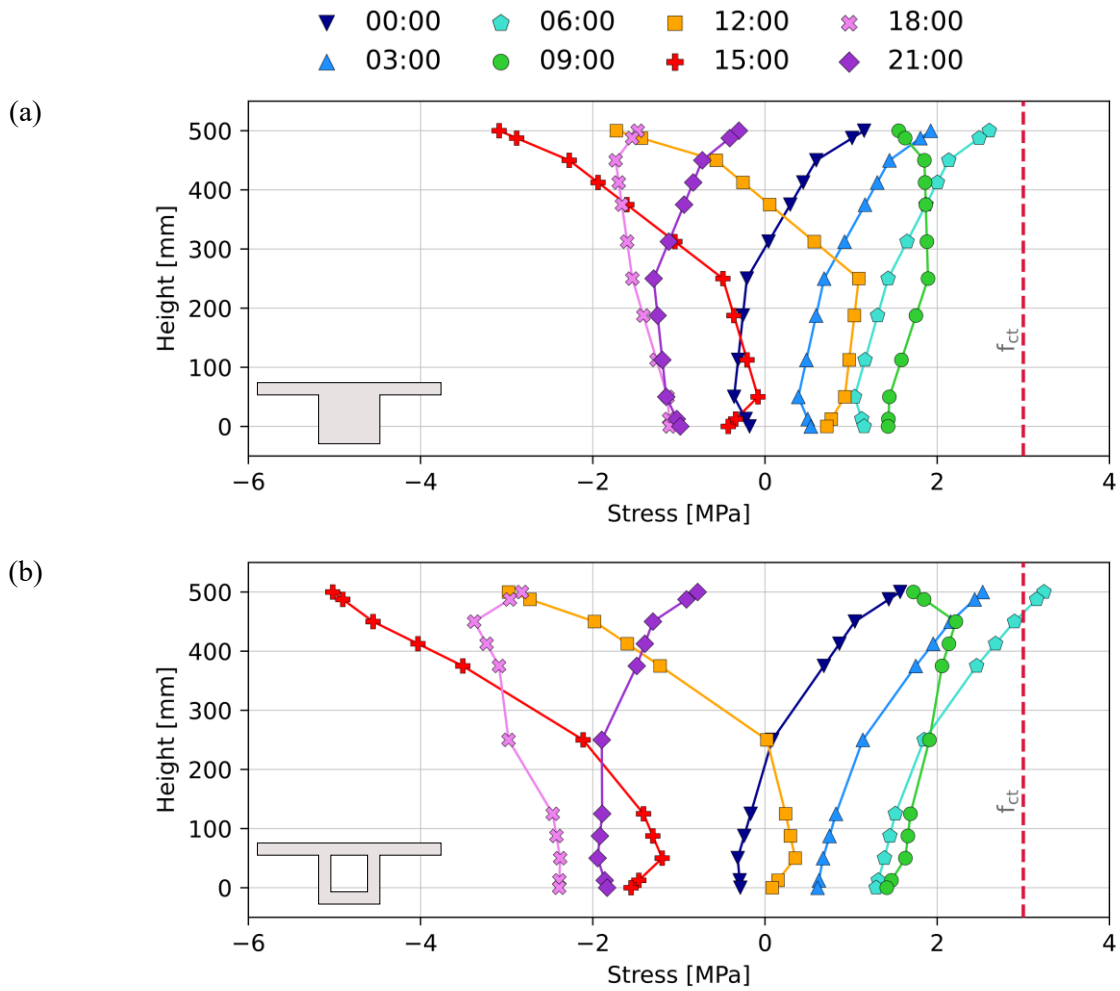


Figure 4-22 Total vertical thermal stress for the (a) solid and (b) voided restrained T-beams

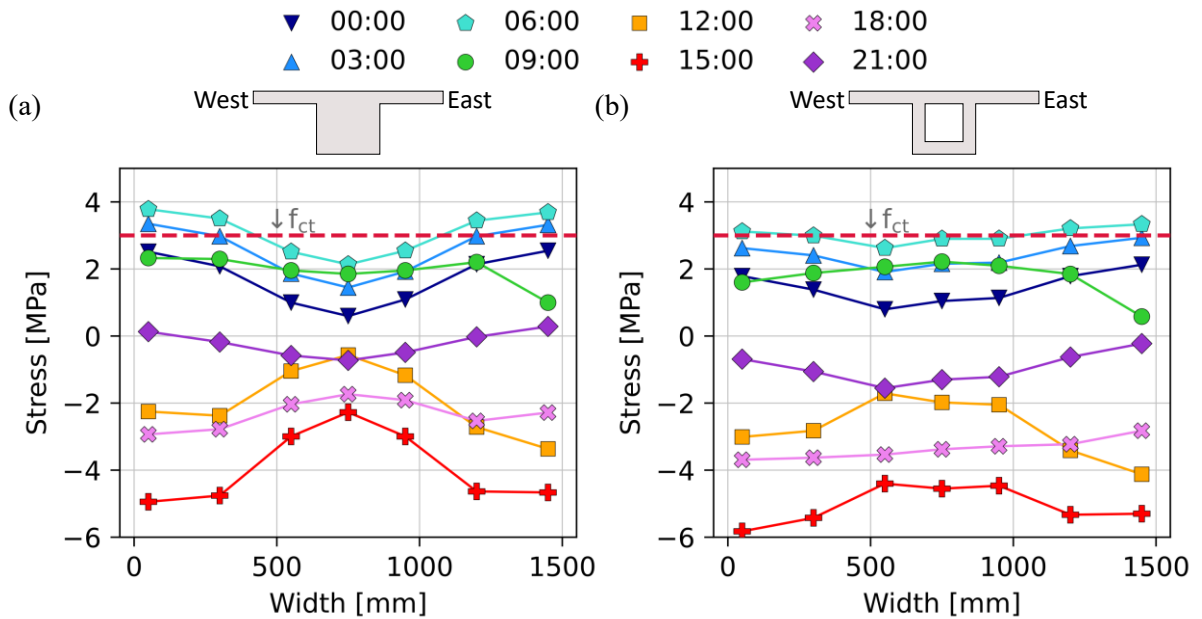


Figure 4-23 Total transverse thermal stress for the (a) solid and (b) voided restrained T-beams

## 4.5 MEASURED STRAINS

Since the strains and resulting stresses presented in **Section 4.2** were calculated based on temperature measurements using assumptions and mathematical theory, there was a need to verify the validity of the results. In order to confirm whether the strains produced via calculation were accurate, they were compared to the measurements recorded by the VWSGs on the centreline of each T-beam. To ensure the appropriate measured strains were compared, the shrinkage strains were removed from the gauges used in the comparison. Self-equilibrating stresses do not produce measurable strains, therefore the calculated strains used in the verification were the combination of the strains which produced the curvature and effective stresses. These are the same strains as the plane strains ( $\epsilon_{plane}$ ) given in **Figure 4-15**. The described measured and calculated strains are shown in **Figure 4-24** for the same selected day used throughout **Section 4.2**. For the voided T-beam, the calculated strains matched the measured values for the included warmest (15:00) and coldest (06:00) times well, although some variation occurred between these times. The times for which the highest compressive and tensile stresses are produced are the focus and concern in terms of cracking and therefore the calculated strains for the voided section are considered representative of the measured strains. In the case of the solid beam, the strains calculated for coldest time (06:00) matched the measured strains well but overestimated the curvature at other times. One of the assumptions used in the calculations is that the T-beams remained uncracked, therefore all areas were used to calculate effective temperatures and strain planes. However, if cracking was present within the solid section, as suggested by the shrinkage strain presented in **Section 4.1.3**, the contribution of the flange temperature changes to strains would be reduced. Therefore, the deviation between calculated and measured strains supports the theory that cracking occurred between the central solid portion and the flanges of the solid T-beam. **Figure 4-25** shows the difference between the calculated and measured strains for the positions 50 mm and 450 mm above the soffit for both T-beams over the duration of the study. The trends seen and discussed in **Figure 4-24** can also be seen in **Figure 4-25**, where the difference between daily calculated and measured strain remained constant for much of the observed period. For both beams the difference between the measured and calculated strain was less for the bottom of the beam than for the top. The calculated strains for the voided T-beam are more representative of the measured strains than that calculated for the solid T-beam. The only major anomaly within the strain differences for both T-beams was at the very beginning of the observed period. The strains were calculated from the point of final set onwards and the prominent peaks seen at a height of 450 mm were as result of the heat of hydration of the cement which continued after final set. The strains calculated in this chapter mostly show the behaviour of the T-beams over 24 hours but the long-term effects of drying shrinkage and temperature change from setting must be taken into account.



COMPARING SOLID AND VOIDED T-BEAM CROSS SECTIONS

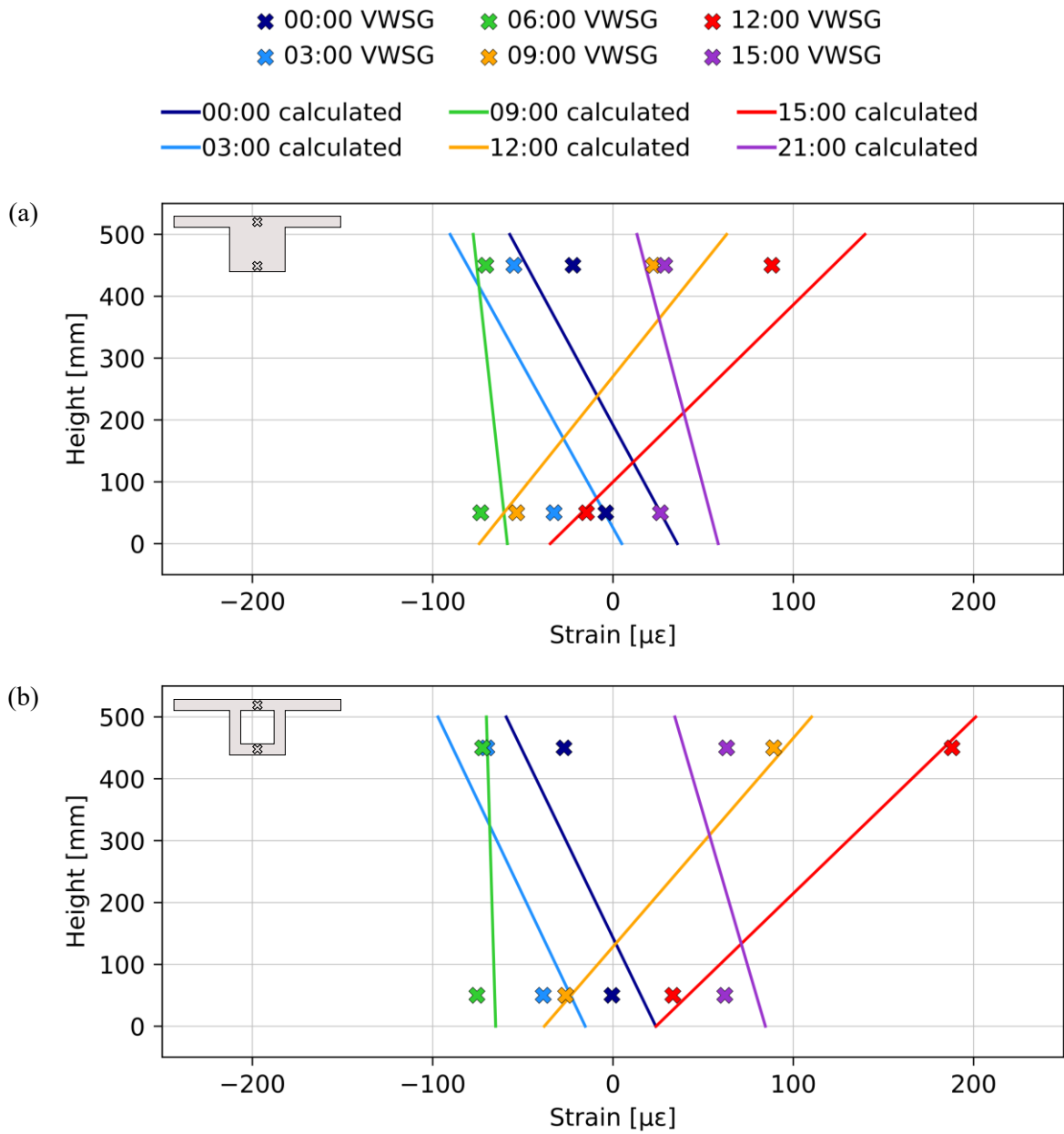


Figure 4-24 Measured and calculated strains for the (a) solid and (b) voided T-beams

COMPARING SOLID AND VOIDED T-BEAM CROSS SECTIONS

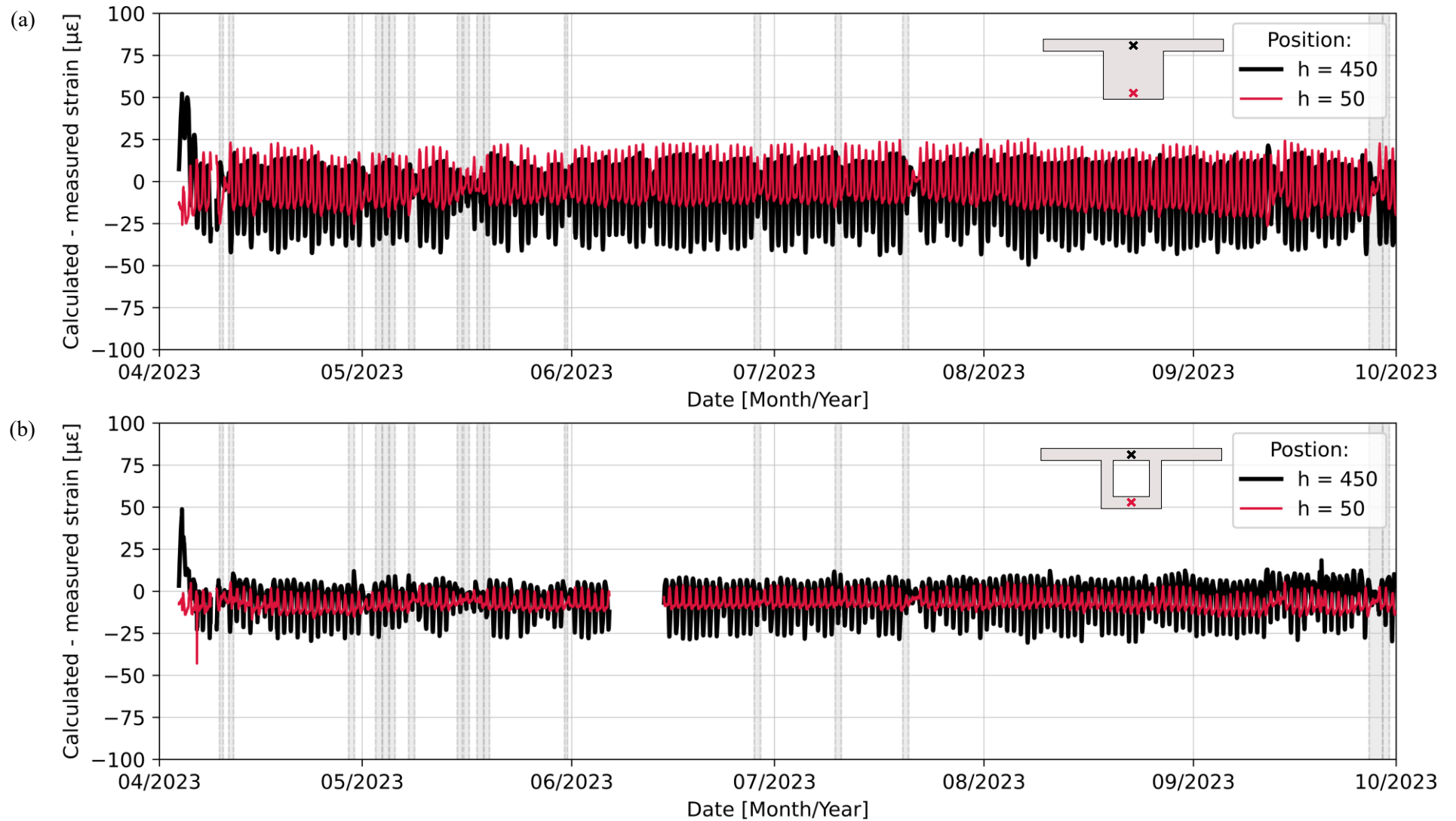


Figure 4-25 Measured and calculated strain difference for the (a) solid and (b) voided T-beams

## 4.6 SUMMARY OF RESULTS

In this section the response of the solid and voided cross-sections to typical thermal environmental loads were compared. This section summarises the findings according to measured temperature, measured strain and calculated stress results.

### 4.6.1 Measured Temperature

The thermocouples positioned throughout the cross sections of the T-beams were used in conjunction with the thermistors within the VWSGs to calculate the weighted average, or effective temperatures and temperature distributions of both cross sections. The following observations could be made regarding the measured temperature results:

- As a result of its lower thermal inertia, the voided T-beam was more sensitive to environmental temperature and therefore showed greater daily effective temperature ranges compared to the solid beam.
- Both T-beams developed nonlinear temperature distributions in the vertical direction. The transverse temperature distribution for the solid beam was also nonlinear but the voided beam developed more uniform temperatures across the width of the top portion of the beam.
- TMH7:1981 provided satisfactory vertical temperature distribution guidelines for the selected cross sections. This highlights the potential for TMH7:1981 to be used in the design of typical beam elements to take temperature effects into account. However, guidelines for the transverse direction are lacking and should be considered for a solid section.

### 4.6.2 Measured Strain

The T-beams analysed in this study were cast with the specific intension to allow free movement caused by the environment so that strain measurements could be recorded. The strain measurements yielded the following findings:

- The total strain measurements captured by the VWSGs showed increasingly negative trends, indicating an increased shortening, caused by the drying shrinkage experienced by the beams.
- The difference in shrinkage between the web and the flange of the solid T-beam was significant due to the difference in thickness between the two segments. The uniform thickness of the voided section caused more uniform shrinkage of the web and flange segments of the beam.
- Furthermore, both cross-sections experienced differential shrinkage between the top and bottom portions of the T-beams over time.
- TMH7:1989 provided a poor prediction of the effective shrinkage strain for the voided T-beam over time despite taking the effective thickness of either cross-section into account. It

underestimated the drying shrinkage of the voided beam after 6 months by 100  $\mu\epsilon$ . TMH7:1989 produced a better prediction for the solid T-beam with an underprediction of 30  $\mu\epsilon$  after 6-months. However, the early age shrinkage prediction provided by TMH7:1989 for both beams was poor.

- The calculated strains due to temperature were compared to the measured thermal strains in both T-beams. Although the calculated strains for the voided section showed better correlation with the measured strains than the solid section, both were considered acceptable. Therefore, the calculated stresses were considered representative of the response of the beams to temperature.

### 4.6.3 Calculated Stress

Strains throughout the T-beam caused by the thermal loading on a typical day were calculated based on mathematical models and so different stress components could be calculated for applicable boundary conditions. Therefore, the calculated stresses could be compared to the tensile strength of the concrete to evaluate the potential of cracking caused by typical temperature loading. The following conclusions for individual stress components and their summation caused by the thermal loading of a typical day can be reached:

- The self-equilibrating stresses are the only component independent of boundary conditions but were the smallest individual stress component in both T-beams, remaining below 1 MPa in tension.
- For nonlinear temperature distributions, self-equilibrating stresses are present and for curvature restraint, curvature stresses will develop in addition to the self-equilibrating stress. Therefore, the combination of the two must be considered when compared to the tensile capacity of concrete to quantify the possibility of cracking when longitudinal movement is allowed. Since the self-equilibrating stresses counteract the tensile stresses produced at the top and bottom extremes of the beam, it is unlikely that critical tensile stresses would develop based on the imposed thermal loading for the selected day. According to Elbadry and Ghali (1986), self-equilibrating stresses can produce higher stresses in deep sections while continuity stresses decrease. Therefore, further investigation would be required to determine how this combination of stresses changes with varied cross-sectional depths.
- For the selected datum temperature, neither the effective stress, nor the combination of effective and self-equilibrating stresses surpassed the tensile capacity of the concrete. This would be the applicable combination when axial movement is permitted but curvature prevented. As such, the combination of all three stress components ( $\sigma_{Self-eq}$ ,  $\sigma_{Curv}$  and  $\sigma_{Teff}$ ) result in the highest tensile stresses, increasing the likelihood of transverse cracking. The largest tensile stresses

developed at the top of the voided section, as such additional steel reinforcement should be considered to limit the development of cracks in the region. Furthermore, the critical stresses were developed due to fully restrained boundary conditions.

- The sizable difference in thickness between the flanges and the central segment of the solid T-beam, created large stress differentials between the two portions. The difference in stress should be considered in design to minimise the probability of cracking at the transition in thickness.

In this chapter the comparative behaviour of the two cross-sections in response to temperature over the study period along with the stresses developed for a typical day, were mainly presented. The long-term effects of shrinkage on stress development and the risking of cracking due to heat of hydration after final set were not considered in this chapter. However, these effects must be taken into account along with the time of restraint to determine the full extent of tensile stress development of the concrete T-beams through their life spans.

## 5 FACTORS INCREASING TENSILE STRESS

### 5.1 INTRODUCTION

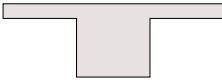
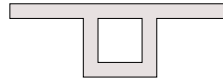
**Chapter 4** compared the response of the T-beams with different cross-sections to environmental thermal loading and presented the stresses developed in the fully restrained sections due to thermal loading of a typical day. The results presented in **Chapter 4** did not yield conclusive evidence that either cross-section would crack transversely under environmental thermal loading applied on a typical day. Further investigation into the behaviour of both beams over the full period of observation is required to identify the key parameters and conditions which could be responsible for critical tensile stresses development. This chapter provides insight into the combined effects of temperature, particularly concrete heat of hydration, and shrinkage over time on the stresses generated within the two different T-beams.

### 5.2 TEMPERATURE CAUSED BY HEAT OF HYDRATION

Neither T-beam cast and observed in this study would typically be large enough to be considered as mass concrete. However, considering the high effective temperatures produced during and after final set, along with the V/A ratio of each beam, the stresses developed within the beams were investigated. The concrete mix used is not considered a high-strength mix. It contained significant amounts of pozzolan and filler material, which are known to reduce the heat of hydration. Moreover, casting started when the outside temperature was 25 °C which increased to 26 °C (the maximum for the day) when casting was completed. The windspeed was low while casting took place and the beams were adequately covered with curing blankets shortly after casting was completed. Therefore, the full casting process was completed in good conditions which should not adversely influence results.

In **Section 4.2** the datum temperature  $T_0$  was selected at a time where the effective temperatures of the cross-sections were similar and uniform. However, the effective temperatures at the selected datum were below 15 °C and so the full temperature history of the members were not considered. **Table 5-1** gives the effective temperatures at final set and maximum effective temperatures produced due to cement hydration after final set.

**Table 5-1 Effective temperatures related to heat of hydration**

|   |  |  |
|---|--|---|
| Effective temperature at Set ( $T_{effset}$ )<br>03/04/2023: 21:15  | 36.2 °C  | 34.7 °C   |
| Maximum effective temperature due to<br>heat of hydration after set | 48.9 °C<br>(04/04/2023: 15:30)   | 46.5 °C<br>(04/04/2023: 14:00)  |

Clearly, the maximum heat of hydration temperatures were greater than any caused by daily thermal loading. Considering the presence of restraint, either from the member itself or externally, the thermal shrinkage which occurs with the heat dissipation, will produce tensile stresses. Therefore, the decrease in effective temperature and differential temperature decrease between different segments of the T-beams are important. The maximum effective temperature for both sections exceeded 45 °C and were recorded approximately 24 hours after casting, after which the sections started to cool down and follow the expected daily thermal cycles.

The temperature distributions for both cross-sections from the time that the beams started to cool down after reaching maximum effective temperature up to the time the environmental conditions started to heat the beams for the first time the following morning are displayed in **Figure 5-1** and **Figure 5-2**. In this section, the datum temperatures were taken as  $T_{effset}$  (displayed on the left side) and the effective temperature ( $T_{eff}$ ) of each time increment are displayed on the right. As expected, the maximum effective temperature of the solid beam was higher because of the solid central mass that produced and retained the hydration heat more than the thin sections surrounding the void of the voided beam. The effective temperature of the voided T-beam decreased more rapidly than the solid T-beam, but the insulated void also efficiently maintained its temperature as the surrounding concrete remained marginally warmer than the flanges, despite the segments having the same thickness. As the solid beam cooled down, a significant difference of more than 5 °C developed between the top centre point and the flange. The voided beam also developed differences between the top centre point and the flange but to a much smaller extent.

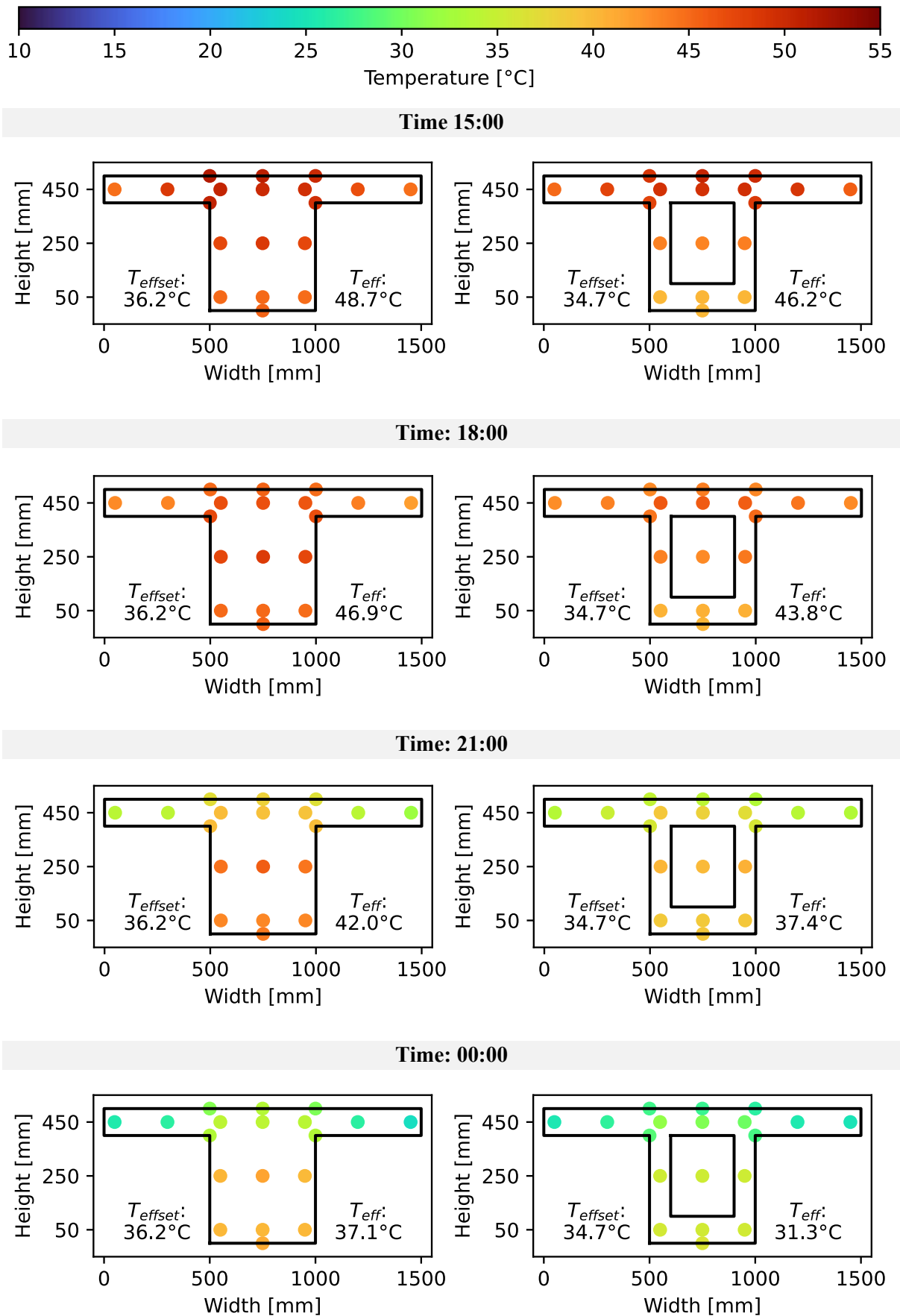


Figure 5-1 Temperature distributions from 15:00 04/04/2023 to 00:00 05/04/2023



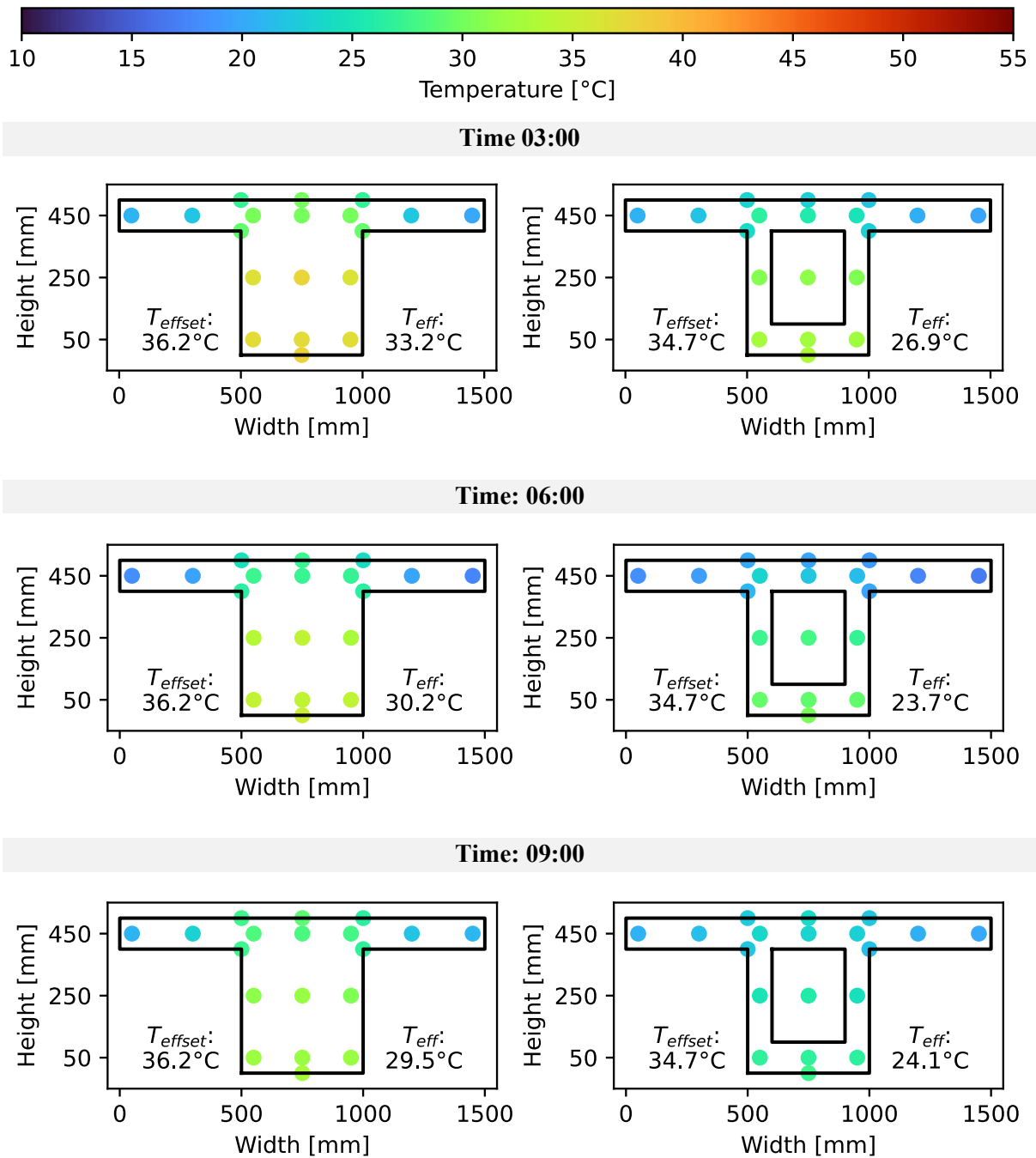
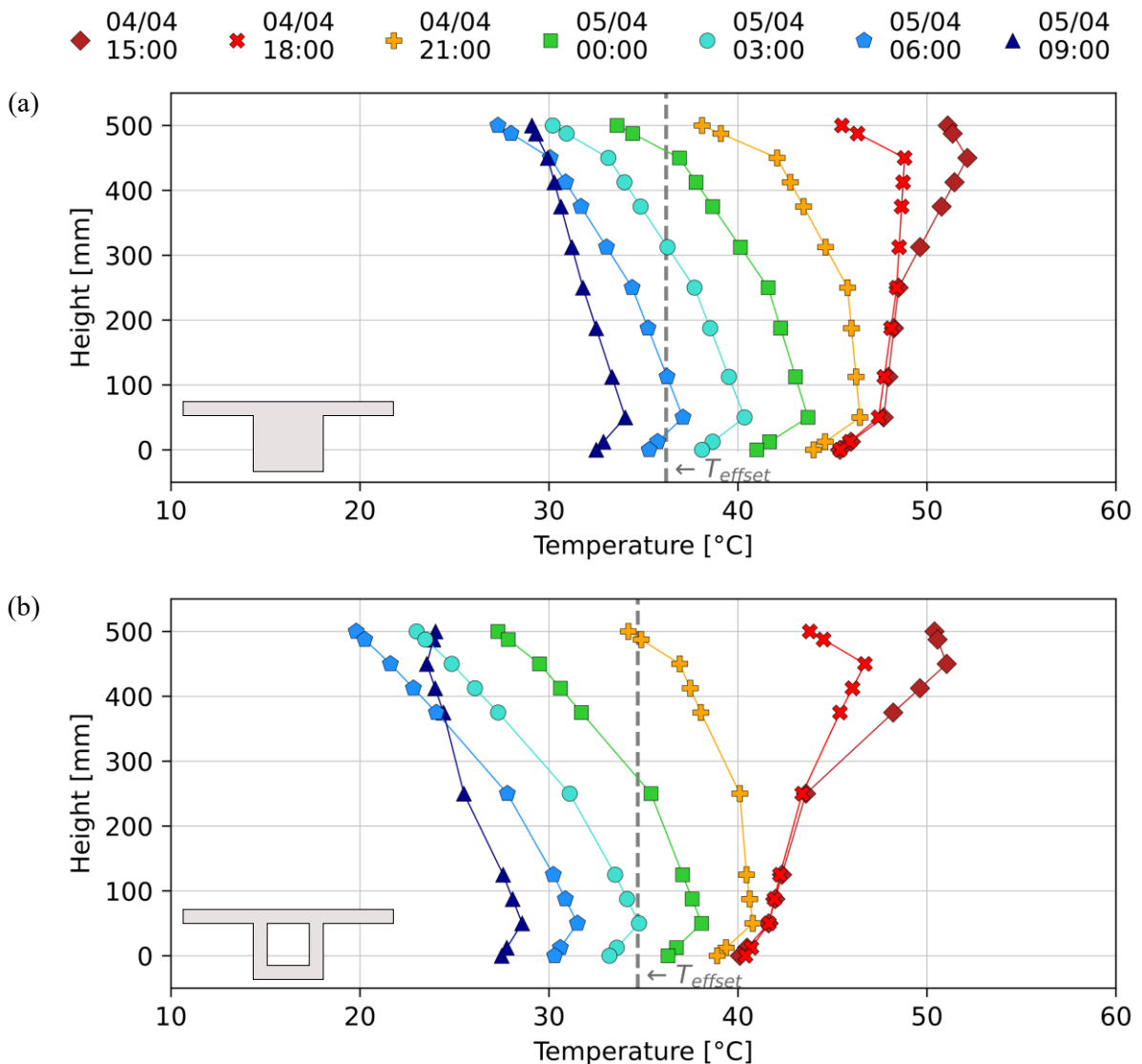


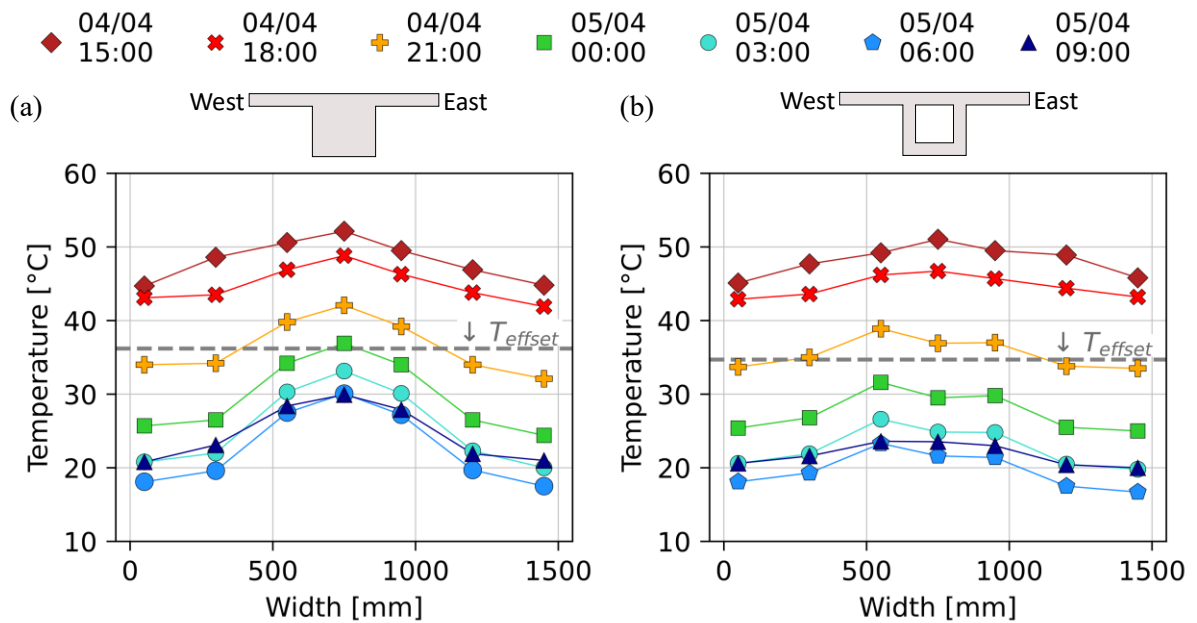
Figure 5-2 Temperature distributions from 03:00 to 09:00 on 05/04/2023

The vertical temperature distributions for the same time increments included in **Figure 5-1** and **Figure 5-2** are displayed in **Figure 5-3**. From this it can be seen that the solid beam reached higher temperatures, particularly at the vertical centre and that the top portion cooled down faster than the bottom. By 09:00 on 05/04/2023 the influence of the sunrise on the top portion can be seen as it regains heat. This was the time where the daily thermal cycles were considered to begin. For the voided T-beam, a similar trend could be seen but at a more rapid rate. The maximum difference between the centre and top and bottom surfaces for both beams was 8 °C, which is within the range of 19 °C given in ACI SPEC- 301-20 (2020).



**Figure 5-3 Vertical heat of hydration temperature distributions for the (a) solid and (b) voided T-beams on 04/04/2023 to 05/04/2023**

For the same time increments as included for the vertical temperature distribution, the transverse direction was plotted and is displayed in **Figure 5-4**. The temperature of the void is seen to keep the centre marginally warmer than the flanges as the heat dissipation continued but by the time the temperature began to increase due to the sunrise, very constant temperatures were recorded across the width of the section. For the solid beam, a significant difference between the centre and the flange sections was seen to develop as the T-beam cooled down. A difference of 5 °C was present between the centre segment of the flange and the top centre point of the beam at 18:00 on 04/04/2023 which increased to a difference of 11 °C by 00:00 05/04/2023. Given that the centre point in the transverse direction is at a height of 450 mm and a further 5 °C difference between it and the centroid, a difference of 16 °C was exhibited between the centroid and the flanges of the solid beam, approximately 33 hours after the beam was cast.



**Figure 5-4 Transverse heat of hydration temperature distributions for the (a) solid and (b) voided T-beams on 04/04/2023 to 05/04/2023**

### 5.3 TOTAL STRESS CAUSED BY HEAT OF HYDRATION

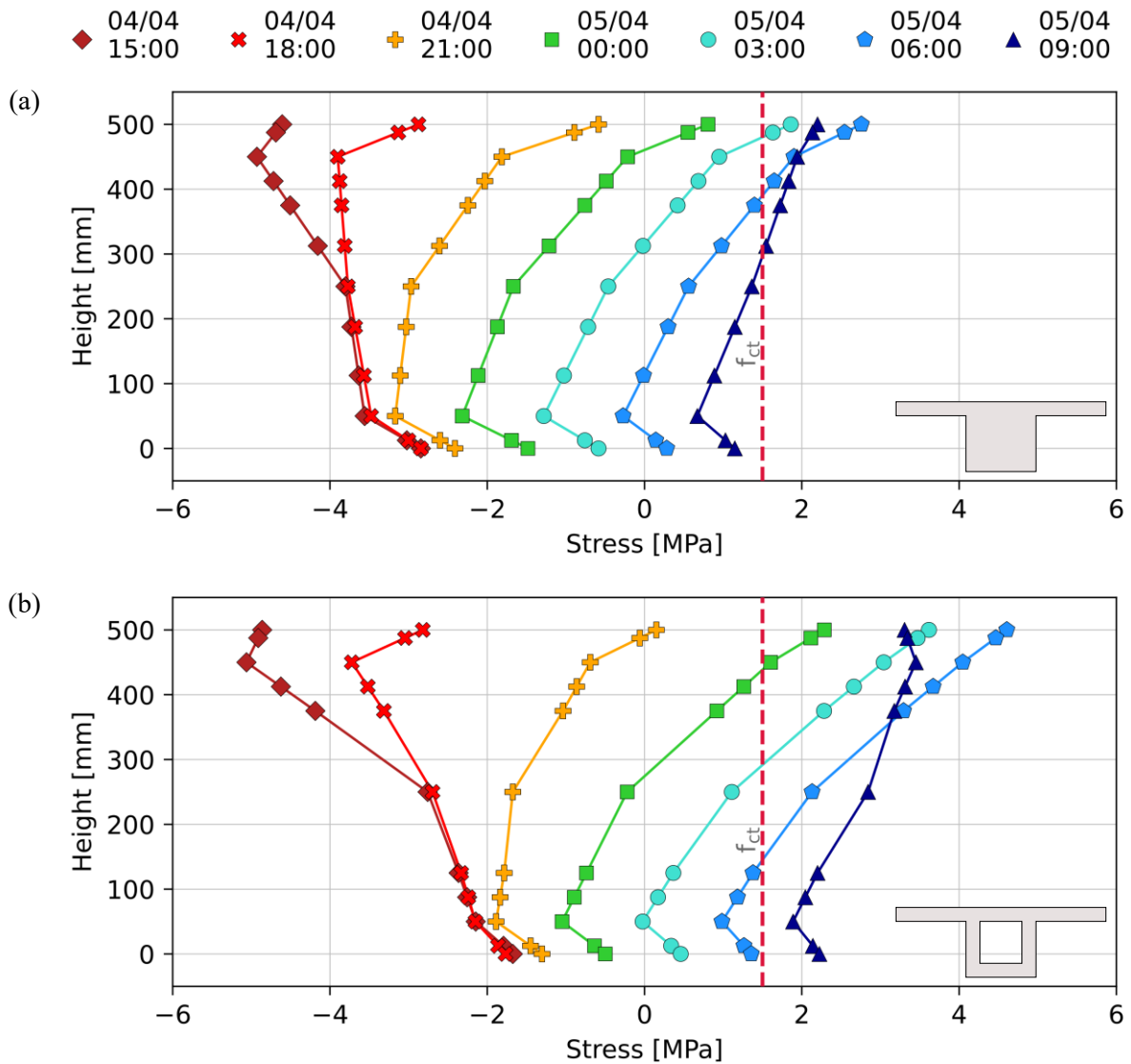
If the section is assumed restrained from final set, the increase in temperature from cement hydration after set would produce compressive stresses throughout both sections. However, after the heat of hydration dissipates and the effective temperatures decrease to below the effective temperatures at set, tensile stresses are produced in the section. The average effective temperature ( $T_{effavg}$ ) for the duration of the study for both T-beams was calculated to be 19.8 °C, which is lower than the respective effective temperatures at set ( $T_{effset}$ ), the beams would predominantly experience tensile stresses due to the net thermal shrinkage. The temperature differentials developed through the depth and width of the sections would also create stress differences within the section.

Using the effective temperature at set ( $T_{effset}$ ) as the datum temperature, the same calculation process detailed in **Section 3.3.2** and presented in **Section 4.4** was used to calculate the total thermal stresses in the vertical and transverse directions as presented in **Section 5.3.1** and **Section 5.3.2** respectively. The assumption of full restraint of curvature and longitudinal movement was maintained and the self-equilibrating stresses due to nonlinear temperature distributions were also considered. The tensile strength of the concrete ( $f_{ct}$ ), was read from **Figure 3-28** as 1.5 MPa for the time between 1- and 2-days after casting, which was considered to be the most suitable value for the range of time intervals displayed.

In this experiment only one concrete mix with unique material properties was evaluated. Therefore, the sensitivity of restrained stresses to individual material properties would be required to determine recommended properties to minimise tensile stresses within any cross-section.

#### 5.3.1 Vertical Stress Distribution caused by Heat of Hydration

The vertical total thermal stress distributions for both the solid and voided T-beams are shown in **Figure 5-5**. For the solid T-beam, the tensile stress at the top portion exceeds the tensile strength of the concrete from approximately 03:00 on 05/04/2023 onwards. With the low tensile strength applicable for the early age concrete, the stresses developed exceeded the tensile strength of the concrete along the top surface of the beam. However, tensile stress in lower half of the solid beam remained below the tensile strength. In the case of the voided beam, the top portion also exceeded the tensile strength from 00:00 on 05/04/2023 - sooner than the solid beam. In addition, as time progressed, the stress through the entire depth of the voided section surpassed the tensile strength which would constitute major transverse cracks for restrained conditions throughout the depth of the voided T-beam.



**Figure 5-5 Vertical total thermal stress for the (a) solid and (b) voided restrained T-beams on 04/04/2023 to 05/04/2023**

Based on the fully restrained stress analysis between the two cross sections, the voided section is more likely to develop longitudinal tensile stress caused by thermal shrinkage after the heat of hydration dissipates, which exceeds the tensile stress capacity of the concrete. It is interesting to note that even though the solid T-beam had a higher effective temperature at set caused by its higher thermal inertia, the tensile stresses developed through the voided T-beam as the heat of hydration dissipated, were greater than for the solid section. Furthermore, the vertical stress distributions caused by heat of hydration were far greater than those caused by a temperature variation of a typical day.

Considering that the stresses developed due to heat of hydration in small, scaled beams could easily exceed the tensile strength of the concrete soon after set, coupled with the fact that larger bridge cross sections would develop greater effective temperatures because of cement hydration, stresses caused by

the restraint of concrete elements after concrete set should be considered in the design of any structural concrete element.

### 5.3.2 Transverse Stress Distribution caused by Heat of Hydration

The transverse total thermal stress distributions for both the solid and voided T-beams are shown in **Figure 5-6**. The solid beam's flanges developed stresses greater than 4 MPa, exceeding both the early age and mature concrete tensile strength. Not only were high tensile stresses produced, the stress differential between the centre and the flange regions were also sufficient to cause cracks between the web and flange sections in the unrestrained beam as can be seen in **Figure 5-7**. In this experiment, the shutters were not insulated and the curing blankets were removed 24 hours after casting was completed, which coincided with the time when both T-beams reached their respective maximum effective temperatures. The difference in temperature between the web and the flange was sufficiently large to cause cracks in the unrestrained beam.

The entire width of both sections is shown to exceed the tensile strength at approximately the same time that the vertical top sections was indicated to do so. However, in contrast to the solid beam, the transverse stress in the voided section was more uniform with much smaller stress differentials developing between the centre and flange segments. In this experiment the beams were free to move so that strains could be measured and stresses calculated. The unrestrained voided beam did not crack as the stress difference within the cross section was less than 1.5 MPa.

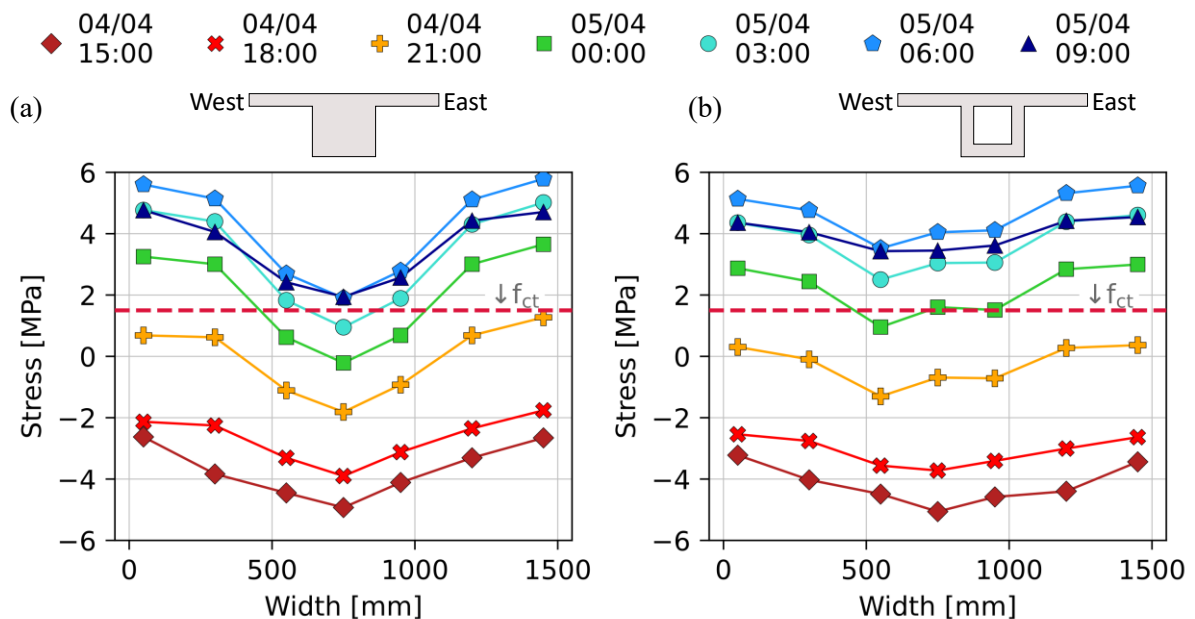
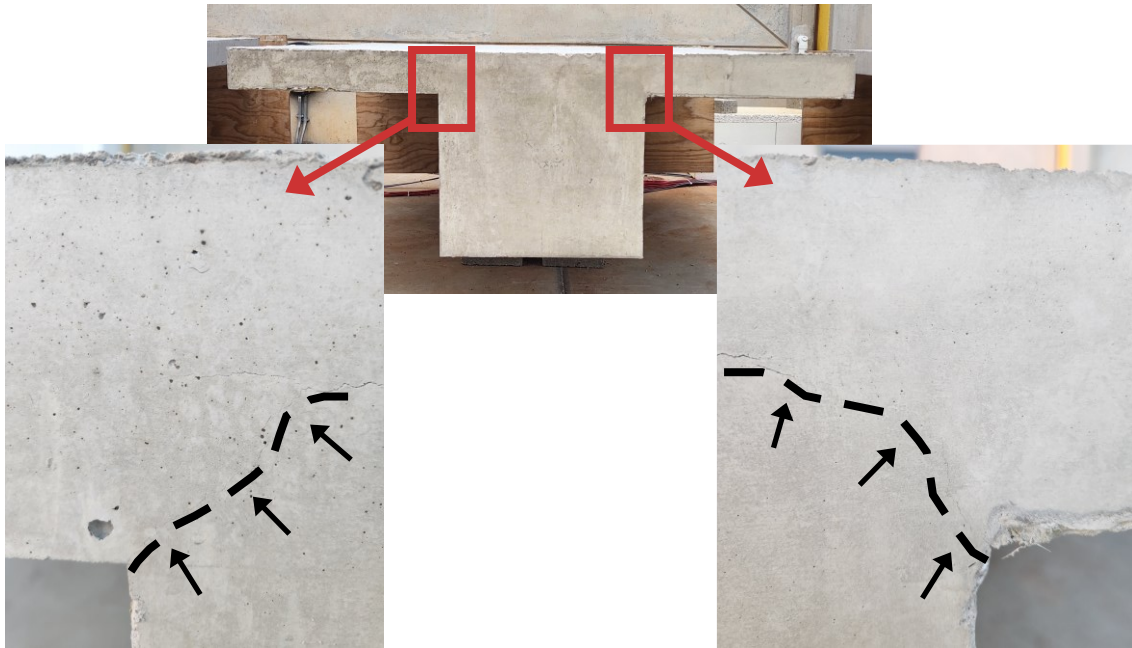


Figure 5-6 Transverse total thermal stress for the (a) solid and (b) voided restrained T-beams on 04/04/2023 to 05/04/2023



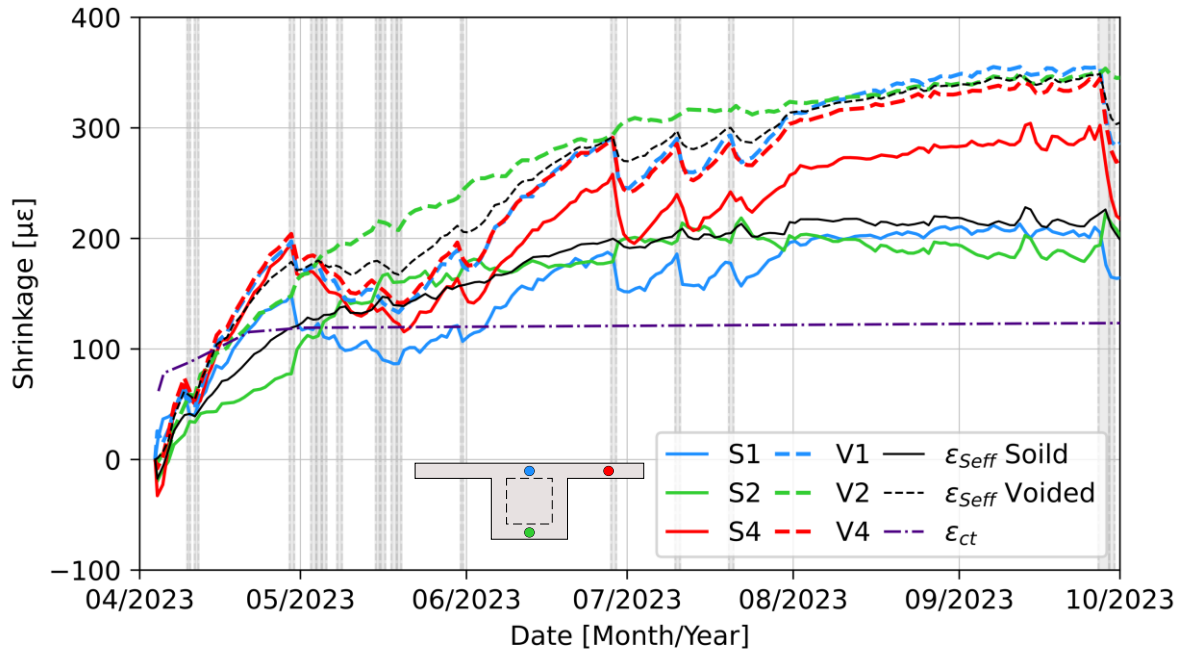
**Figure 5-7 Cracking between web and flange section of solid T-beam**

The cracking between the web and flanges of the solid beam can be prevented by using insulated shutters and curing blankets left in place until the beam core temperature caused by heat of hydration is reduced. The temperature difference and so the stresses would also be reduced if the difference in thickness between the flange and the web of the solid T-beam were decreased, by increasing the flange thickness. A greater flange thickness would increase the thermal inertia of the flange and result in thermal response and behaviour closer to that of the web thereby reducing the stress difference between the web and flange sections. Furthermore, the addition of reinforcement could be used to limit crack widths.

As was the case for the vertical stress distributions, the transverse stresses caused by heat of hydration were also greater than those caused by the temperature changes of a typical day in both sections.

## 5.4 SHRINKAGE

While the shrinkage trends of the two cross-sections were discussed in **Section 4.1.3**, the relation between restrained shrinkage and cracking was excluded. In this section, the differences in shrinkage between the cross-sections and different segments within the cross-sections will be discussed with focus on cracking. **Figure 5-8** displays the measured shrinkage strain of the centre top, centre bottom and centre flange for both cross sections. The concrete tensile strength in terms of strain ( $\epsilon_{ct}$ ) is also included in the figure along with the weighted average shrinkage strain for each cross-section ( $\epsilon_{Seff}$ ).



**Figure 5-8 Shrinkage measurements of selected points**

Since the effective shrinkage of the solid T-beam surpasses the tensile strain capacity of the concrete within the first month after casting, transverse cracks are expected to occur for restrained conditions. Similarly, the voided beam is expected to crack within the first two weeks after casting with the same assumptions. The top measurement points in the voided T-beam (V1 and V4) displayed nearly identical shrinkage over time, which was expected due to the uniform thickness of the top portion of the beam. While the bottom segment of the voided beam also had the same thickness, it showed less shrinkage than the top and still exceeded the tensile strain capacity within the month. For the solid T-beam, noticeable differences in shrinkage were measured between the centre top and bottom (S1 and S2), as well as between the centre top and the centre of the flange (S1 and S4). Even so, both the centre top and flange (S1 and S2) surpassed the tensile strain capacity at similar times than the top centre and flange of the voided section (V1 and V2). Over time the effect of the longer diffusion path created by the solid centre mass of the solid T-beam became more evident as the rate of shrinkage of the S1 was lower than V1. As the flange thickness of the two cross-sections were identical the shrinkages measured by S4 and V4 would be identical, if the flanges were unaffected by the adjacent central segments. Since the



shrinkage of flange (S4) was lower, it can be concluded that it was restrained by the adjacent solid web segment of the solid beam.

The difference in shrinkage between the top and bottom, as particularly prominent in the solid T-beam before the rainfall events in May, induces curvature that if restrained would cause further curvature stresses than quantified by the effective shrinkage values. Furthermore, the differential shrinkage across the width of the section would cause varying stresses between the different segments of the solid T-beam. The effects of restrained shrinkage and temperature curvature are discussed in **Section 5.6.3**.

Since the measured shrinkage strains easily exceed the concrete tensile strain capacity for both sections early on, it is clear that restrained concrete shrinkage is a key factor influencing the cracking potential of concrete.

## 5.5 STRESSES CAUSED BY EFFECTIVE TEMPERATURE AND SHRINKAGE

For structures which are prevented from moving in the axial direction (longitudinally restrained), the dominant stresses which should be considered are the effective (weighted average) stresses produced by temperature and shrinkage. The effective stresses are assumed to develop at the centroid of the section and are the main components in the calculation for total longitudinal stress.

**Figure 5-9** shows the components of effective temperature stress ( $\sigma_{Teff}$ ) and effective shrinkage stress ( $\sigma_{Seff}$ ) as well as their combined effect, total effective stress ( $\sigma_{Totaleff}$ ), over time. The figure displays which component is dominant over time. Initially, the effective temperature stresses govern total effective stress. First, the heat of hydration caused compressive stresses for both cross sections but after the heat dissipated, both sections experienced a net thermal shrinkage. As time progressed, the effective shrinkage became the governing factor, especially for the voided T-beam.

As discussed in **Section 5.3**, the solid beam developed higher effective temperatures ( $T_{eff}$ ) due to the heat of hydration. However, after heat of hydration dissipates the tensile effective temperature stress ( $\sigma_{Teff}$ ) generated in the voided beam is higher than for the solid beam and the daily temperature variation causes a bigger daily stress range (**Section 4.4**). Ultimately, the largest difference in total effective stress between the two cross-sections was the greater effective shrinkage of the voided T-beam. It caused the total effective stress of the voided section to plateau at approximately 15 MPa in comparison to the solid section at about 10 MPa. As the stress effects of temperature and shrinkage curvature were not taken into account for total effective stress, they will be presented and discussed separately in **Section 5.6.3**, for the selected times denoted by the dashed lines in **Figure 5-9**. Furthermore, the effect of rain on the effective shrinkage stress was barely noticeable as the effective shrinkage is a weighted average of the shrinkage values, but its impact becomes clearer when curvature is considered in **Section 5.6.3**.

The time of application of the longitudinal restraint is an important factor to consider when looking at tensile stress development within concrete structures. In monolithically cast structures, for which longitudinal restraint is present from casting, the thermal shrinkage resulting from the dissipation of heat caused by heat of hydration is the key factor that will cause tensile stresses which exceed the tensile capacity of the concrete. If restrained shortly after the initial hydration heat has dissipated, the structure is likely to crack due to shrinkage. Both section's effective shrinkage stresses surpass the concrete tensile strength but because of the short moisture diffusion paths in the thinner, individual segments of the voided T-beam, shrinkage will occur more rapidly and so cause cracking earlier than the solid T-beam. If major cracking due to heat and hydration and shrinkage is to be avoided, longitudinal restraint should only be applied once the effective shrinkage of either section reaches a near constant value. Alternatively additional reinforcement would be required throughout the cross sections to minimise crack widths. This highlights the value of utilising precast elements as the stresses produced from both restrained heat of hydration and restrained early age shrinkage are avoided. The precast element would need to be designed for the stresses developed due to restraint of movement caused by daily temperature cycles as presented in **Section 4.4**, in addition to typical design for applicable dead and live loading.

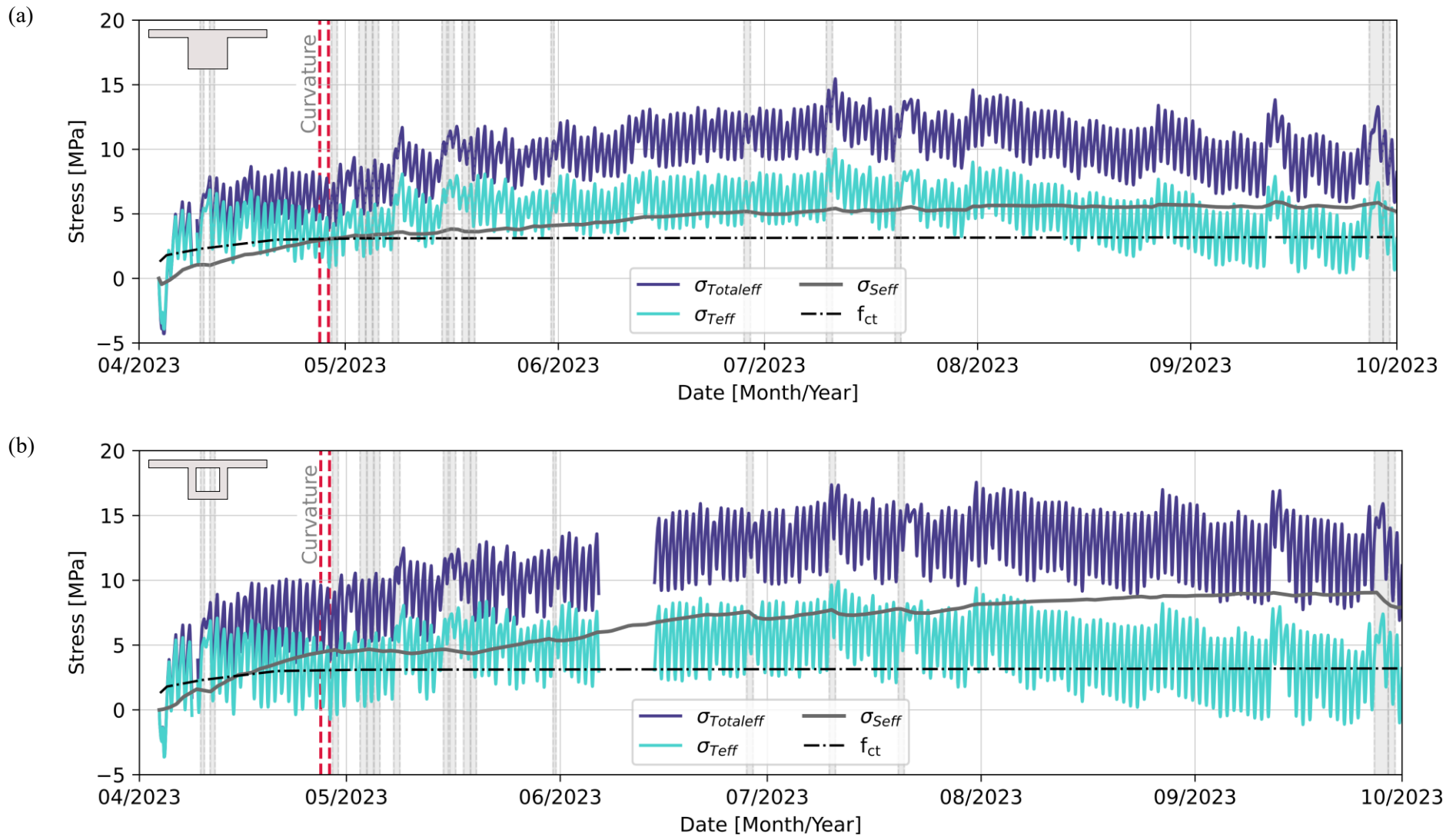


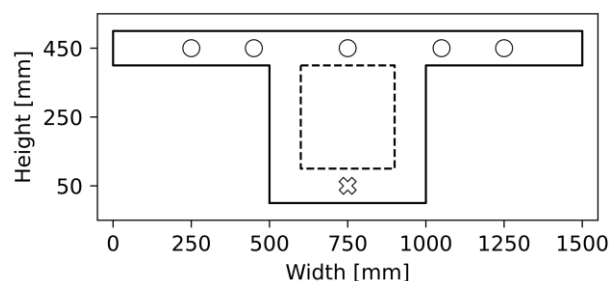
Figure 5-9 Effective stress development over time for the (a) solid and (b) voided restrained T-beams

## 5.6 CURVATURE AND SELF-EQUILIBRATING STRESS

The differential movement between the top and bottom of a structure due to temperature and shrinkage effects caused by environmental loading will induce curvature, or bending, stresses if restrained. In continuous structures which allow longitudinal movement, but restrict curvature with continuity over internal supports, the effective stresses discussed in **Section 5.5** will be absent but curvature stresses will develop. The concept of curvature was briefly outlined in terms of the strain planes for temperature variations in **Section 4.3** but will be discussed in detail in terms of temperature and shrinkage in this section. The self-equilibrating stress which develops within a section irrespective of restraint conditions will also be included in the discussion. With the assumption that rotation (by extension curvature) occurs about the centroid, the sign convention used within the discussion centres about the stresses incurred by restrained curvature. As such, curvature which induces tensile stress beneath the section's centroid will be referred to as positive curvature. Conversely, curvature which induces tensile stress above the section's centroid will be referred to as negative curvature.

To investigate the maximum stresses caused by the combination of shrinkage and temperature, points in time for which the greatest curvature combinations developed were determined. According to the shrinkage measurements displayed in **Figure 5-8**, the largest difference in shrinkage between the top centre points and bottom centre points occurred a few days before the rainfall event on the 29<sup>th</sup> of April. Therefore, the greatest shrinkage induced curvature for both cross sections occurred at the same time. Within this time frame, the largest curvatures caused by temperature were at 07:00 on 27/04/2023 and 13:30 on 28/04/2023 respectively.

The VWSGs were used to determine the curvatures caused by both shrinkage and temperature and since the gauge readings dictate the temperature or strain planes as well as illustrate the presence of self-equilibrating stresses, they will be included in the discussions regarding temperature and shrinkage curvatures which follow. Since the discussion relates to axial strains, the VWSGs orientated in the longitudinal direction as detailed in **Section 3.3.3** and shown in **Figure 5-10**, were considered.



**Figure 5-10 VWSG positions for curvature comparison**

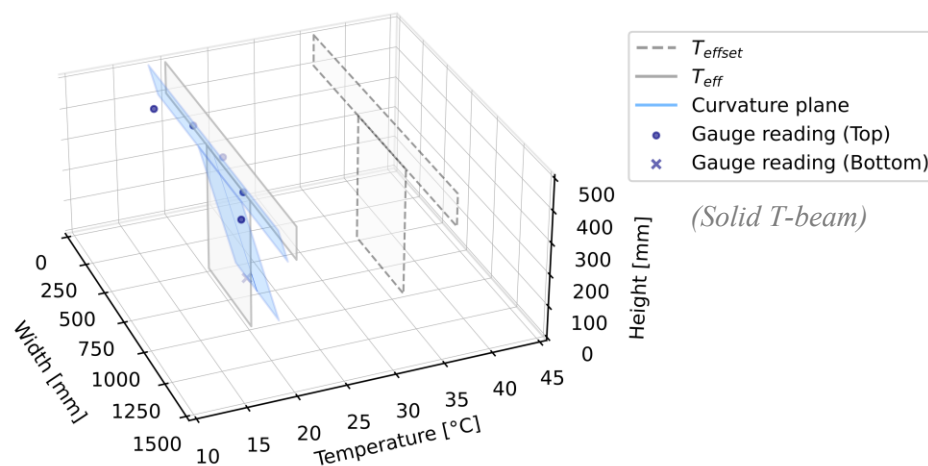
VWSGs were only placed in the centre and to one side of each T-beam, therefore symmetry for the shrinkage measurements were assumed for the side without instrumentation. To aid visualisation in

subsequent plots, a marker differential was used between the top and bottom of the beams. The gauges at height of 450 mm are indicated by circular markers and the gauges at bottom height of 50 mm by a cross.

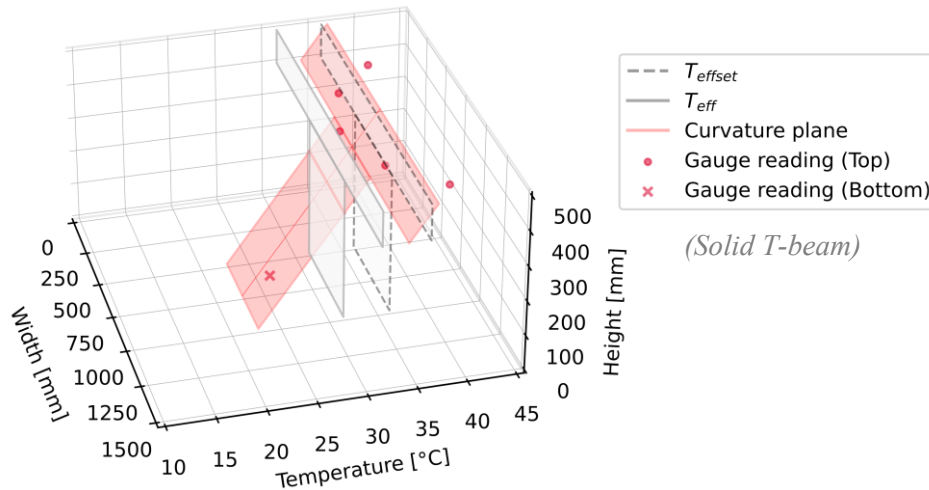
### 5.6.1 Temperature

**Figure 5-11** displays the temperature plane calculated with the assumptions given **Section 3.3.2** along with visual representations of the effective temperatures at final set ( $T_{effset}$ ) and 07:00 on 27/04/2023 for the solid T-beam. This illustrates the difference between the effective temperature at set and the chosen time and highlights the difference between the uniform effective temperature and the ‘tilted’ temperature plane created when the rotation created by temperature differences at different positions, are considered. The temperature plane shaded in blue is directly related to the curvature stresses developed for restrained curvature conditions. Because the top temperatures were lower than those at the bottom, the top would contract, and the bottom extend relative to the section’s centroid. Under restrained conditions, this would induce tensile stresses above the section’s centroid and therefore this temperature case caused negative curvature. Measured values denoted as gauge readings were also included in **Figure 5-11**.

The difference between the gauge readings and the temperature plane are representative of the self-equilibrating stresses which develop within the section to maintain equilibrium. With the same assumptions and reasoning applied in **Figure 5-11**, the effective temperatures at set and at 13:30 on 28/04/2023, along with the temperature plane and gauge readings are shown in **Figure 5-12**. While **Figure 5-11** illustrated conditions for negative curvature, **Figure 5-12** displays the conditions for positive curvature produced by temperature.



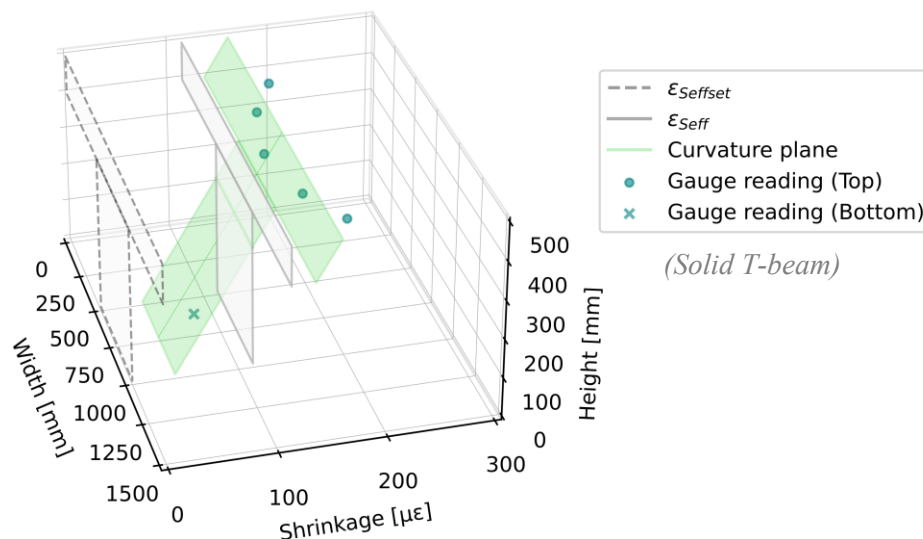
**Figure 5-11** Curvature plane and gauge readings for temperature at 07:00 on 27/04/2023



**Figure 5-12 Curvature plane and gauge readings for temperature at 13:30 on 28/04/2023**

### 5.6.2 Shrinkage

**Figure 5-13** illustrates similar concepts to **Figure 5-11** and **Figure 5-12** but in terms of shrinkage strain instead of temperature. At final set the effective shrinkage strain is zero and this increased to approximately  $115 \mu\epsilon$  for the solid T-beam at the time when maximum curvature occurred. The strain plane for shrinkage was calculated in the same way as for temperature and is shown by the shaded green T-shape. Since the top shrinkage was greater than the bottom, tensile stresses would develop above the section's centroid if restrained, and so this differential shrinkage will induce negative shrinkage curvature. As for temperature, the difference between the gauge readings and the strain plane are representative of the self-equilibrating stress within the section.



**Figure 5-13 Curvature plane and gauge readings for shrinkage on 28/04/2023**

In the interest of visual clarity, the solid T-beam is used for illustrations in **Figure 5-11**, **Figure 5-12** and **Figure 5-13**, but the same concepts were applied to the voided T-beam for the same points in time.

### 5.6.3 Combined Effects of Temperature and Shrinkage

With the individual maximum positive and negative curvature created by temperature and shrinkage identified, the combinations could be analysed and compared to the tensile strength of the concrete to determine the potential for transverse cracking. The combinations for each T-beam yields two distinct scenarios: one with negative shrinkage curvature and positive temperature curvature, and the other with negative shrinkage curvature and negative temperature curvature. The positive temperature and negative shrinkage curvatures would counteract one another but as the positive temperature curvature can be large, the net curvature could be large and positive. In the second scenario, the two negative curvatures are complementary and result in a greater net negative curvature.

**Figure 5-14** and **Figure 5-15** displays the first scenario and **Figure 5-16** and **Figure 5-17** the second scenario for the solid and voided T-beams respectively. In each of the figures, the top row contains two cross-section diagrams, one dedicated to shrinkage and the other to temperature. The effective shrinkage strain ( $\epsilon_{Seff}$ ) and effective shrinkage stress ( $\sigma_{Seff}$ ) are displayed within the cross-section diagram dedicated to shrinkage and even though these effective values would only be applicable if the longitudinal movement of the member is restrained, the curvature is relative to the effective values and the centroid of the member. Therefore, the gauge readings within the cross-section diagram are plotted as a change in shrinkage ( $\delta$ shrinkage in  $\mu\epsilon$ ) with colours correlating to the colour bar alongside.

The same rationale is applicable to the cross-section diagram dedicated to temperature. Below the cross-section diagrams, a grid of plots with three columns and two rows, is displayed. The first column is dedicated to the shrinkage curvature and associated self-equilibrating stresses, the second column to the temperature curvature and associated self-equilibrating stresses and finally the last column contains the summation of the two preceding columns. In each case, the top row is committed to the transverse direction and the bottom row to the vertical direction.

For each graph within the grid, the shrinkage strains and temperatures were converted into stresses ( $\delta$ Stress in MPa) and plotted, also relative to the effective values mentioned before. In the graphs for the transverse direction, horizontal, grey lines indicate the position of the curvature plane at the same level as the gauge readings at 450 mm, based on the assumption that planes remain plane in bending and are therefore constant across the width of the section.

Furthermore, each transverse graph also includes the bottom gauge reading to highlight the difference between top and bottom points relative to each other. The curvature planes are also indicated by straight lines through the neutral axis for the graphs dedicated to the vertical direction. In each graph the gauge reading values are connected with dashed lines which represent the true stress profiles if self-equilibrating stresses are added to the curvature stresses. Considering that the self-equilibrating stresses are present regardless of restraint condition, total curvature stresses will contain the self-equilibrating

stress components for restrained curvature and the combination will be referred to as total curvature stress. For the vertical temperature graphs the measured values from the thermocouples and their interpolations are also included to ensure the correct stress profile shape is displayed due the nonlinear temperature distribution.

In the top right corner of each figure the total effective stress for the given time is indicated to show the stress that would be added to the curvature and self-equilibrating stresses if the T-beams were longitudinally restrained in addition to the applied curvature restraint, from final set. The moment produced by the total curvature stresses caused by the combination of shrinkage and temperature is displayed just below the total effective stress. With the applied sign convention, a net positive curvature would have produced a positive moment, with tension stress at the bottom.

For early afternoon environmental conditions imposed on the solid T-beam (**Figure 5-14**), the negative and positive curvatures from shrinkage and temperature counteract one another resulting in a small positive curvature overall. However, the self-equilibrating stresses have a large impact, resulting in tensile stresses through most of the section. Nonetheless, the total stresses in the vertical direction remained well below the concrete's tensile strength capacity of 3 MPa at this age. In the transverse direction, the curvature at the height of 450 mm of the individual components of shrinkage and temperature counteract one another and the self-equilibrating stresses act in opposite directions resulting in near zero stresses across the width of the T-beam. For the same scenario the voided T-beam (**Figure 5-15**), had a larger positive resultant curvature than the solid T-beam. This was due to the smaller negative shrinkage curvature coupled with a near identical positive temperature curvature compared to the solid T-beam. The total tensile stress (including the self-equilibrating component) below the centroid was higher than for the solid T-beam but also remained below the tensile strength of the concrete.

In the early morning, when the shrinkage and temperature curvatures are complementary, the difference between the two cross sections becomes more noticeable, particularly in the transverse direction (**Figure 5-16** and **Figure 5-17**). In the transverse direction of the solid T-beam, both the shrinkage and temperature stresses have increased tensile stresses from the centre outwards towards the flanges. The shrinkage and temperature components are added together to yield the total stress, which yielded marginally higher tensile stress in the centre and increasingly larger tensile stresses outwards to the flanges. Although the tensile stresses in the flanges where high, the tensile strength was not exceeded. Therefore, the probability of cracking was not high. Even though the shrinkage and temperature curvatures were complementary, the resultant curvature did not develop large enough tensile stresses to surpass the concrete tensile strength at the top of the solid T-beam. In the transverse direction of the voided T-beam, the shrinkage and temperature stresses were tensile but uniform across the beam's width. Therefore, the resultant stress in the transverse direction was also uniform across the width and



only marginally tensile. While both shrinkage and temperature curvatures were negative, both had smaller curvature magnitudes than for the solid T-beam, resulting in a lower net curvature and low tensile stresses at the top of the beam.

The largest total tensile stress in the vertical direction was 1.5 MPa at a height of 50 mm in the voided T-beam for the case of high positive temperature curvature created by early afternoon temperature distributions, coupled with low negative shrinkage curvature. In the transverse direction, the largest tensile stress was 2.8 MPa in the flange of the solid T-beam. This was caused early morning cool weather which induced tensile self-equilibrating stresses from temperature, in combination with the differential shrinkage between the solid centre segment and the flanges. Neither of the maximum tensile stresses would constitute transverse cracks caused by the restraint of curvature and inclusion of self-equilibrating stresses for the selected times.

While the net curvatures and stresses caused by temperature and shrinkage were similar for the T-beams, due to the different cross-sectional properties, the associated bending moments differed significantly. **Figure 5-18** illustrates the difference between the total bending moment for the T-beams. In general, the solid T-beam produced larger daily moment ranges of approximately 110 kNm compared to about 90 kNm in the voided T-beam. Furthermore, the increasingly greater negative curvature experienced by the solid T-beam due to the differential shrinkage between top and bottom of the beam, is characterised by the reducing trend in bending moment within the first month. The influence of the rainfall at the end of April and throughout May can be seen in bending moments of the T-beams as well. For the solid T-beam, the rainfall caused the top portion of the T-beam to swell, reversing the negative curvature caused by greater shrinkage of the top relative to the bottom. With the absence of rainfall in June, the top of the solid beam dries out and the shrinkage differential increased, as shown by the downward trend for the solid T-beam in June. Similar patterns developed for the rainfall events July. The negative curvature due to shrinkage was much smaller in the voided T-beam due to the even thicknesses of the different segments throughout the beam. As such, the bending moments display the daily temperature induced curvature variations but remains constant in times without rainfall. The rain also caused the small amount of negative curvature in the voided beam to be reversed but the top swelled enough to produce positive curvature and thereby positive bending moments which were maintained throughout the study period.

FACTORS INCREASING TENSILE STRESS

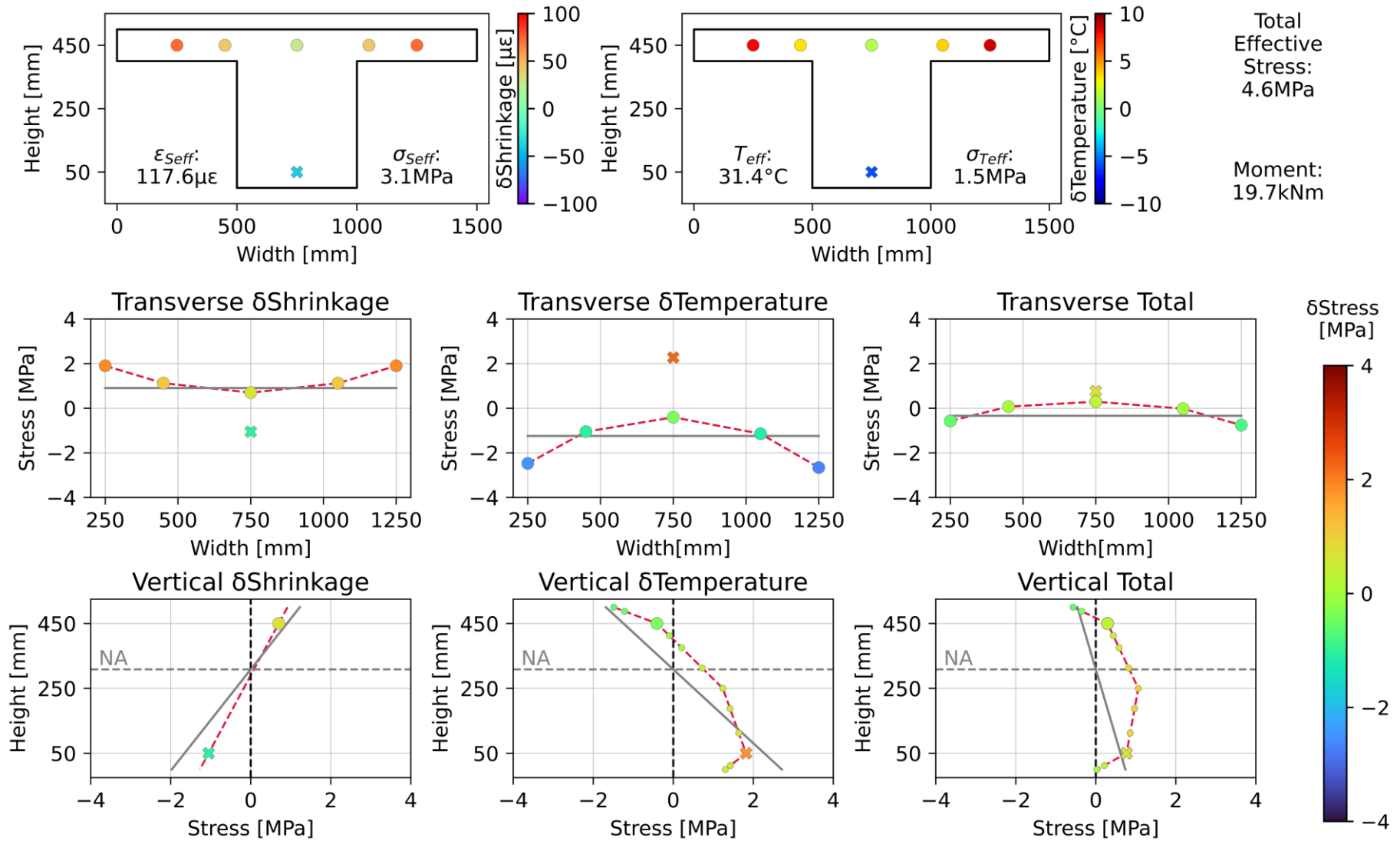


Figure 5-14 Total curvature stresses for the solid T-beam on 28/04/2023 at 13:30

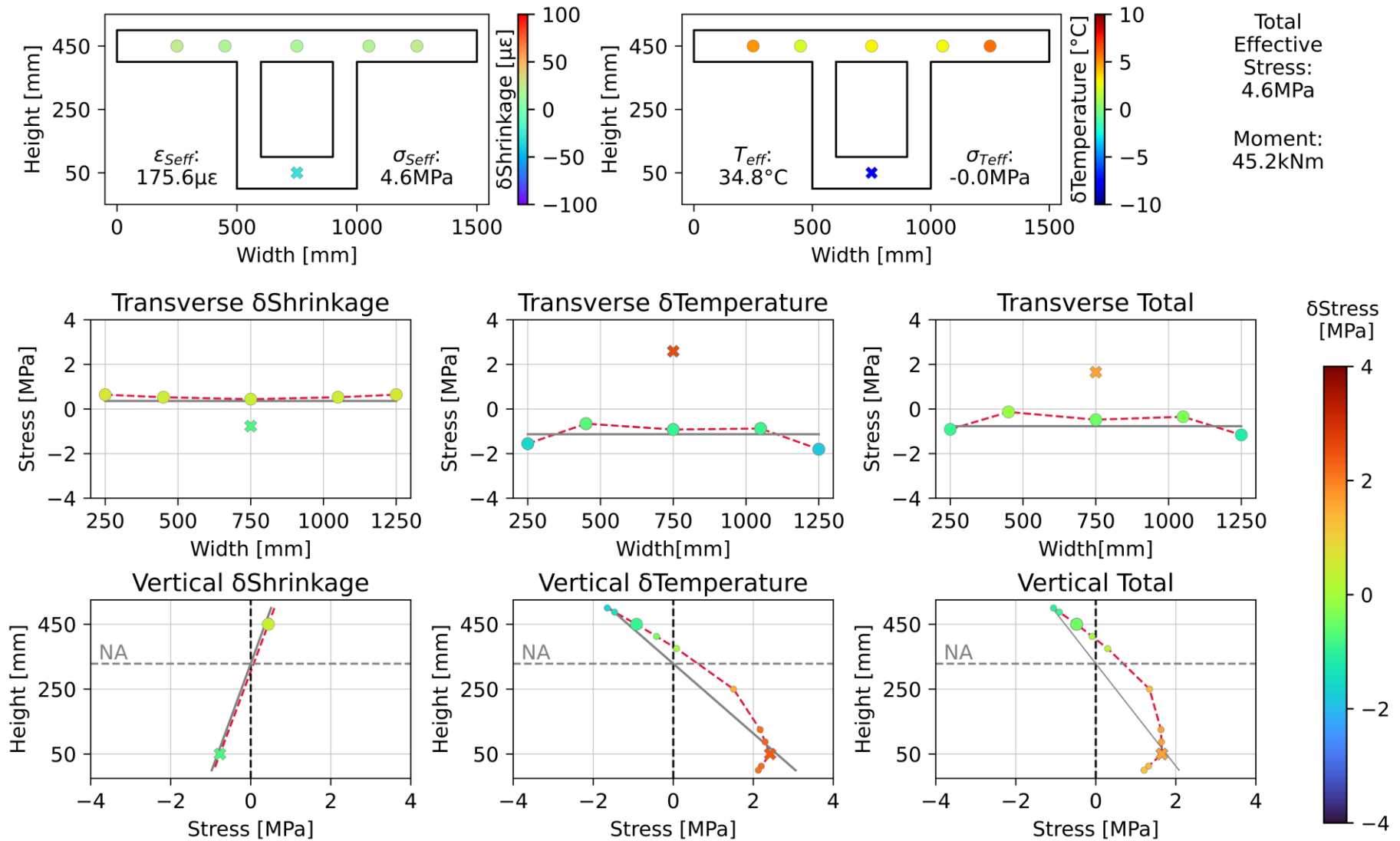


Figure 5-15 Total curvature stresses for the voided T-beam on 28/04/2023 at 13:30

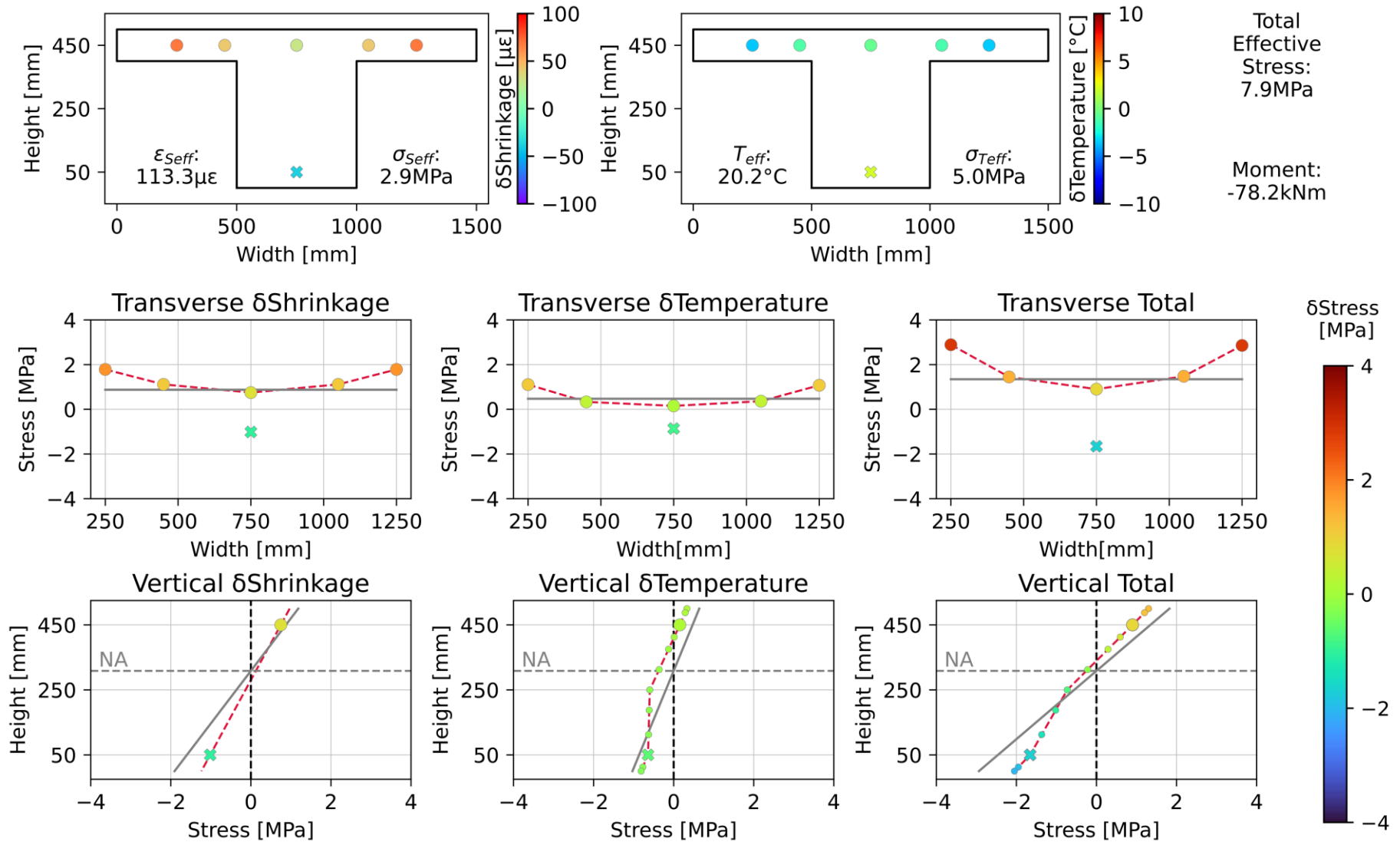


Figure 5-16 Total curvature stresses for the solid T-beam on 27/04/2023 at 07:00

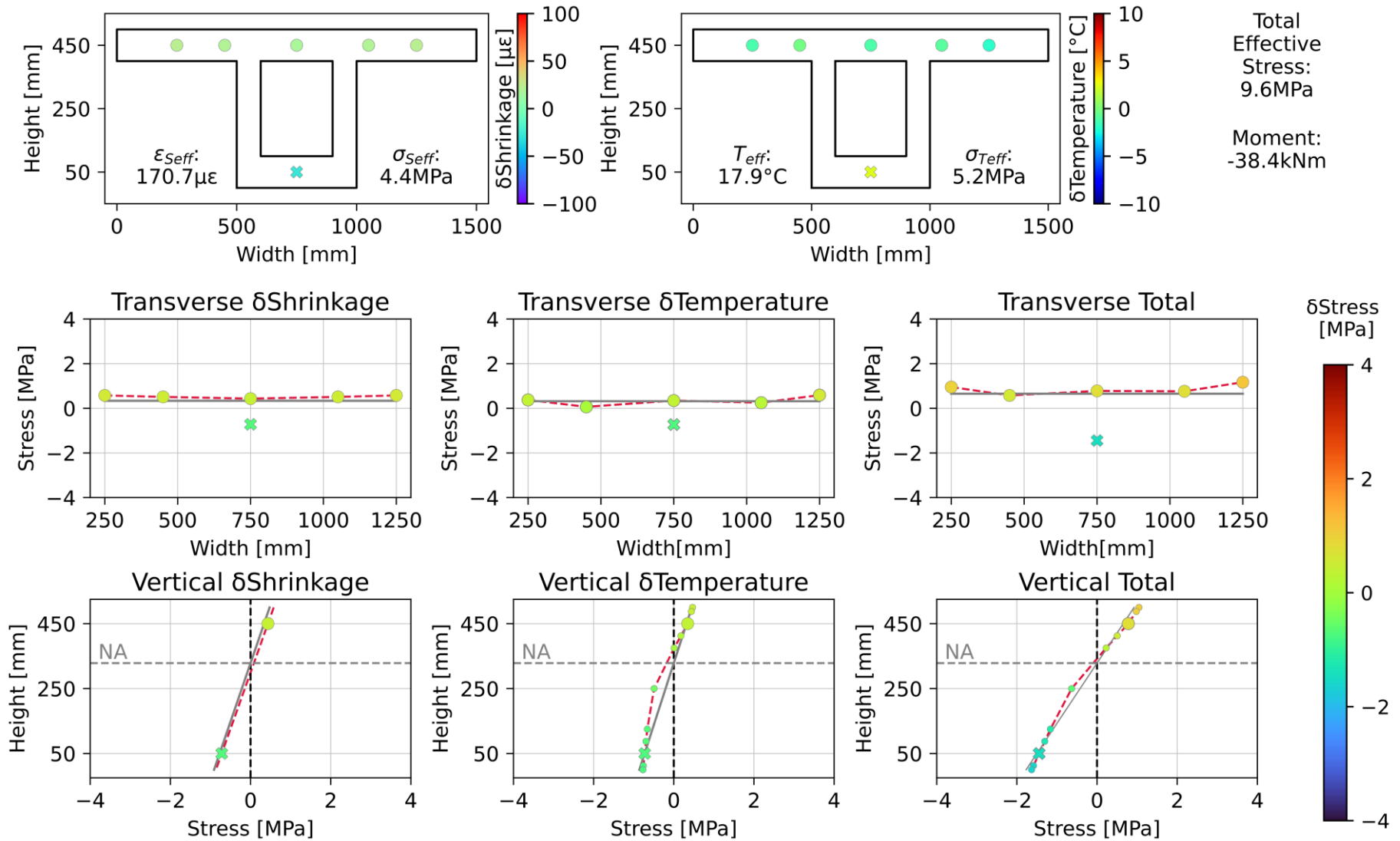
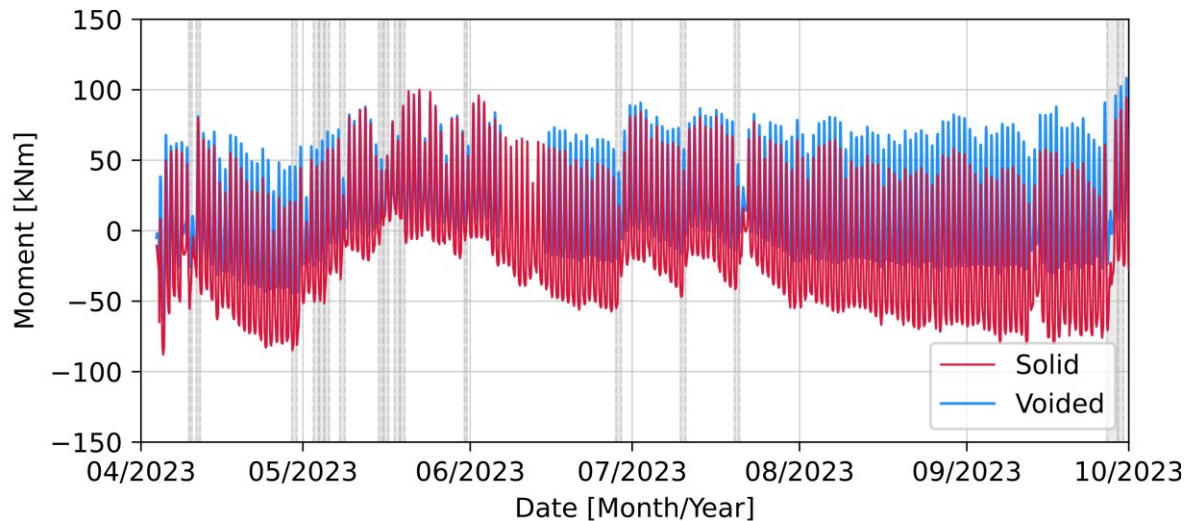


Figure 5-17 Total curvature stresses for the voided T-beam on 27/04/2023 at 07:00



**Figure 5-18 Total bending moment over time**

**Figure 5-14, Figure 5-15, Figure 5-16 and Figure 5-17** only show the stress profiles caused by restraint of temperature and shrinkage curvature for a single point in time. As time progressed, the interactions between temperature and shrinkage within the T-beams varied and so it is necessary to consider both the self-equilibrating stress and the total curvature stress (the combination of curvature stress and self-equilibrating stress) due to restrained curvature, over time. To illustrate the stress profiles for the beams over time, three heights were selected: 0 mm, 250 mm and 500 mm; and the self-equilibrating stress (**Figure 5-19**) and total curvature stress (**Figure 5-20**) at these heights were plotted against time. The self-equilibrating stresses of both sections remained uniform over time and only showed the effects of daily temperature cycles. Furthermore, the tensile capacity of the concrete was never exceeded by tensile self-equilibrating stresses for either section. Although the self-equilibrating stresses contribute to the total stresses over time, their effect alone was insufficient to produce cracking. While the impact of rain was not dominant for longitudinal restraint and by extension the total effective stresses, the effects of rain on total curvature stresses caused by curvature restraint through the section depth can clearly be seen in **Figure 5-20** and the results correspond to the bending moments in **Figure 5-18**.

Before rainfall events, the restrained solid T-beam developed tensile stresses at the top due to the greater shrinkage in the top region, while the bottom went into compression. The rainfall reversed this trend creating tensile stresses at the bottom of the beam and compression at the top. Throughout the observed time, the tensile stresses remained below the concrete's tensile capacity. In the restrained voided T-beam, similar shrinkage and therefore stress was observed by the top and bottom of the beam before rainfall events. As for the solid T-beam, the rainfall caused the top portion of the voided T-beam to swell, creating tensile stress at the bottom of the beam. However, unlike the solid beam, the bottom remained in tension over the times for which rainfall was absent. Furthermore, the tensile stresses developed at the bottom of the restrained voided T-beam surpassed the tensile strength of the concrete during the times of frequent and prolonged rainfall events. It can therefore be concluded that the voided T-beam was more sensitive to rainfall, producing significant tensile stresses for conditions of curvature restraint.

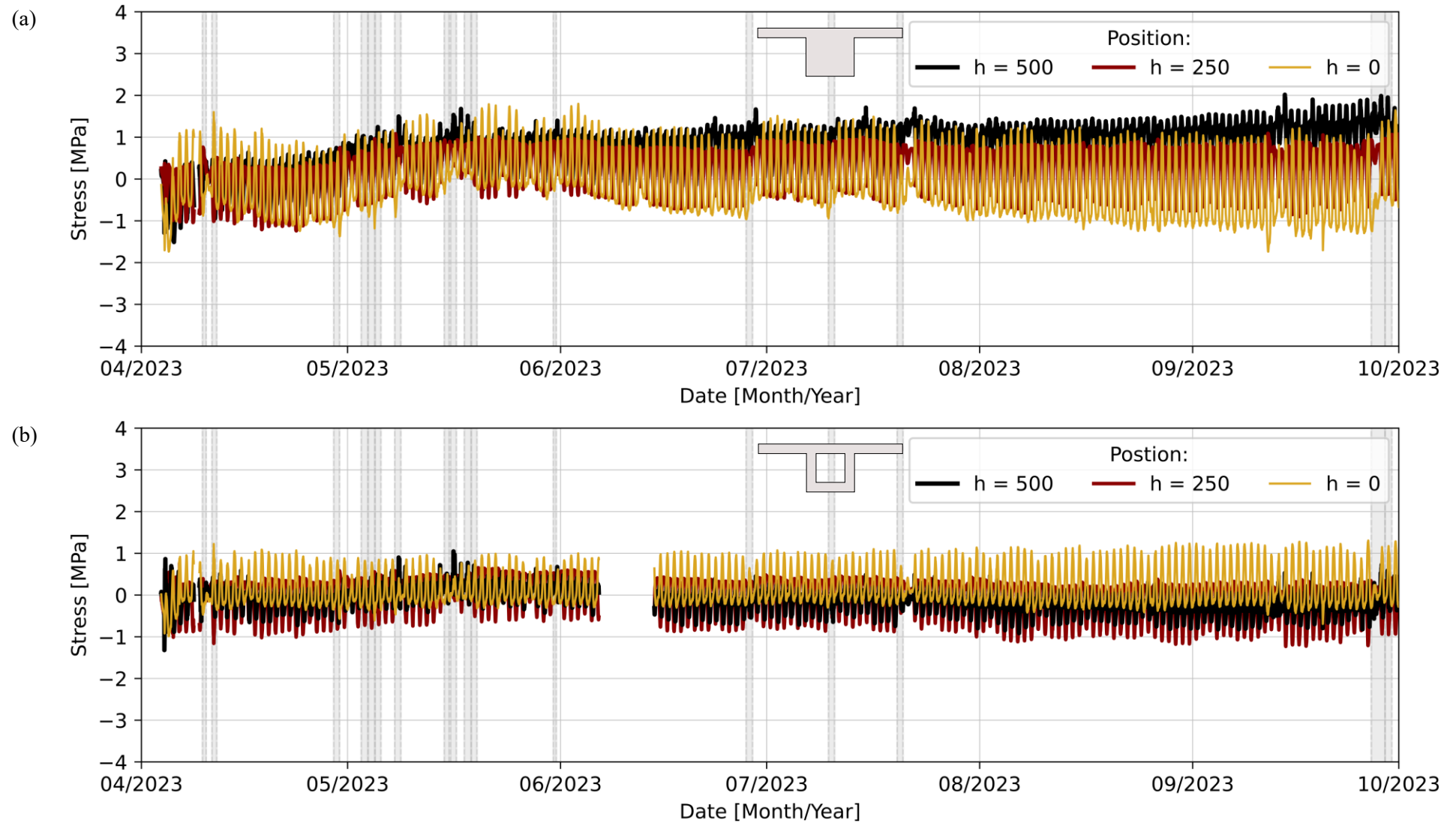


Figure 5-19 Self-equilibrating stress at selected positions of the (a) solid and (b) voided T-beam

FACTORS INCREASING TENSILE STRESS

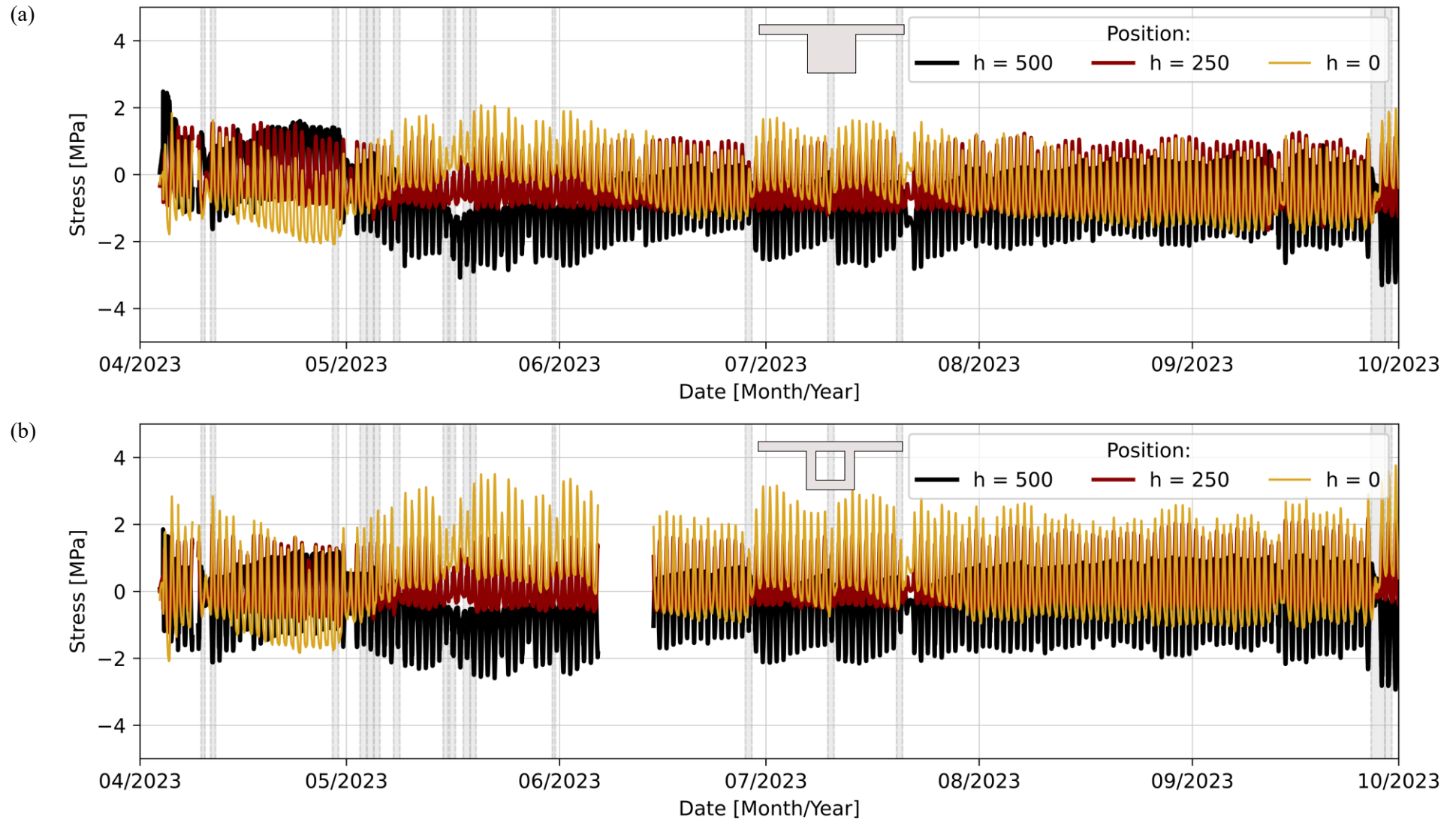


Figure 5-20 Total curvature stress at selected positions of the (a) solid and (b) voided restrained T-beam



## 5.7 SUMMARY OF RESULTS

This chapter presented the stresses developed over time within the T-beams due to temperature and shrinkage and restraint from final set of the concrete. This allowed an overview of stress development over time caused by the individual and combined components of temperature and shrinkage which could be related to the tensile strength of the concrete. The analysis resulted in the following observations:

- Even though the effective temperature at set and maximum effective temperature caused by heat of hydration in the solid beam were higher than in the voided beam, the tensile stresses developed after the heat of hydration dissipated were greater in the voided beam because it reached a significantly lower effective temperature before the daily temperature cycles governed the thermal behaviour of the beams. Therefore, the transverse crack potential of the voided beam was greater than for the solid beam under restrained conditions. Nonetheless, the stresses caused by heat of hydration were larger than stresses produced for a typical day's temperature cycle for both T-beams.
- The greater thermal inertia of the solid beam was beneficial in reducing tensile stresses, despite the higher temperatures reached during heat of hydration. However, in this study the difference in thickness and temperature response between the flange and the web segments of the solid T-beam was too great, resulting in crack formation between the segments despite being unrestrained. The addition of reinforcement could be used to limit crack widths and cracking can be minimized by using insulated shutters which would limit the thermal gradients produced between the core and the flanges until the core temperature reduces. The stresses between the web and flanges would also be reduced if the difference in thicknesses were decreased and chamfering was utilised.
- If axial movement was prevented but curvature is permitted, initially the heat dissipation after peak hydration heat governed total effective stress. As time progressed, the effective shrinkage becomes the dominant factor of total effective stress. The effective shrinkage strain of both cross-sections exceeded the tensile strain capacity of the concrete within the first month after casting was completed. Therefore, under longitudinally restrained conditions from concrete setting time, the stresses would exceed the tensile strength of the concrete and constitute transverse cracking even without taking temperature induced stresses into account.
- The largest tensile stresses were produced as a result of heat of hydration, followed by drying shrinkage of the beams. These can therefore be identified as the key parameters causing critical tensile stresses. These observations highlight the advantageous qualities of precast elements where the main causes of cracking found in this study are avoided.
- The vertical self-equilibrating tensile stresses after the heat of hydration dissipated were not large enough (in either section) to surpass the tensile capacity of the concrete over the remainder

- of the study. Therefore, without restraint, transverse cracking caused by temperature and shrinkage is unlikely.
- The combination of self-equilibrating stresses and curvature stresses (total curvature stress caused by the combination of temperature and shrinkage) for curvature restraint were considered separately from total effective stress. This allowed the scenario at internal supports with axial movement but curvature restraint to be analysed. The total curvature stress developed may be large enough to induce cracks under certain conditions. Within the first couple of days, high tensile stresses were experienced by the bottom of the voided and top of the solid T-beams, which exceed the tensile strength of the concrete. These stresses were developed when heat of hydration governed the stresses. Therefore, cracking is likely to occur at the internal support of monolithically cast members due to the restraint of curvature. Furthermore, critical curvature stresses developed when shrinkage and temperature curvatures were complementary (the same sign). Therefore, these conditions need to be considered in the reinforcement design of the concrete element.
  - The moments caused by the total curvature stress highlighted the difference of the cross-sectional properties of the different cross-sections, but also showed that the impact of rain events can be significant. The effects of rainfall were clearer on curvature stresses than on effective stress. The voided T-beam was more sensitive to rainfall events than the solid T-beam, which caused tensile stresses at the bottom of the beam large enough to cause cracking for curvature restraint. It was notable how small amounts of rain could produce large deformation effects.
  - For the time included in this study, the critical tensile stress conditions in the transverse direction were experienced by the solid T-beam for early morning, cold temperatures with shrinkage conditions where the flange section exhibited greater shrinkage strains than the web. These conditions caused the largest tensile stress in the transverse direction but also the greatest stress differences between the flange and web sections. Since the thickness of the top portion of the voided beam was a uniform thickness, the stresses developed across the width were also uniform.
  - The difference in thickness and thermal inertia between the web and the flange of the solid T-beam caused large stress differentials across the width of the section. This trend was seen through conditions of heat of hydration, shrinkage and daily temperature variations. These stresses could be reduced by determining the an optimum flange/web thickness ratio.

## 6 CONCLUSIONS AND RECOMMENDATIONS

This chapter presents the main conclusions of the study aimed at determining the response of the solid and voided cross-sections to environmental loading, the stress distributions caused by the environmental conditions and the critical restraint conditions which cause high tensile stresses within reinforced concrete T-beams. The trends for the solid and voided T-beams are considered applicable to full scale spine beam and box girder bridge cross sections. Furthermore, the predicted strain calculated by mathematical models were compared to experimental results to assess the accuracy of the analytical calculations and applied assumptions. The existing technical guidelines for bridge design in South Africa were assessed for possible application to the design of concrete T-beams for environmental loading in terms of temperature and shrinkage. Moreover, the magnitudes of self-equilibrating stresses in the cross sections were determined for different conditions and the effects of rainfall were evaluated. The objectives were reached by casting and analysing the temperature and strain data recorded for two statically determinate, reinforced concrete T-beams with solid and voided cross-sections. The support conditions of the beams allowed free movement and therefore strain could be measured and thereby stress profiles could be produced for both cross-sections in the vertical and transverse directions for different environmental and restraint conditions. Recommendations for further research is presented and recommendations for the design and construction of restrained reinforced concrete T-beams for environmental loading is also discussed.

### 6.1 CONCLUSIONS

The following main conclusions relate to the primary objectives listed in **Chapter 1**. The conclusions relating to the individual components temperature and shrinkage are discussed followed by the conclusions relating to the combined effects of temperature and shrinkage.

The following conclusions can be made regarding the effective temperature and thermal stresses developed within the solid and voided T-beam cross-sections:

- Due to the difference in thermal inertia between the solid and the voided T-beams, the effective temperature and stress profiles differed between the two sections. The voided T-beam had greater daily temperature ranges and was considered to be more susceptible to environmental temperature changes.
- Considering a typical day's temperature fluctuations, the higher thermal inertia of the solid T-beam was beneficial and resulted in smaller mean elongation and contraction deformation due to temperature and so resulted in smaller total thermal stresses for fully restrained conditions when compared to the voided T-beam.

- For the same typical day, both the solid and the voided T-beams developed temperature differences between the top and the bottom of the beam which resulted in curvature stresses as a result of curvature restraint. The curvature stresses developed in the two cross-sections were similar, but the thermal moments varied due to the unique cross-sectional properties of each beam.
- The total thermal stresses created in the transverse direction for a typical day were generally uniform for the voided section but varied from centre outwards to the flanges in the solid beam creating high stress at the transition point from web to flange. As such, the transverse direction is more important in the solid section than in the voided section for typical temperature variation.
- Neither section produced sufficient tensile stresses for fully restrained conditions during a typical daily temperature cycle to conclusively produce transverse cracking. Therefore, critical tensile stresses due to environmental loading were not caused by typical daily temperature changes.
- When full restraint of curvature and axial movement is considered from final set of the concrete, the largest contribution toward tensile stress is caused by the effects of cement hydration. The tensile stresses caused by the dissipation of heat of hydration exceeded the tensile strength of the concrete in some regions of both cross-sections. Interestingly, even though the solid section had a higher effective temperature at final set, the voided section had a greater decrease in effective temperature compared to its temperature at set, therefore the tensile stresses developed throughout the voided section were greater due to heat of hydration than for the solid beam.
- In the transverse direction, the differential temperatures between the flange and the web sections, caused by the uneven dissipation of heat caused by cement hydration, were large enough to cause cracking of the unrestrained solid T-beam. This highlighted the need to consider the transverse direction of the solid T-beam, as was the case for typical daily temperatures cycles.
- The analytically calculated thermal strains showed good correlation to the measured strains. The correlation was better for the voided section, but the slightly larger deviation of the solid section can be attributed to the presence of cracking between the flange and the web of the solid section. The correlation validated the calculated thermal strains as well as the applied assumptions and so showed the strain behaviour could be predicted from temperature using mathematical models.

The following conclusions can be made regarding the shrinkage strains developed within the solid and voided T-beam cross-sections:

- The effective shrinkage strains of both solid and voided cross-sections surpassed the tensile strain capacity of the concrete within the first month after casting. Therefore, the rate of early age drying shrinkage must be taken into account in reinforced concrete design.
- Greater effective shrinkage was observed for the voided T-beam throughout the study duration.
- Both cross-sections exhibited differential shrinkage strains between the top and bottom of the beam. The differences between top and bottom shrinkage strain were however more pronounced in the solid section. Similarly, the solid T-beam showed greater strain differences between the flange and the web region, which demonstrated the influence of the solid core on the adjacent flange sections. Due to the uniform thickness across the width of the voided section, shrinkage strains were also identical.

The following conclusions can be made regarding the combined effects of temperature and shrinkage on the stresses developed within the solid and voided T-beam cross-sections:

- Assuming longitudinally restrained conditions initiated from the final setting time of the concrete, the total stress was initially governed by the tensile stresses caused by the dissipation of heat of hydration after final set. However, as time progressed, effective shrinkage became dominant in both cross sections. Therefore, it can be concluded that for longitudinal restraint from set the largest parameter contributing early age tensile stress development is heat of hydration, followed by shrinkage.
- The individual stress caused by heat of hydration and shrinkage over time both surpassed the tensile stresses developed due to daily temperature variations.
- For longitudinal restraint the total stress of the voided T-beam was greater when compared to the solid T-beam, mainly due to the higher effective shrinkage component. Furthermore, the restraint of longitudinal movement produced much greater tensile stresses when compared to curvature restraint.
- The difference between the two sections became more pronounced when temperature and shrinkage are considered for curvature restraint. During the study period the critical curvature conditions developed when the curvatures for temperature and shrinkage were complementary (in the same direction). This was the case for both T-beams. The total curvature stresses were affected by temperature cycles, shrinkage and swell caused by rain events. However, the voided T-beam showed greater sensitivity to both temperature and moisture changes, by developing higher stresses and stress ranges over time.

The following conclusions relate to the secondary objectives listed in **Chapter 1**:

- TMH7:1981 provided adequate temperature distribution shape and magnitude guidelines which could potentially be used for any concrete element with nonlinear temperature distributions caused by thermal environmental loading. However, TMH7:1989 provided mixed results for shrinkage predictions over time. Overall, the shrinkages of the T-beams were underestimated for the duration of the study, especially during the first month. The 6-month shrinkage prediction for the solid beam was better than for the voided beam but was still underpredicted strain by  $30 \mu\epsilon$ . Therefore, the shrinkage prediction model presented by TMH7:1989 was not optimal and would require adjustment to be applicable to varied cross-sections and sizes, especially at early ages.
- The tensile self-equilibrating stresses within both sections caused by temperature and shrinkage were not high enough to induce transverse cracking, however the self-equilibrating stresses within the solid section were marginally larger over the duration of the study. Between the stress components caused by axial restraint, curvature restraint and internal equilibrium, the self-equilibrating stress component was the smallest stress component, but influenced total stress nonetheless.
- Rainfall had significant impacts on the beams, reversing shrinkage particularly at the top portion of both beams. The voided beam was more sensitive to the rainfall especially for restrained curvature, as rain created sufficient swell in the top portion to keep bending moments predominantly positive, causing tension in the bottom fibres, throughout the study duration and caused sufficient tensile stresses at the bottom of the voided section to exceed the tensile strength of the concrete. The effects of rainfall were less noticeable for the solid beam, but the curvature induced by differential shrinkage of the top and bottom could also be reversed by frequent or prolonged rainfall. Therefore, it can be concluded that rainfall should be considered as a major factor of environmental loading.

The research completed in this study highlights the need for environmental conditions to be considered in the design of restrained reinforced concrete elements, irrespective of cross-section type. Depending on the application and restraint condition the combined response to environmental and typical design loading of one cross-section would be favoured over another, but analysis of the combination of shrinkage and thermal behaviour is necessary, regardless of the cross-section type.

## 6.2 RECOMMENDATIONS FOR FURTHER RESEARCH

Based on the conclusions and scope of this study the following aspects should be considered for further research:

- The effect of varied flange to web thickness ratios for the solid beam to determine if an optimal ratio can be found which balances the benefits of high thermal inertia while not excessively increasing the self-weight or heat of hydration. Such investigation should also include tapered thickness from centre to flange at different slopes.
- The influence of surface colour and surface sealants should be considered for both temperature distributions and shrinkage.
- The time interval between casting and restraint of the beams should also be varied and the impact evaluated.
- The interaction between the self-equilibrating and curvature stresses should be investigated at varied section depths.
- The period included in this study only included Autumn, Winter and part of Spring and so the stresses produced for mid-Summer temperatures should also be evaluated.
- The experimental data can be used to calibrate numerical models which can in turn be used to establish the sensitivity of the response to environmental loading on all the different material properties of the concrete, such as different coefficients of thermal expansion and elastic moduli.

### **6.3 RECOMMENDATIONS FOR DESIGN AND CONSTRUCTION OF REINFORCED CONCRETE BEAMS EXPOSED TO ENVIRONMENTAL LOADING**

Even though the study contained the analysis of scale model T-beams, the trends and conclusions should also be valid for full scale bridges.

The following points should be considered to reduce the tensile stresses within reinforced concrete beams or bridge cross-sections:

- Curing conditions have a significant impact on the thermal gradients caused by heat of hydration. Therefore, insulated shutters and prolonged use of curing blankets should be implemented to reduce the thermal gradients developed within sections. This is particularly applicable to solid sections with varying thicknesses through the cross-section.
- The web/flange thickness ratio must be considered for both temperature and shrinkage behaviour, particularly for solid sections.
- Precast elements should be considered if fully restrained end conditions are applicable. Otherwise, the timing of restraint (when beams are tied-in to other members) must be considered. For example, delay in restraint should be considered to allow drying shrinkage before restraints are imposed.
- The overall behaviour of any cross-section will be influenced by the material properties of the selected constituents in a concrete mix design. As such, the unique material properties of any mix design must be taken into account.



## 7 REFERENCES

- Abid, S.R. (2018). Three-dimensional finite element temperature gradient analysis in concrete bridge girders subjected to environmental thermal loads. *Cogent Engineering*, 5(1).
- Abid, S.R., Tayşi , N. and Özakça, M. (2014). Experimental measurements on temperature gradients in concrete box-girder under environmental loadings. In: *Proceedings of the Istanbul Bridge Conference, 2014*. Istanbul.
- Abid, S.R., Tayşi, N. and Özakça, M. (2016). Experimental analysis of temperature gradients in concrete box-girders. *Construction and Building Materials*, 106(2016), pp.523–532.
- Abid, Sallal.R., Tayşi, N., Özakça, M., Xue, J. and Briseghella, B. (2021). Finite element thermo-mechanical analysis of concrete box-girders. *Structures*, 33(2021), pp.2424–2444.
- ACI Committee 207 (2022). *ACI PRC-207.1-21: Mass Concrete - Guide*. Farmington Hills, Michigan: American Concrete Institute.
- ACI Committee 209 (2008). *ACI 209.2R-08: Guide for Modeling and Calculating Shrinkage and Creep in Hardened Concrete*. American Concrete Institute.
- ACI Committee 301 (2020). *ACI SPEC-301-20: Specifications for Concrete Construction*. Farmington Hills, Michigan: American Concrete Institute.
- Al-Saleh, S.A. and Al-Zaid, R.Z. (2006). Effects of drying conditions, admixtures and specimen size on shrinkage strains. *Cement and Concrete Research*, 36(10), pp.1985–1991.
- Alexander, M.G. ed., (2021). *Fulton’s concrete technology*. 10th ed. Midrand, South Africa: Cement & Concrete SA.
- Alumudaiheem, J.A. and Hansen, W. (1987). Effect of Specimen Size and Shape on Drying Shrinkage of Concrete. *ACI Materials Journal*, 84(2), pp.130–135.
- ASTM Standard (2022). *C469/C469M -22: Static Modulus of Elasticity and Poisson’s Ratio of Concrete in Compression*. ASTM International, United States.
- ASTM Standard (2014). *CI57/CI57M-17: Standard test method for length change of hardened hydraulic cement mortar and concrete*. ASTM International, United States.

- Baroghel-Bouny, V. and Godin, J. (2001). Experimental study on drying shrinkage of ordinary and high-performance cementitious materials. *Concrete science and engineering*, 3(9), pp.13–22.
- Bartojay, K. (2012). *Thermal Properties of Reinforced Structural Mass Concrete Dam Safety Technology Development Program*. Denver, Colorado: U.S. Department of the Interior Bureau of Reclamation.
- Bazant, Z.P. and Murphy, W.P. (1995). Creep and shrinkage prediction model for analysis and design of concrete structures— model B3. *Materials and Structures*, 28(180), pp.357–365.
- Beverly, P. and International Federation For Structural Concrete (2013). *FIB model code for concrete structures 2010*. Berlin Ernst.
- Bissonnette, B., Pierre, P. and Pigeon, M. (1999). Influence of key parameters on drying shrinkage of cementitious materials. *Cement and Concrete Research*, 29(10), pp.1655–1662.
- Black, W., Moss, D.S. and Emerson, M. (1976). *TRRL Report LR 748: Bridge temperatures derived from measurement of movement*. Crowthorne: Department of the Environment (Transport and Road Research Laboratory).
- Bolander, J.E. (2018). *Controlling Temperature and Shrinkage Cracks in Bridge Decks and Slabs*. California Department of Transportation.
- Branco, F.A. and Mendes, P.A. (1993). Thermal Actions for Concrete Bridge Design. *Journal of Structural Engineering*, 119(8), pp.2313–2331.
- Brown, M., Seller, G., Folliard, K.J. and Fowler, D.W. (2001). *Restrained Shrinkage Cracking of Concrete Bridge Decks: State-of-the-art review*. Austin Texas: Center for Transportation Research, Bureau of Engineering Research.
- Chen, B., Ding, R., Zheng, J. and Zhang Shi-Biao (2009). Field test on temperature field and thermal stress for prestressed concrete box-girder bridge. *Frontiers of Architecture and Civil Engineering in China*, 3(2), pp.158–164.
- Chijiwa, N., Hayasaka, S. and Maekawa, K. (2018). Long-Term Differential and Averaged Deformation of Box-Type Pre-stressed Concrete Exposed to Natural Environment. *Journal of Advanced Concrete Technology*, 16, pp.1–17.
- Clark, L.A. (1983). *Concrete bridge design to BS 5400*. London: Construction Press.

- Committee of State Road Authorities (1981). *TMH7: 1981 Parts 1 and 2: Code of Practice for the Design of Highway Bridges and Culverts in South Africa*. Pretoria: Department of Transport.
- Committee of State Road Authorities (1989). *TMH7: 1981 Parts 3: Code of Practice for the Design of Highway Bridges and Culverts in South Africa*. Pretoria: Department of Transport.
- Do, T.A., Hoang, T.T., Bui-Tien, T., Hoang, H.V., Do, T.D. and Nguyen, P.A. (2020). Evaluation of heat of hydration, temperature evolution and thermal cracking risk in high-strength concrete at early ages. *Case Studies in Thermal Engineering*, 21(100658).
- Do, T.A., Tia, M., Nguyen, T.H., Hoang, T.T. and Tran, T.D. (2021a). Assessment of Temperature Evolution and Early-Age Thermal Cracking Risk in Segmental High-Strength Concrete Box Girder Diaphragms. *KSCCE Journal of Civil Engineering*, 26(1), pp.166–182.
- Do, T.A., Verdugo, D., Tia, M. and Hoang, T.T. (2021b). Effect of volume-to-surface area ratio and heat of hydration on early-age thermal behavior of precast concrete segmental box girders. *Case Studies in Thermal Engineering*, 28(2021).
- Downie, B. (2005). *Effect of moisture and temperature on the mechanical properties of concrete*. Thesis, West Virginia University.
- El-Tayeb, E.H., El-Metwally, S.E., Askar, H.S. and Yousef, A.M. (2017). Thermal analysis of reinforced concrete beams and frames. *HBRC Journal*, 13(1), pp.8–24.
- Elbadry, M. and Ghali, A. (1986). Thermal Stresses and Cracking of Concrete Bridges. *ACI Journal*, 83-90.
- Emerson, M. (1976). *Extreme Values of Bridge Temperatures for Design Purposes*. Crowthorne, Berkshire : Transport and Road Research Laboratory.
- European Committee for Standardization (2004). *EN 1992-1-1:2004: Eurocode 2: Design of concrete structures - Part 1-1: General rules and rules for buildings*. Brussels.
- Feng, Z., Jinyi, L. and Lei, G. (2022). Experimental investigation of temperature gradients in a three-cell concrete box-girder. *Construction and Building Materials*, 335(2022), p.127413.
- French, C., Eppers, L., Le, Q. and Hajjar, J.F. (1999). Transverse Cracking in Concrete Bridge Decks. *Transportation Research Record: Journal of the Transportation Research Board*, 1688(1), pp.21–29.
- Gao, X., Qu, G.-B. and Zhang, A. (2012). Influences of reinforcement on differential drying shrinkage of concrete. *Journal of Wuhan University of Technology-Mater. Sci. Ed.*, 27(3), pp.576–580.

- Ge, Z., Wang, K., Sandberg, P. and Ruiz, J.M. (2009). Characterization and Performance Prediction of Cement-Based Materials Using a Simple Isothermal Calorimeter. *Journal of Advanced Concrete Technology*, 7(3), pp.355–366.
- Ghali, A. and Favre, R. (1986). *Concrete Structures: Stresses and Deformations*. London: Chapman & Hall.
- Gu, B., Chen, Z. and Chen, X. (2014). Temperature gradients in concrete box girder bridge under effect of cold wave. *Journal of Central South University*, 21(3), pp.1227–1241.
- Hadidi, R. and Saadeghvaziri, M.A. (2005). Transverse Cracking of Concrete Bridge Decks: State-of-the-Art. *Journal of Bridge Engineering*, 10(5), pp.503–510.
- Hagedorn, R., Martí-Vargas, J.R., Dang, C.N., Hale, W.M. and Floyd, R.W. (2019). Temperature Gradients in Bridge Concrete I-Girders under Heat Wave. *Journal of Bridge Engineering*, 24(8).
- Han, S., Liu, Y., Lyu, Y., Liu, J. and Zhang, N. (2023). Numerical simulation investigation on hydration heat temperature and early cracking risk of concrete box girder in cold regions. *Journal of Traffic and Transportation Engineering*, 10(4), pp.697–720.
- Issa, M.A. (1999). Investigation of Cracking in Concrete Bridge Decks at Early Ages. *Journal of Bridge Engineering*, 4(2), pp.116–124.
- Kada, H., Lachemi, M., Petrov, N., Bonneau, O. and Aïtcin, P.C. (2002). Determination of the coefficient of thermal expansion of high performance concrete from initial setting. *Materials and Structures*, 35(1), pp.35–41.
- Kadlec, L., Křístek, V. and Strobach, C.P. (2017). Effects of Differential Shrinkage in Concrete Bridges. *Solid State Phenomena*, 259, pp.158–163.
- Kang, X., Lei, H. and Xia, Z. (2020). A comparative study of modified fall cone method and semi-adiabatic calorimetry for measurement of setting time of cement based materials. *Construction and Building Materials*, 248(2020), p.118634.
- Krauss, P.D. and Rogalla, E.A. (1996). *Transverse Cracking in Newly Constructed Bridge Decks*. Washington, D.C.: National Academy Press.
- Křístek, V., Bazant, Z.P., Zich, M. and Kohoutkova, A. (2005). Why is the Initial Trend of Deflections of Box Girder Bridges Deceptive. In: *Creep, Shrinkage and Durability of Concrete Structures: CONCREEP 7*.

- Kulprapha, N. and Warnitchai, P. (2012). Structural health monitoring of continuous prestressed concrete bridges using ambient thermal responses. *Engineering Structures*, 40(2012), pp.20–38.
- Larsson, O. and Thelandersson, S. (2012). Transverse thermal stresses in concrete box cross-sections due to climatic exposure. *Structural Concrete*, 13(4), pp.227–235.
- Lee, J.-H. (2012). Investigation of Extreme Environmental Conditions and Design Thermal Gradients during Construction for Prestressed Concrete Bridge Girders. *Journal of Bridge Engineering*, 17(3), pp.547–556.
- Lee, J.-H. and Kalkan, I. (2012). Analysis of Thermal Environmental Effects on Precast, Prestressed Concrete Bridge Girders: Temperature Differentials and Thermal Deformations. *Advances in Structural Engineering*, 15(3), pp.447–459.
- Leonhardt, F. and Lippoth, W. (1970). Folgerungen aus Schäden an Spannbetonbrücken. *Beton- und Stahlbetonbau*, 10(65), pp.231–244.
- Maher, D.R.H. (1970). The effects of differential temperature on continuous prestressed concrete bridges. *Civil Engineering Transactions*, 12(1).
- Mateos, A., Harvey, J., Bolander, J., Wu, R., Paniagua, J. and Paniagua, F. (2019). Field evaluation of the impact of environmental conditions on concrete moisture-related shrinkage and coefficient of thermal expansion. *Construction and Building Materials*, 225(2019), pp.348–357.
- Mosley, B., Bungey, J. and Hulse, R. (2012). *Reinforced concrete design to Eurocode 2*. 7th ed. Houndmills: Palgrave Macmillan.
- Naaman, A.E. (2001). Reinforced Concrete. In: K.H.J. Buschow, R.W. Cahn, M.C. Flemings, B. Ilshner, E.J. Kramer, S. Mahajan and P. Veyssi re, eds., *Encyclopedia of Materials: Science and Technology*, 2nd ed. Oxford: Elsevier, pp.8095–8109.
- Nair, H., Ozyildirim, C. and Sprinkel, M.M. (2016). *Reducing Cracks in Concrete Bridge Decks Using Shrinkage Reducing Admixture*. Charlottesville, Virginia: Virginia Transportation Research Council.
- Ng, S., Low, K.-S. and Tioh, N.-H. (2011). Newspaper sandwiched aerated lightweight concrete wall panels—Thermal inertia, transient thermal behavior and surface temperature prediction. *Energy and Buildings*, 43(7), pp.1636–1645.
- Orta, L. and Bartlett, F.M. (2014). Stresses Due to Restrained Shrinkage in Concrete Deck Overlays. *ACI Materials Journal*, 111-M63, pp.701–710.

- Peiretti, H.C., Parrotta, J.E., Oregui, A.B., Caldentey, A.P. and Fernandez, F.A. (2014). Experimental Study of Thermal Actions on a Solid Slab Concrete Deck Bridge and Comparison with Eurocode 1. *Journal of Bridge Engineering*, 19(10).
- Potgieter, I.C. (1983). *Response of Highway Bridges to Nonlinear Temperature Distributions*. Thesis: University of Illinois at Urbana-Champaign.
- Priestly, M.J.N. (1972). Model study of a prestressed concrete box-girder bridge under thermal loading. In: *IABSE Congress report - Ninth Congress*. Amsterdam: IABSE publications, pp.737–746.
- Priestly, M.J.N. (1976). Design thermal gradients for concrete bridges. *New Zealand Engineering*, 31(9), p.213.
- Priestly, M.J.N. (1978). Design of Concrete Bridges for Temperature Gradients. *ACI Journal*, 75-23.
- Priestly, M.J.N. and Wood, J.H. (1977). Comparison between theory and in-situ tests for a complex box-girder bridge. In: *International Symposium on testing in situ of Concrete Structures*. Budapest, Hungary.
- Radolli, M. and Green, R. (1975). Thermal stresses in concrete bridge superstructures under summer conditions. In: *Transportation Research Record*. 54th Annual Meeting of the Transportation Research Board. Transportation Research Board, pp.23–36.
- Reynolds, J. and Emanuel, J.H. (1974). Thermal Stresses and Movements in Bridges. *Journal of the Structural Division*, 100(1), pp.63–78.
- Rodriguez, L.E. (2012). *Temperature Effects on Integral Abutment Bridges for the Long-Term Bridge Performance Program*. Dissertation: Utah State University.
- Roeder, C.W. (2003). Proposed Design Method for Thermal Bridge Movements. *Journal of Bridge Engineering*, 8(1), pp.12–19.
- RST Instruments LTD. (2019). *Vibrating Wire Embedment Strain Gauge (VWSG-E) Manual*. Canada: RST Instruments LTD.
- Samouh, H., Roziere, E. and Loukili, A. (2016). Drying Depth and Size Effect on Long-Term Behavior of Concrete. *Key Engineering Materials*, 711, pp.645–651.
- Samouh, H., Rozière, E. and Loukili, A. (2018). Shape effect on drying behavior of cement-based materials: Mechanisms and numerical analysis. *Cement and Concrete Research*, 110(2018), pp.42–51.

- Sharp, S. and Moruza, A. (2009). *VTRC 09-R9: Field Comparison of the Installation and Cost of Placement of Epoxy-Coated and MFMX 2 Steel Deck Reinforcement: Establishing a Baseline for Future Deck Monitoring*. Charlottesville: Virginia Transportation Research Council.
- Silfwerbrand, J. (1997). Stresses and Strains in Composite Concrete Beams Subjected to Differential Shrinkage. *ACI Structural Journal*, 94-S31.
- Skorpen, S.A. (2020). *Temperature effects and the behaviour of long reinforced concrete integral bridges*. Thesis: University of Pretoria.
- Skorpen, S.A., Kearsley, E.P., Clayton, C.R.I. and Kruger, E.J. (2021). Structural monitoring of an integral bridge in South Africa. *Proceedings of the Institution of Civil Engineers - Smart Infrastructure and Construction*, 173(3), pp.63–73.
- Song, Z., Xiao, J. and Shen, L. (2012). On Temperature Gradients in High-Performance Concrete Box Girder under Solar Radiation. *Advances in Structural Engineering*, 15(3), pp.399–415.
- South African National Standard (2006a). *SANS 6253:2006 Concrete tests- Tensile splitting strength of concrete*. Pretoria: The South African Bureau of Standards.
- South African National Standard (2006b). *SANS 5861-3:2006 Concrete tests- Part 3: Making and curing of test specimen*. Pretoria: The South African Bureau of Standards.
- South African National Standard (2006c). *SANS 5863:2006 Concrete tests- Compressive strength of hardened concrete*. Pretoria: The South African Bureau of Standards.
- South African National Standard (2000). *SANS 10100-1:2000 The structural use of concrete: Part 1: Design*. Pretoria: The South African Bureau of Standards.
- Soutsos, M. and Domone, P. (2017). *Construction Materials*. 5th ed. Boca Raton, FL: CRC Press.
- Tayşi, N. and Abid, S. (2015). Temperature Distributions and Variations in Concrete Box-Girder Bridges: Experimental and Finite Element Parametric Studies. *Advances in Structural Engineering*, 18(4), pp.469–486.
- Thurston, S.J. (1978). *Thermal Stresses in Concrete Structures*. Ph.D. Thesis: University of Canterbury, Christchurch.

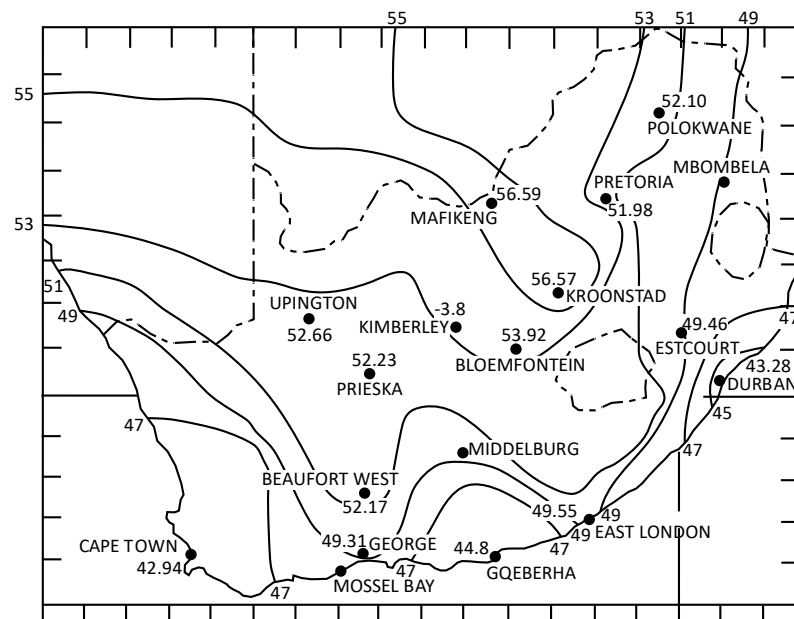
- Tia, M., Lawrence, A., Do, T.A., Verdugo, D., Han, S., Almershoud, M. and Markandeya, A. (2016). *Maximum Heat of Mass Concrete - Phase 2*. Gainesville, Florida: Engineering School of Sustainable Infrastructure and Environment, University of Florida.
- Vecchio, Frank.J. (1987). Nonlinear Analysis of Reinforced Concrete Frames Subjected to Thermal and Mechanical Loads. *ACI Structural Journal*, November-December(84-S51).
- Wang, B., Wang, W. and Zeng, X. (2010). Measurement and Analysis of Temperature Effects on Box Girders of Continuous Rigid Frame Bridges. *Journal of Civil and Environmental Engineering*, 4(10), pp.331–337.
- Wendner, R., Hubler, M.H. and Bažant, Z.P. (2013). The B4 Model for Multi-decade Creep and Shrinkage Prediction. In: *Creep, Shrinkage and Durability of Concrete Structures: CONCREEP-9*.
- William, G.W., Shoukry, S.N. and Riad, M.Y. (2008). Development of early age shrinkage stresses in reinforced concrete bridge decks. *Mechanics of Time-Dependent Materials*, 12(4), pp.343–356.
- Zhang, Y. and Hubler, M. (2020). Role of Early Drying Cracks in the Shrinkage Size Effect of Cement Paste. *Journal of Engineering Mechanics*, 146(11). 04020128 1-17.



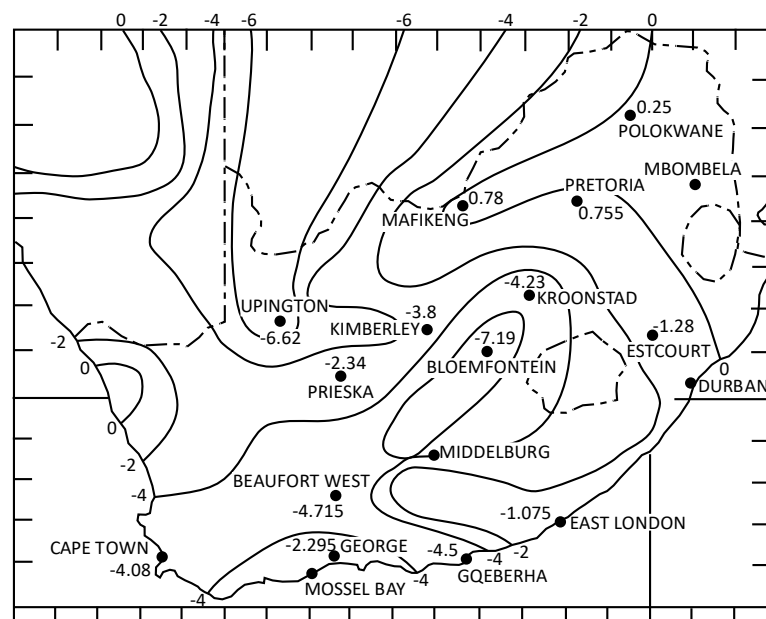
## APPENDIX A

This appendix details the vertical temperature distributions and shrinkage predictions calculated according to TMH7:1981 Parts 1&2 and TMH7:1989 Part 3 respectively, for the concrete T-beams used in this study for comparison to the experimental results.

The maximum and minimum shade air temperatures for Pretoria were read from **Figure A- 1** and **Figure A- 2** as 51.98 °C and 0.755 °C respectively.



**Figure A- 1 Isotherms of minimum shade air temperature in °C**



**Figure A- 2 Isotherms of maximum shade air temperature in °C**

These values were adjusted for the 1339 m elevation above sea level of Pretoria by subtracting 0.5 °C per 100 m height for minimum shade temperature and 1 °C per 100 m height for maximum temperatures. The adjusted maximum and minimum shade temperatures were calculated as 39 °C and -6 °C respectively. The maximum and minimum effective bridge temperatures were then determined according to the shade air shade temperatures and **Table A- 1** and **Table A- 2**. The values of  $T_1$  to  $T_4$  and  $T_1$  to  $T_3$  for the reverse and positive temperature differences were determined according to **Table A- 3**. And the values of  $h_1$  to  $h_4$  and  $h_1$  to  $h_3$  for the reverse and positive temperature distributions were calculated according to **Figure A- 3**.

**Table A- 1 Maximum effective bridge temperature**

| Maximum shade air temperature [°C] | Maximum effective bridge temperature [°C] | Maximum shade air temperature [°C] | Maximum effective bridge temperature [°C] |
|------------------------------------|---|------------------------------------|---|
| 30                                 | 32  | 46                                 | 41  |
| 31                                 | 32  | 47                                 | 42  |
| 32                                 | 33  | 48                                 | 42  |
| 33                                 | 33  | 49                                 | 43  |
| 34                                 | 34  | 50                                 | 44  |
| 35                                 | 35  | 51                                 | 44  |
| 36                                 | 36  | 52                                 | 45  |
| 37                                 | 37  | 53                                 | 45  |
| 38                                 | 38  | 54                                 | 46  |
| 39                                 | 38  | 55                                 | 46  |
| 40                                 | 38  | 56                                 | 47  |
| 41                                 | 39  | 57                                 | 47  |
| 42                                 | 39  | 58                                 | 47  |
| 43                                 | 40  | 59                                 | 48  |
| 44                                 | 40  | 60                                 | 48  |
| 45                                 | 41  |                                    |   |

**Table A- 2 Minimum effective bridge temperature**

| Minimum shade air temperature [°C] | Minimum effective bridge temperature [°C] | Minimum shade air temperature [°C] | Minimum effective bridge temperature [°C] |
|------------------------------------|---|------------------------------------|---|
| -15                                | -9  | -7                                 | -3  |
| -14                                | -9  | -6                                 | -3  |
| -13                                | -8  | -5                                 | -2  |
| -12                                | -7  | -4                                 | -1  |
| -11                                | -6  | -3                                 | 0   |
| -10                                | -6  | -2                                 | 0   |
| -9                                 | -5  | -1                                 | 1   |
| -8                                 | -4  | 0                                  | 1   |

**Table A- 3 Values of T for concrete superstructures**

| Depth of slab (h) [m] | Surfacing thickness [mm] | Positive temperature difference |                     |                     | Reverse temperature difference |                     |                     |                     |
|-----------------------|--------------------------|---------------------------------|---------------------|---------------------|--------------------------------|---------------------|---------------------|---------------------|
|                       |                          | T <sub>1</sub> [°C]             | T <sub>2</sub> [°C] | T <sub>3</sub> [°C] | T <sub>1</sub> [°C]            | T <sub>2</sub> [°C] | T <sub>3</sub> [°C] | T <sub>4</sub> [°C] |
| ≤0.2                  | unsurfaced               | 12.0                            | 5.0                 | 0.1                 | 4.7                            | 1.7                 | 0.0                 | 0.7                 |
|                       | waterproofed             | 19.5                            | 8.5                 | 0.0                 | 4.7                            | 1.7                 | 0.0                 | 0.7                 |
|                       | 50                       | 13.2                            | 4.9                 | 0.3                 | 3.1                            | 1.0                 | 0.2                 | 1.2                 |
|                       | 100                      | 8.5                             | 3.5                 | 0.5                 | 2.0                            | 0.5                 | 0.5                 | 1.5                 |
|                       | 150                      | 5.6                             | 2.5                 | -0.2                | 1.1                            | 0.3                 | 0.7                 | 1.7                 |
|                       | 200                      | 3.7                             | 2.0                 | -0.5                | 0.5                            | 0.2                 | 1.0                 | 1.8                 |
| 0.4                   | unsurfaced               | 15.2                            | 4.4                 | 1.2                 | 9.0                            | 3.5                 | 0.4                 | 2.9                 |
|                       | waterproofed             | 23.6                            | 6.5                 | 1.0                 | 9.0                            | 3.5                 | 0.4                 | 2.9                 |
|                       | 50                       | 17.2                            | 4.6                 | 1.4                 | 6.4                            | 2.3                 | 0.6                 | 3.2                 |
|                       | 100                      | 12.0                            | 3.0                 | 1.5                 | 4.5                            | 1.4                 | 1.0                 | 3.5                 |
|                       | 150                      | 8.5                             | 2.0                 | 1.2                 | 3.2                            | 0.9                 | 1.4                 | 3.8                 |
|                       | 200                      | 6.2                             | 1.3                 | 1.0                 | 2.2                            | 0.5                 | 1.9                 | 4.0                 |
| 0.6                   | unsurfaced               | 15.2                            | 4.0                 | 1.4                 | 11.8                           | 4.0                 | 0.9                 | 4.6                 |
|                       | waterproofed             | 23.6                            | 6.0                 | 1.4                 | 11.8                           | 4.0                 | 0.9                 | 4.6                 |
|                       | 50                       | 17.6                            | 4.0                 | 1.8                 | 8.7                            | 2.7                 | 1.2                 | 4.9                 |
|                       | 100                      | 13.0                            | 3.0                 | 2.0                 | 6.5                            | 1.8                 | 1.5                 | 5.0                 |
|                       | 150                      | 9.7                             | 2.2                 | 1.7                 | 4.9                            | 1.1                 | 1.7                 | 5.1                 |
|                       | 200                      | 7.2                             | 1.5                 | 1.5                 | 3.6                            | 0.6                 | 1.9                 | 5.1                 |
| 0.8                   | unsurfaced               | 15.4                            | 4.0                 | 2.0                 | 12.8                           | 3.3                 | 0.9                 | 5.6                 |
|                       | waterproofed             | 23.6                            | 5.0                 | 1.4                 | 12.8                           | 3.3                 | 0.9                 | 5.6                 |
|                       | 50                       | 17.8                            | 4.0                 | 2.1                 | 9.8                            | 2.4                 | 1.2                 | 5.8                 |
|                       | 100                      | 13.5                            | 3.0                 | 2.5                 | 7.6                            | 1.7                 | 1.5                 | 6.0                 |
|                       | 150                      | 10.0                            | 2.5                 | 2.0                 | 5.8                            | 1.3                 | 1.7                 | 6.2                 |
|                       | 200                      | 7.5                             | 2.1                 | 1.5                 | 4.5                            | 1.0                 | 1.9                 | 6.0                 |
| 1.0                   | unsurfaced               | 15.4                            | 4.0                 | 2.0                 | 13.4                           | 3.0                 | 0.9                 | 6.4                 |
|                       | waterproofed             | 23.6                            | 5.0                 | 1.4                 | 13.4                           | 3.0                 | 0.9                 | 6.4                 |
|                       | 50                       | 17.8                            | 4.0                 | 2.1                 | 10.3                           | 2.1                 | 1.2                 | 6.3                 |
|                       | 100                      | 13.5                            | 3.0                 | 2.5                 | 8.0                            | 1.5                 | 1.5                 | 6.3                 |
|                       | 150                      | 10.0                            | 2.5                 | 2.0                 | 6.2                            | 1.1                 | 1.7                 | 6.2                 |
|                       | 200                      | 7.5                             | 2.1                 | 1.5                 | 4.8                            | 0.9                 | 1.9                 | 5.8                 |
| ≥1.5                  | unsurfaced               | 15.4                            | 4.5                 | 2.0                 | 13.7                           | 1.0                 | 0.6                 | 6.7                 |
|                       | waterproofed             | 23.6                            | 5.0                 | 1.4                 | 13.7                           | 1.0                 | 0.6                 | 6.7                 |
|                       | 50                       | 17.8                            | 4.0                 | 2.1                 | 10.6                           | 0.7                 | 0.8                 | 6.6                 |
|                       | 100                      | 13.5                            | 3.0                 | 2.5                 | 8.4                            | 0.5                 | 1.0                 | 6.5                 |
|                       | 150                      | 10.0                            | 2.5                 | 2.0                 | 6.5                            | 0.4                 | 1.1                 | 6.2                 |
|                       | 200                      | 7.5                             | 2.1                 | 1.5                 | 5.0                            | 0.3                 | 1.2                 | 5.6                 |

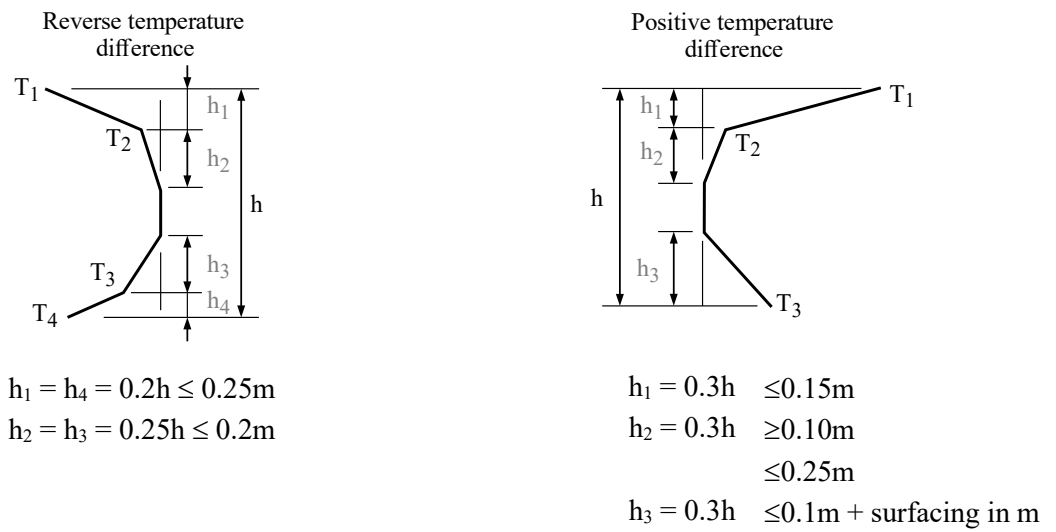


Figure A- 3 Positive and reverse temperature differences

The resulting positive and reverse temperature guidelines for the sections analysed for this study is shown in Figure A- 4.

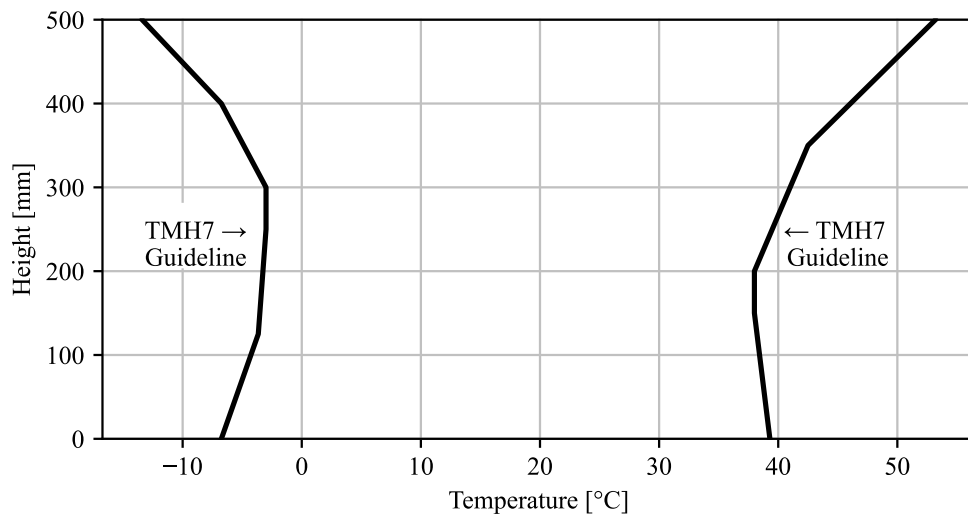


Figure A- 4 Positive and reverse temperature distributions

The graphs used to determine the partial coefficients in the calculation of the shrinkage deformation according to TMH7:1989 for the two sections analysed in this study were detailed in chapter 2.

$$\Delta_{cs} = k_L \cdot k_c \cdot k_e \cdot k_j \quad \text{Equation 2-1}$$

where:

$\Delta_{cs}$  = shrinkage deformation

$k_L$  = depends on the environmental conditions

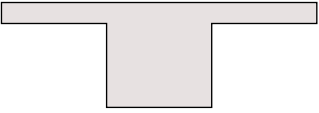
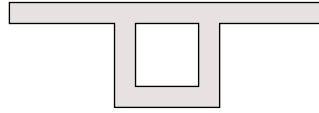
$k_c$  = depends on the composition of the concrete

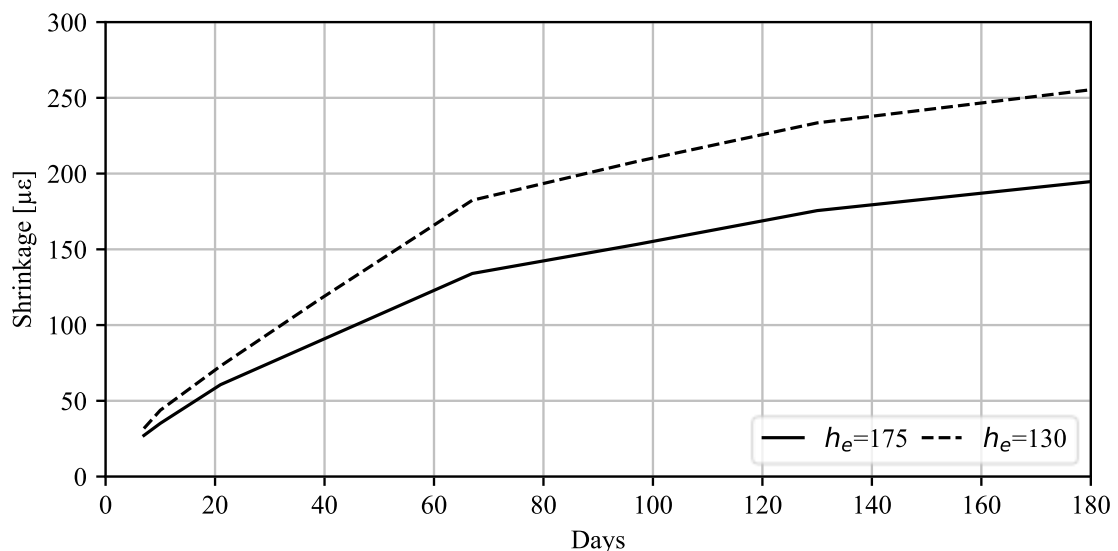
$k_e$  = depends on the effective thickness of the member

$k_j$  = defines the development of shrinkage as a function of time

Based on the environmental conditions, concrete composition and effective thickness of the sections the time constant partial coefficients calculated are listed in **Table A- 4**. The predicted shrinkage deformation is shown in **Figure A- 5**.

**Table A- 4 Partial coefficients for shrinkage deformation**

| Partial coefficient | <br>$h_e = 175\text{mm}$ | <br>$h_e = 130$ |
|---------------------|--|--|
| $k_L$               |  | 380  |
| $k_c$               |  | 1.0  |
| $k_e$               | 0.84   | 0.96   |



**Figure A- 5 Predicted shrinkage values**